Hydrothermal alteration of medium-grade metamorphic rocks of Metsämonttu VMS deposit, southern Finland

A comparative portable XRD and near-infrared spectroscopy analysis

Jenniina Siira

Geology (Bedrock Geology)
M.Sc. Thesis
Extent: 30 ECTS

Supervisors:
Esa Heilimo
Irmeli Huovinen

28.12.2021
Turku

Pro gradu -tutkielma

Pääaine: Geologia

Tekijä: Jenniina Siira

Otsikko: Hydrothermal alteration of medium-grade metamorphic rocks of Metsämonttu deposit, southern Finland: A comparative portable XRD and near-infrared spectroscopy analysis

Ohjaajat: Esa Heilimo, Irmeli Huovinen

Sivumäärä: 116 sivua + liitteet 5 sivua

Päivämäärä: 28.12.2021

Hydrotermiset muuttumisprosessit ovat yhteydessä monien taloudellisesti merkittävien malmivarantojen syntyyn. Tässä työssä esitetään vertaileva kannettavalla röntgendiffraktioanalysaattorilla (pXRD) ja lähi-infrapunaspektroskopialla (NIR) tehty analyysi neljästä kairasydämestä, jotka on kairattu Metsämontun vulkanogeenisesta massivisesta sulfidiesiintymästä (VMS). Kairasydämet edustavat matalan metamorfoosiasteen alemman amfiboliittifasieksen litologioita.

NIR-spektroskopia keskittyi lyhytaaltoisen infrapuna-alueen (short-wave infrared, SWIR; 1.0-2.5 µm) mittauksiin, joita täydennettiin näkyvän valon lyhytaaltoisen infrapuna-alueen (visible, near-infrared, VNIR; 0.4-1.0 µm) mittausaineistolla. SWIR- ja VNIR-aineisto kerättiin ASD Terraspec 4 Portable NIR -spektrometrillä pistemittauksina ja tulkittiin The Spectral Geologist -ohjelmistolla. pXRD-aineisto kerättiin käyttäen Olympus Portable Onsite XRD Terra-542 -laitteistoa ja tulkittiin XPowder-ohjelmistolla.

pXRD:llä ja SWIR-spektroskopialla havaittuja mineraalikokoonpanoja vertailtiin petrofysikaaliseen ja kannettavalla röntgenfluoresenssilaitteistolla (pXRF) mitattuun geokemialliseen aineistoon. SWIR-aineisto yhdistettiin litologiseen aineistoon käyttämällä Al-, Fe- ja Mg-hydroksidien absorptiokäyrien sijaintien vaihtelua ja havainnoimalla mineralogista muuttumista niiden kautta.

pXRD-mittauksien laatuongelmia, kuten diffraktogrammien taustojen nousua, ilmeni sulfideja, etenkin lyijyhohdetta, sisältävissä näytteissä. Toinen laatuseikka liittyi näytteisiin, jotka sisälsivät preferoitua orientaatiota suosivia mineraaleja, kuten muskoviittia. Paljon amorfista tai nanokiteistä, erittäin hienojakoista materiaalia sisältävät näytteet ovat epävarmuustekijöitä, jotka aiheuttivat laatuongelmia diffraktogrammeihin. Edellämainituista sekä useista muista virhelähteistä, kuten lyhyestä mittausajasta ja alhaisesta resoluutiosta johtuen metodia ei voida todeta luotettavaksi pieninä pitoisuuksina (<5 wt%) esiintyvien mineraalien ja aksessoristen mineraalien tunnistamisessa.

SWIR- ja VNIR-spektroskopialla tehdyillä pistemittauksilla havaittiin olevan omat rajoitteensa siinä, kuinka paljon eri mineraalifaaseja niillä voidaan tunnistaa. Pistemittausten edustavuus on myös rajallinen. pXRD ja SWIR-spektroskopia kuvaavat mineraalien vaihtelua eri tavoin. pXRD-aineistoa käytetään yleisimpien päämineraalien tunnistuksessa, kun taas SWIR-aineistoa käytetään vaaleiden kiilteiden ja kloriitti-ryhmän mineraalien kemiallisen vaihtelun havaitsemiseen.

Yhdistämällä pXRD- ja SWIR-aineistoista saatua tietoa petrofysikaaliseen ja pXRF-aineistoon on voitu tunnistaa eri muuntumistyyppejä Metsämontun esiintymän muuntuneissa kivissä, ja jo olemassa olevia tietoja litologisista yksiköistä on voitu tarkentaa.. Tämä lähestymistapa on suositeltava ja sillä voidaan kompensoida eri menetelmien puutteita.

Avainsanat: Metsämonttu, lähi-infrapunaspektroskopia (NIR), kannettava XRD (pXRD), vulkanogeeniset massiiviset sulfidiesiintymät (VMS), hydroterminen muuttuminen

Master's thesis

Subject: Geology

Author: Jenniina Siira

Title: Hydrothermal alteration of medium-grade metamorphic rocks of Metsämonttu deposit, southern Finland: A comparative portable XRD and near-infrared spectroscopy analysis

Supervisors: Esa Heilimo, Irmeli Huovinen

Number of pages: 116 pages + appendices 5 pages

Date: 28.12.2021

Hydrothermal alteration processes are connected to the formation of many economically important ore deposits. This study represents a comparative portable XRD (pXRD) and near-infrared (NIR) spectroscopy analysis of four drill cores of Metsämonttu volcanogenic massive sulphide (VMS) deposit, southwestern Finland. The drill cores represent hydrothermally altered low-grade metamorphic lithologies of lower amphibolite facies.

The NIR spectroscopy focuses on short-wave infrared (SWIR; 1.0-2.5 µm) analysis with some supplementing visible, near-infrared (VNIR; 0.4-1.0 µm) data. The SWIR and VNIR data were gathered with ASD Terraspec 4 Portable NIR Spectrometer as point measurements and were interpreted with The Spectral Geologist software. The pXRD data were measured using Olympus Portable Onsite XRD Terra-542 device and were interpreted with XPowder software.

In this study, the mineral assemblages identified with the pXRD, and the SWIR spectroscopy are compared to the petrophysical and geochemical data measured with portable X-ray fluorescence (pXRF). The SWIR data are connected to the lithological data by using the wavelength positions of AlOH, FeOH, and MgOH absorption features and identifying the mineralogical alterations pointed by them.

The pXRD measurements used in this study show to have quality issues like rising of the diffractogram background with the samples including sulphidic minerals, especially galena. Another quality issue is observed with the samples including minerals with preferred orientations, particularly muscovite. High amount of amorphous, or nanocrystalline material of extremely fine grain size in the sample is one uncertainty factor that is shown to produce quality problems to the diffractograms. Due to previously mentioned and several other quality issues such as short measurement time and low resolution, the method is shown not to be reliable enough to be used in identification of minor mineral phases (<5 wt%) or accessory minerals.

Furthermore, it is shown that the point measurements done with the spectrometer, using the SWIR and VNIR wavelengths, have their limitations regarding the number of minerals that could have been identified. In addition, the representativeness of the point measurements is shown to be limited. However, both the pXRD and the SWIR spectroscopy describe the mineral variation in a different manner. The pXRD data are used to identify most of the major mineral phases in the sample, while the SWIR data are used to observe chemical alterations of white mica and chlorite group phases.

The study identifies the alterations of the altered rocks of the Metsämonttu deposit by combining the pXRD and the SWIR data with the pXRF and the petrophysical data, and specifies the information related to the previously logged lithological units. This approach is a suggested way to overcome the limitations of each method.

Keywords: Metsämonttu, near-infrared (NIR) spectroscopy, portable X-ray diffraction (pXRD), volcanogenic massive sulphide (VMS) deposits, hydrothermal alteration

Contents

1 Introduction

Old mining sites, also known as brownfields targets, are promising areas in terms of mineral exploration. It is known that they have an existing ore potential and there are already research data available from these areas. However, they might be poorly explored when contrasted to the possibilities offered by new measurement and data processing technologies (Ross et al. 2013). Examples of these new technologies would be near-infrared (NIR) spectroscopy, portable X-ray diffraction (pXRD) and automated mineral identification.

Metsämonttu (Fig. 1) is an old zinc mine located in Kisko, Southern Finland. In terms of geology, it is a volcanogenic massive sulphide deposit, and it belongs to Aijala part of the volcanic 1.90-1.89 Ga Orijärvi formation (Nironen & Luukas 2017) formed during the Svecofennian orogeny (Nironen et al. 2016). The deposit was found in 1946 by Suomen Malmi Oy (SMOY). The mine operated in 1951-1974 and was owned by Outokumpu Oy. The main commodities were zinc, copper, lead and some gold and silver. (Latvalahti 1979)

Figure 1. The old mine of Metsämonttu. Photo: Outokumpu Oy.

Two potential contemporary field analysis methods for characterization of alteration in VMS deposits would be the pXRD and the NIR spectroscopy. Both methods were tested for systematic alteration mineralogical mapping as a part of the Geological Survey of Finland (GTK) process development project in a VMS-type Aijala-Metsämonttu deposit.

The X-ray diffraction (XRD) is a conventional method for the mineral identification. It is a traditional and precise laboratory-based method that provides information of crystal structures, phase composition, and atomic spacing of solid, crystalline materials. pXRD devices are the latest applications of the XRD method but their suitability to mineralogical research has been relatively little tested.

The NIR spectroscopy is another relatively new mineral identification method. It uses short-wave infrared (SWIR; 1.0-2.5 μm) reflectance spectroscopy data that are used for both mineral identification and for classification of the chemical changes in minerals. The SWIR data are fulfilled with the visible and near-infrared (VNIR; 0.4-1.0 μm) spectroscopy data providing information mainly on iron oxide minerals on a group level as well as on rare earth elements (REE).

This thesis aims to ascertain if the pXRD and the NIR spectroscopy data would be suitable data collection methods for mineral exploration of volcanogenic massive sulphide (VMS) deposits. Furthermore, it is also studied whether the data collected with these methods tell about the alteration of minerals.

Four drill cores from Metsämonttu have been initially analyzed with field-based portable ASD TerraSpec 4 spectrometer and TERRA-542 pXRD analyzer. The drill cores have been also measured with portable XRF (pXRF) and petrophysical methods including density, magnetic susceptibility, and conductivity measurements. This study focuses on the interpretation of the pXRD data using XPowder software and the SWIR and VNIR data using The Spectral Geologist (TSG) software. Each software allows automatic mineral interpretation to some extent. The petrophysical and the pXRF measurement data are used as a support material in the characterization and interpretation of the drill cores.

2 Literature review of the portable X-ray diffraction and the imaging spectroscopy

2.1 X-Ray Diffraction

2.1.1 Principles of X-ray diffraction

The XRD is a method that provides information on crystal structures of crystalline materials and therefore, it is of great use in identification of mineral phases. It has been used since 1930s for the quantification of phase abundances (Clark & Reynolds 1936) as well as studying the sizes and textures of crystallites, their internal stress or micro-strain (Will 2006). According to Max von Laue (1912), crystals have a three-dimensional structure, a lattice, that scatters radiation in a wavelength in the proximity of interatomic distances.

A crystal is defined as a solid material where its atomic arrangement is repeated in a three-dimensional space as follows:

$$\mathbf{r} = n_1\mathbf{a} + n_2\mathbf{b} + n_3\mathbf{c}. \tag{1}$$

In Equation 1 three basis vectors **a**, **b** and **c** depict the crystal arrangement or a motif in space, forming the lattice (**r**). The fundamental repetitive unit of the lattice is termed a unit cell. It consists of three lattice constants a, b and c which are the lengths of the basis vectors, and three angles α, β and γ that locate between the basis vectors (Massa & Gould 2004). When the material is in its crystalline state, its molecules are in an organized disposition (Giacovazzo 1992).

X-rays are electromagnetic waves occurring within the wavelength range of 0.01-10 nm of the electromagnetic spectrum. The electromagnetic spectrum (Fig. 2) is divided into frequency bands according to the nature of radiation. The boundaries between the bands are not tightly defined, and therefore might vary (Rumble 2021). X-ray diffraction describes the procedure where this radiation, not changing its wavelength, is converted via interference of the lattice into many reflections having distinguishable orientations in space. The method measuring the directions and the intensities of the reflections is known as X-ray structure analysis. These internal atomic distances cannot be observed within visible light wavelength region, approximately 300-700 nm since they are located within 100-300 pm wavelength region in the electromagnetic spectrum (Massa & Gould 2004).

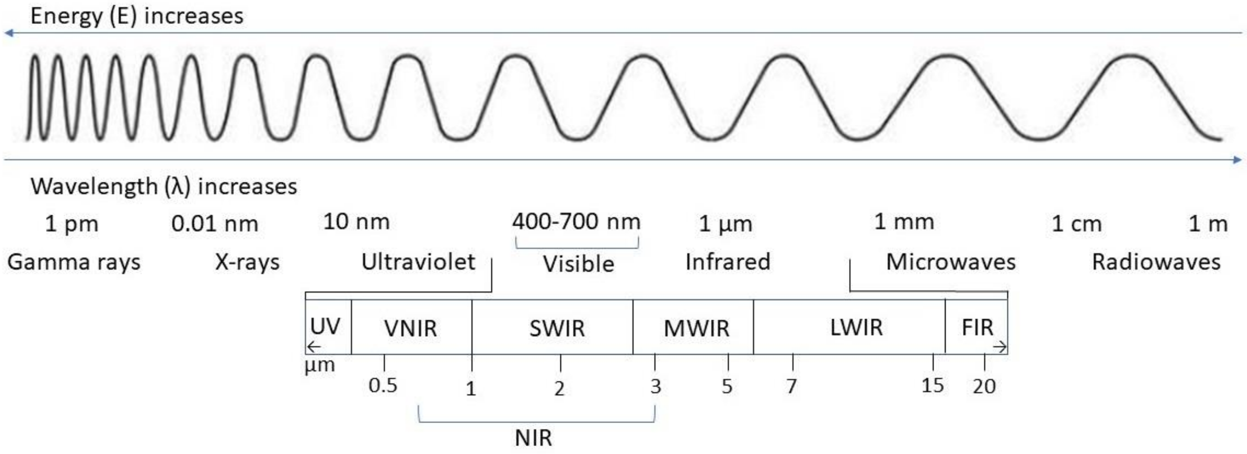

Figure 2. The electromagnetic spectrum. UV = ultraviolet, VNIR = visible, near infrared, NIR = near infrared, SWIR = short-wave infrared, MWIR = mid-wave infrared, LWIR = long-wave infrared, FIR = far infrared. Figure adapted and modified from Booysen et al. 2021a.

In Equation 2 the wavelengths (λ) of X-rays are reversibly comparable to their energy (*E*):

$$E = hv = h\frac{c}{\lambda}, \tag{2}$$

where h = the Planck's constant, v = the frequency and c = the velocity of light. In X-ray diffraction a conventional unit to be used is Å (Ångström), a unit length of 10^{-10} m or 0.1 nm.

When X-rays pass through a material with a certain wavelength (λ) and an intensity (I_0), they undergo several different processes: first they will become debilitated, then absorbed and scattered. In Equation 3 the event intensity (I_0), the attenuation coefficient (μ, known also as absorption coefficient) and the length of the travel through a substance (d) all effect on the transmitted intensity (I):

$$\mathrm{I} = \mathrm{I}_0 \mathrm{e}^{-\mu \mathrm{d}}. \tag{3}$$

Mass attenuation coefficient (MAC) is defined as following (Equation 4):

$$\frac{\mu}{\rho_m}, \tag{4}$$

where μ = the attenuation coefficient and ρ = density (ICRU 1980).

X-rays can be produced in example with a sealed high-vacuum tube (Fig. 3). Electrons are transmitted by a heated filament that is used as a cathode, and they are targeted to hit an anode, a flat metallic plate. Afterwards, the X-rays are generated on the surface of the anode in two different ways. When electrons reach the field of the metallic ions, they decelerate and this transforms part of their energy into radiation. 99 % of the kinetic energy turns into heat and 1 % to X-ray radiation, and therefore anode needs sufficient cooling provided conventionally by water circulation. (Massa & Gould 2004; Ermrich & Opper 2011)

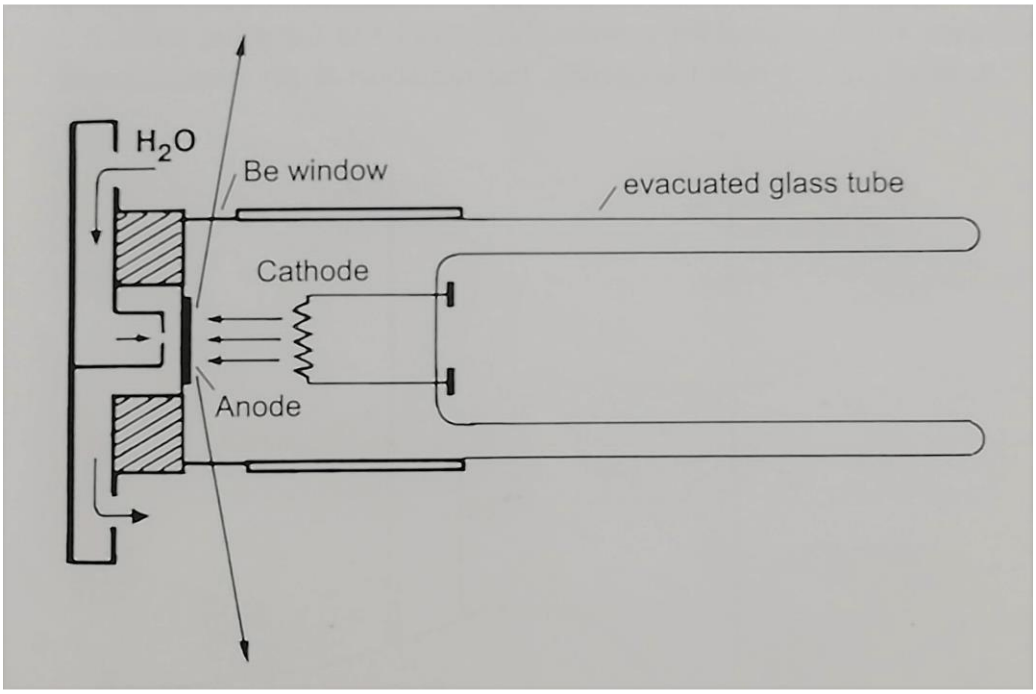

Figure 3. An illustration of one type of an X-ray tube (Massa & Gould 2004).

This process creates so called white radiation, which is a continuous energy spectrum. White radiation depicts the narrowest wavelength generated which is a function of used voltage, described in Equation 5:

$$\lambda_{\mathrm{min}} = \frac{\mathrm{hc}}{\mathrm{eU}}\,, \tag{5}$$

where h = Planck's constant, c = the velocity of the light, e = the electronic charge and U = the applied voltage. If the units of U would be kilovolts (kV), then

$$\lambda_0\,(\text{Å}) = \frac{12.4}{\mathrm{U\ (kV)}}\,. \tag{6}$$

(Massa & Gould 2004; Ermrich & Opper 2011)

According to the Dauvillier law, the maximum of the radiation wavelength (λ_{max}) is between 1.5-1.7 times λ_0. The total intensity of the white radiation wavelength (I_{wr}) depends on the emission current, the acceleration voltage as well as the atomic number, and therefore the atomic radius of the target, as can be seen in Equation 7:

$$\mathrm{I_{wr}} \sim \mathrm{ZU^2 i}, \tag{7}$$

where Z = atomic number, U = tube voltage and I = emission current of the X-ray tube.

However, when studying crystal structures, observing the characteristic radiation is in the focus. Considering the structure of an atom according to the Bohr atom model, each atom has a nucleus that hosts protons with a positive charge and neutrons without any charge. Around the nucleus there are negatively charged electrons organized in shells. The order of the shells from inwards towards outer shells is K (principal quantum number n = 1), L (n = 2) and M (n = 3), and the shells are further divided into subshells. Each shell can host a certain number of electrons.

Characteristic radiation emerges when an electron is driven away of the material of interest by emitting it with high enough energy to exceed the binding energy of the electron to release it. When the electron is released, the incoming X-ray radiation gets absorbed and scattered. Too intensive energy causes that plenty of photons would only pass through the atom hardly interacting with it. Characteristic radiation is adjusted with acceleration voltage. If the voltage would be too high, it would be seen as high background noise in the diffractogram since the white radiation would cover the characteristic radiation.

Scattering is process that includes reflection and refraction. Its extent in relation to absorption dictates how large a number of photons is received from a plane (Clark 1999). Thompson or Rayleigh scattering, that is also known as coherent, preserving scattering, occurs when the arriving photon scatters elastically when it hits the electrons within the inner shells. This type of scattering preserves the photon energy constant and does not change the wavelength of the photon. It is well suitable for elements of medium weight since heavy elements scatter more strongly. It is the most essential type of scattering in X-ray diffraction.

Another essential scattering mechanism is incoherent, prevailing scattering, which occurs as Compton scattering and fluorescence. In Compton scattering, the photon encounters a loosely bound electron and pushes the electron off its shell. The photon loses its energy in this process: with light elements this effect is stronger since light components have more loosely bound electrons. The laboratory based XRD instrument can neglect this effect.

In fluorescence, an empty space is created in the shell when the electron is expelled. The atom is now aroused with energy willing to restore the equilibrium. It moves an electron from a higher-level vacancy to a lower-level vacancy, in example from the outer L-shell to the inner K-shell. This leads to an emission of an X-ray photon with a known wavelength, which equals to the energy difference between these two shells. Since every atom bears its own specific energy state, the radiation it delivers is characteristic to it. The wavelengths delivered by the X-ray tube are therefore characteristic to its anode material. The Moseley law (Equation 8) describes the dependency of the wavelength of the photon and its proton number (Z):

$$\frac{1}{\lambda} \sim Z^2. \tag{8}$$

This mechanism is beneficial in XRF since it aids the determination on elemental proportions in a sample, but it is not a desired one in XRD since it elevates the background of a diffractogram and might weaken the peak/background proportion. (Ermrich & Opper 2011)

The frequency can be affected by the material of the anode. In mineralogical studies, Cu and Mo anodes are common, but also Ag and Co are used. All the anode materials have also their own best fit for production of X-rays, in example for Cu U_{opt} = 40 kV producing Kα energy of 8.0 keV, and for Co U_{opt} = 30 kV producing Kα energy of 6.9 keV (Ermrich & Opper 2011). Co is often a preferred anode material when there would be Fe-rich materials present in the sample since it can be used to avoid background increase which could appear when copper Kα radiation would be used as a radiation source while measuring Fe-rich samples (Ramos Dias de Andrade et al. 2016).

The characteristic spectrum contains multiple lines. Kα lines of $K\alpha_1$ and $K\alpha_2$ radiation appear as a doublet. Kβ line emerges when an electron originating from the M-shell migrates to the K-shell. Additional peaks caused by Kβ radiation are usually subdued with a fitting monochromator, usually a filter (Table 1) or a single-crystal monochromator. (Massa & Gould 2004; Ermrich & Opper 2011)

Table 1.
Wavelengths used for X-ray diffraction and suitable filters for each anode. Intensity relations: Kα1 : Kα2 : Kβ ≈ 100:50:25. (ICDD, International Centre of Diffraction Data, after Ermrich & Opper 2011.)

Anode	Wavelength (Å)			Kβ-filter
	$K\alpha_1$	$K\alpha_2$	Kβ	
Cu	1.54056	1.54439	1.39222	Ni
Co	1.78897	1.79285	1.62079	Fe
Mo	0.70930	0.71359	0.63229	Zr

Diffraction and interference of X-rays was initially described by Bragg (1913). In a crystalline material, they would appear “as reflections at the atomic planes of the crystal lattice”. Their locations can be calculated using the Bragg’s law (Equation 9, also graphically represented in Figure 4):

$$\Delta = 2\mathrm{d}\sin\theta = \mathrm{n}\lambda\,, \tag{9}$$

where Δ = the plane, d = the interplanar configuration d_{hkl} (hkl = Miller indices), θ = the Bragg angle θ_B, n = the reflection of the order n, λ = the wavelength (Ermrich & Opper 2011). Miller indices are a conventional vector representation of atomic planes in crystallography describing lattice planes and directions. In this notation h, k and l would be integers representing reciprocals of intercepts while a, b and c (alternatively x, y and z) would represent crystallographic axes. (Ashcroft & Mermin 2021)

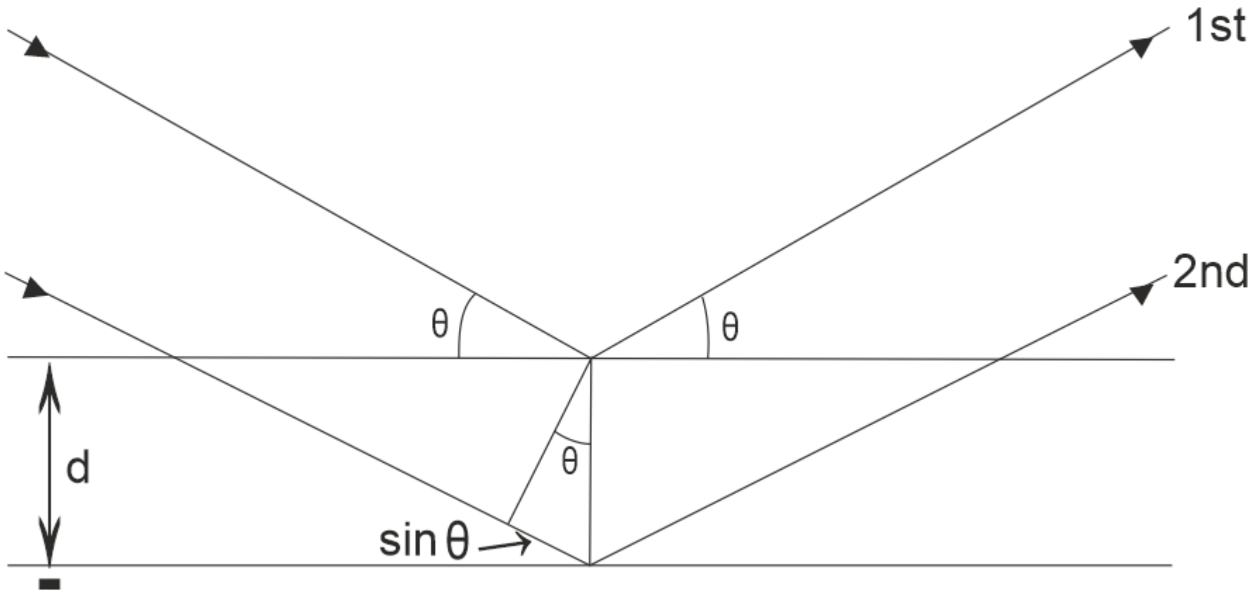

Figure 4. Reflection of the ray of light according to the Bragg’s law, where the line with the arrow describes the ray of light and its reflectance. d is the interplanar configuration d_{hkl} (hkl = Miller indices) and θ is the Bragg angle θ_B. Figure adapted from Ermrich & Opper 2011.

In principle each chemical substance has its own diffraction pattern that shows the intensity of the rays in relation to Bragg's 2Θ angle. Due to this, it is possible to identify the crystal structure of a substance by the positions and intensities of reflections. If the chemical composition of two substances would be like each other, they can be distinguished by their diffraction pattern.

The Bragg's law defines the positions of the reflections. According to the Bragg's law, the Miller indices (d_{hkl}) describe the interplanar spacing (d) within the lattice planes. The order n of interferences has greater (hkl). If n = 1, then the second order of the (111) reflection would be (222). Resolution describes the ability of the detector to distinguish at least two nearby reflections of each other. In single-crystal diffraction the lowest quantifiable d-value for the utilized wavelength would be the resolution of the measurement: if sinθ would be 1, then $d_{min} = \lambda/2$. In X-ray scattering occurring within a small angle the resolution would be the highest d-value that would be possible to detect. If the d-values of a substance are known, they can be used to define the lattice parameters a, b and c applying the quadratic forms in the calculation. The less symmetric the lattice is, the more complicated the equation is.

The intensity of the reflections is controlled by the sample amount, its absorption, and the structure factor. The structure factor is dependent from the configuration of the atoms and their electron amount within the unit cell, and the crystal symmetry. Materials of high order, such as body-centered cubic ones, tend to have systematic extinction and therefore, not all their reflections would be visible.

The shape of the reflections is regulated by instrumental effects and sample-related effects. Examples of instrumental effects include diffractometer configuration, the optical components of the device, and the detector setup. Crystal size and defects in the crystal lattice could be sample-related effects. (Ermrich & Opper 2011)

In the Debye-Scherrer method a powdered mineral sample is rotated in a glass needle placed in the middle of a metallic cylinder. During this rotating movement a primary beam is led through the sample, diffracts, and differs conically with the 2θ angle of the primary beam. The resulting diffraction pattern represents the value of the 2θ angle of a reflectance of each grain surface. (Debye & Scherrer 1916)

In XRD the sample can be studied in two different ways using the X-rays. The first one would be reflection geometry where the sample surface would be flat, and the X-rays would be scattered from the surface of the sample. In a conventional Bragg-Brentano setup shown in Figure 5 the focusing spot of the X-ray tube, the surface of the sample and the detector slit form a focusing circle. Moreover, the detector slit and the focusing spot of the tube form a measuring circle where the centre of the circle would be the surface of the sample. (Ermrich & Opper 2011)

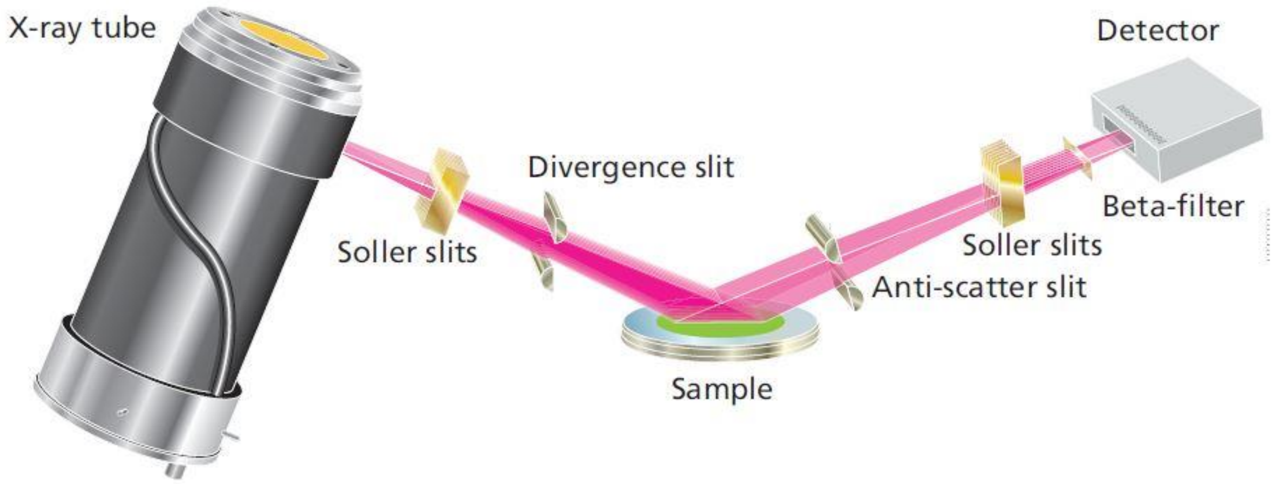

Figure 5. Conventional Bragg-Brentano reflection geometry setup used in reflection measurements (Ermrich & Opper 2011).

In this geometry, the diffracted angle is always double the incident angle. This is called the θ/2θ mode, and usually this means that the X-ray tube position would be fixed, and the sample and detector would move. This geometry is sensitive to the changes of sample height: if the sample would be lifted, the 2θ values of the angles would be moved to higher angles. The θ/θ mode is also used by some vertical diffractometers: in this setup the sample will remain in a horizontal position while the tube and the detector are moving. This would allow to measure liquid or melted samples or samples of a great size.

Transmission geometry is another method where the X-rays would go through a sample that is X-ray transparent. In this method the powdered sample would be placed in between foils or inside a glass capillary, or it would be measured as a thin solid. In this setup there is an extra component for focusing placed between the X-ray tube and the sample, such as a multi-layered mirror or a rounded monochromator. Focusing of the beam would be over the sample to the detector. The first optical components and the detector should be at equal distance according to the Debye-Scherrer method. Material absorption is in an important role in this type of geometry since it attenuates the intensity of the beam of light. The intensity ratio of the incoming beam and penetrated beam should not exceed 4. Thickness of the sample is dependent on its porosity and tends to vary. (Ermrich & Opper 2011)

Detector is one of the most important components of the diffractometer since it is the eyes of the device. According to Ermrich & Opper (2011), there are different types of detectors: point (0D), line (1D) and area (2D). The point detector counts all the incoming photons but is not sensitive to their position. The line detector counts the photons in 2θ orientation in relation to their position of the window of the detector. The area detector resembles the line detectors with the difference that the intensities would be observed perpendicular to 2θ axis.

Features of the detector influence which purposes it could be used. The angular resolution describes how the detector can recognize different d-spacings close to each other. The energy resolution describes if the detector can observe only Kα or Kα$_1$ radiation and its ability to attenuate unwanted Kβ radiation in example using a monochromator or a filter. The count rate linearity would be a limit at which the measured intensity would begin to deviate over 5 % of the initial value. Too big deviations can cause distortions to the diffractograms. The measurement time would be the time that is needed to measure a designated angular range. The noise level of the detector is expressed as counts per second (cps). The dynamic range would be the largest measurable intensity range which is the divergence between the maximal intensity and the noise level. The active length or the active area of the detector describes the angular range it is able to measure. (Ermrich & Opper 2011)

X-ray powder diffraction data are represented as powder diffractograms (Fig. 6), profile patterns, that describe the crystalline phase and the amorphous phase present in the sample. Here the diffraction angle (2θ) is depicted on the x-axis and the intensity on the y-axis. It consists of peaks (reflections), and the information obtained from the diffractograms come from peak locations, shapes, and intensities.

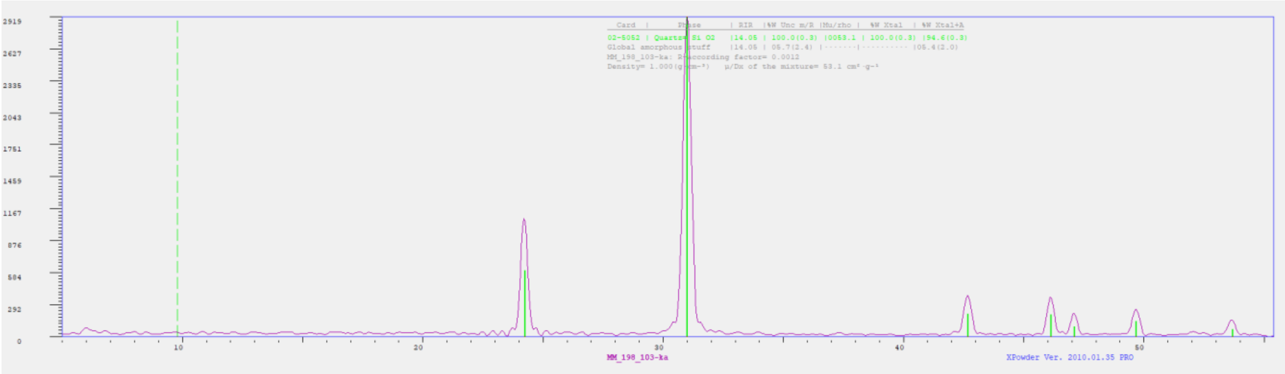

Figure 6. An example of a diffractogram of the drill core MM-198 in the depth of 103 metres from this study. The diffraction angles are in 2Θ scale.

The peak positions calculate on the recurrent order of the atoms and the used wavelength, and can be used for qualitative phase evaluation, defining lattice parameters, and observing residual stress. The peak intensity is connected to the crystal structure, used wavelength and sample preparation procedures, and it provides data for quantitative phase analysis, determining the crystal structure and their possible preferred orientations. The peak profiles relate to lattice distortions and can be used to obtain information on crystal sizes and micro-scale strain. (Ermrich & Opper 2011)

X-ray diffraction is not directly applicable on the characterization of amorphic materials (Billinge & Dinnebier 2008). When a substance is in amorphous state, its atoms are insufficiently ordered within its structure. This can be seen as wide bumps in the diffractograms (Ermrich & Opper 2011).

If the particles are ground down to as small as 3.5 µm grain size, the quantified amount of amorphous substance of approximately 20-25 wt% falls to minimal quantities (Snellings 2014). However, by using semiquantitative methods it is possible to try to identify the amount of amorphic substances in the sample.

There are many factors that should be taken into account in the sample preparation, measurement, and interpretation. An ideal polycrystalline sample would be a combination of randomly oriented crystals. If the sample would be entirely isotropic, a simple single measurement done by adding a film perpendicular to the X-ray beam would be enough for the characterization of the diffractogram. However, if the orientations of the sample particles are not completely random, the resulting pattern would not be isotropic. Due to this issue the sample is rotated to measure as many different orientations as possible to create more homogenous a diffractogram, although sometimes preferred orientations might be of interest. (Giacovazzo 1992)

According to Will (2006), powder in powder diffraction can be “a solid substance divided into very small particles”, but it can also be a solid piece, or alike a thin film or liquid. A sample could be in example a whole rock, and from the sample a smaller fraction is taken as a specimen for the XRD. In an ideal powdered specimen, the average grain size of the XRD would be 10-50 µm (Pecharsky & Zavalij 2009) and for Rietveld analysis 1-5 µm (Ermrich & Opper 2011; Snellings 2014). It should be representative enough (Will 2006), there would not be any internal stress and particles would have no preferred orientations. If the particles would be finer than 1 µm, the reflections become wider since then the particles would be of nanoscale size (Ermrich & Opper 2011). The grain size of a crystal can be calculated from the diffractogram using the Scherrer formula (Equation 10):

$$\mathrm{Dp} = \frac{0.94 \times \lambda}{\beta \times \cos\Theta}, \tag{10}$$

where Dp = average crystallite size, β = line widening in radians, Θ = Bragg angle, λ = X-ray wavelength.

Ermrich and Opper (2011) represent that excessive processing of the sample should be avoided. Grinding the sample might lead to different problems, such as heating of the sample which would cause phase transformations and oxidation. Plate-like crystallites are typically ground poorly, and their texture might then cause distortions to the diffractograms. Too long grinding might destroy the lattice structures of the crystals, and this might turn the sample amorphous. For the laboratory XRD the sample is either prepared in a suspension with acetone and spread on a glass slide or prepared into a side-loaded or back-packed preparate. Plate-like crystals might be a problem when prepared on a glass slide or into the back-packed preparate due to preferred orientation, while the side-loaded preparate aims to deal with this problem and create a random orientation on the sample surface.

Random orientation of the crystals in polycrystalline samples might also result to loss of some information due to overlapping diffraction peaks in the diffractogram. This effect can be tried to be solved with Rietveld refinement method, which uses profile intensities rather than integrated amounts. This elaborate quantitative method was initially developed for neutron powder techniques and was later extended to X-ray diffraction. It aims to deal with the problematics of overlapping peaks, peak separation, and preferred orientation of plate-like crystals like mica, chlorite-group minerals and amphiboles, by applying a set of corrections to refine the diffractogram profile (Rietveld 1969), aiming to refine the full pattern profile as well as the crystal structures (Will 2006), without the need to use time-demanding calibration procedures or standards in the measurement process (Hill & Howard 1987).

In general, studying the wide pattern reduces inaccuracies derived from the systematic errata. However, the Rietveld method is applicable only if all the phases in the sample have been identified (De La Torre et al. 2001), and the phases should preferably by crystalline (Billinge & Dinnebier 2008). According to Will (2006), the Two Stage method is another refinement method that should provide identical results to Rietveld method if it is applied correctly. First positions and intensities of all reflections are defined by decomposition by separating the overstepping diffraction maxima, and then the actual crystal structures are calculated. There are also other quantitative methods used in XRD such as reference-based intensity ratios (RIR; Smith et al. 1987), or the March function that tries to deal with the problem of preferred orientation (Dollase 1986). In RIR methods describe the ratio of the most intensive peak of a phase α to the most intensive peak of a standard s (Billinge & Dinnebier 2008).

Rietveld method can be also adapted to quantification of the amount of amorphous material in the sample by using a defined portion of an internal standard such as Al_2O_3 with corundum structure or SiO_2 with quartz structure (De La Torre et al. 2001). However, the amount of the internal standard effects strongly on the accuracy of the quantification of the amount of the amorphous matter (Westphal et al. 2009).

The diffractograms can be analyzed using different software that use reference databases with stored reflection patterns. Identification of minerals is based on comparing the obtained diffraction patterns to a mineralogical reference database (Billinge & Dinnebier 2008), such as PDF-4/Minerals by International Centre for Diffraction Data (ICDD) or American Mineralogist Crystal Structure Database (AMCSD). There are several software that can be used for basic evaluation and phase interpretation of XRD diffractograms, such as Diffrac.Eva by Bruker, PDXL2 by Rigaku and XPowder. The software differ of their features, in example Diffrac.Eva and PDXL2 have both an option to compare the quality of diffraction patterns for comparison. Quantitative analysis with or without Rietveld refinement, profile fitting, and pattern treatment can be done using software like HighScore Plus by Malvern Panalytical or Siroquant by Sietronics.

2.1.2 Portable X-ray diffraction

The pXRD is a relatively new application of X-ray powder diffraction. It is a portable device suitable to use in field conditions that requires minimal sample preparation procedures and requires relatively short measurement times. CHEMIN, the first commercial application of the pXRD using a charge-coupled device (CCD) camera funded by National Aeronautics and Space Administration (NASA), came to the market in the beginning of the 21st century and was used to conduct definitive mineralogical analysis of rocks and soils on Mars (Blake et al. 2012; Sarrazin et al. 2005).

According to Cornaby et al. (2001), a significant technological advance was the CCD camera where each pixel acts as a separate energy dispersive detector recording the dimensional location and the intensity of an incoming X-ray. This innovation also allowed the compact packing of the reflectometer. The device can measure both the pXRF and the pXRD data (Sarrazin et al. 2005). Earlier research has suggested the suitability of pXRD for identification of at least major mineral phases, and even of quantitative mineralogical data (Burkett et al. 2015), cultural historical research (Gianoncelli et al. 2008), and petroleum exploration (Burkett 2019).

In a laboratory based XRD device applying the reflection geometry, the sample is conventionally placed to the sample holder in a horizontal position. Depending on the setup and the measurement software, the spinner would usually rotate the sample while different parts of the device (such as the goniometer or the detector) would be moving during the measurement. It is also possible to measure the sample without rotating it. Then the crystals would not be measured in a random orientation, and only one angular direction would be measured. This method is typically applied to samples with only one prevalent mineral phase, such as graphite.

In any case the setup is different in the pXRD where the sample is placed into a sample holder that vibrates during the measurement. It uses transmission geometry since the sample holder of pXRD consists of two thin and transparent Mylar/Melinex (biaxially-oriented polyethylene terephthalate) or Kapton (polyimide) films held together by a metallic frame with a 5 mm circular window, and during the measurement the X-rays would pass through the sample holder films. The vibrating movement of a piezo-harmonic sample holder aims to move crystals in a random orientation creating a granular convection of the sample powder inside the holder (Sarrazin et al. 2005). The radiation source used is Cu or Co (Koskinen 2018).

The benefits of pXRD are that in principle there is no need for lengthy sample preparation processes except sieving the material to a grain size of <150 μm. Additionally, it requires relatively small sample amount, approximately 15 mg (Olympus 2020; Sarala et al. 2019). However, the samples should remain coarse enough to allow the movement of grains during the measurement since very finely ground samples might get stuck to each other and to the sample holder window (Sarala & Koskinen 2018). Sarrazin et al. (2005) have reported as short as 5-minute data collection time for a complex single mineral sample but proposed longer measurement times for more complex samples with multiple mineral phases.

According to Sarala and Koskinen (2018), major rock-forming minerals such as amphiboles, feldspars, muscovite, quartz, magnetite, and albite can be identified with pXRD. In their study XPowder software was used for mineral interpretation. Several common indicator and heavy minerals were also detected, such as garnet (almandine and pyrope), iron oxides (hematite, magnetite, goethite, and ilmenite), clay minerals (illite, vermiculite and kaolinite), chlorite, biotite, apatite, zircon, monazite, and xenotime.

In the laboratory based XRD results, the presence of ilmenite was very clear, but it was lacking in the pXRD results. The same applied to almandine and talc. Muscovite appeared in the pXRD results, and its amount was heavily emphasized, but it did not appear in the laboratory made XRD results and in addition, the field emission scanning electron microscopy results showed its proportion to be relatively small. An amphibole present in the sample was suggested to be magnesio-hornblende by the laboratory XRD and richterite by the pXRD. Kyanite, xenotime and topaz were only identified by XPowder. (Sarala & Koskinen 2018)

In another study by Sarala et al. (2019) the pXRD results were compared together with the laboratory XRD and the scanning electron microscopy (SEM) results made with two different SEM devices. The pXRD was able to find the same minerals than other methods used except chlorite group minerals and rutile. Biotite, chlorite, and calcite were all almost systematically missing from the pXRD data while pyrite and aeschynite appeared only in the pXRD results, and the amount of pyroxene was exaggerated in the pXRD data. The diffractograms obtained from tailings of Rautuvaara were of specifically poor quality exaggerating the amounts of ilmenite and albite. Additionally, significant amounts of sulphidic minerals were found only with PDXL2 interpretation software, and only small amount of them were detected using the XPowder software.

Sarala and Koskinen (2018) observed that the results obtained by different analytical methods might be drastically different due to multiple factors that effect on the analysis itself. Methodological differences, used databases and the quality of data stored in them as well as varying sample preparation methods might yield to different results. According to Sarala et al. (2019), the diffractogram quality of the pXRD was found to be of worse quality due to shorter measurement time and narrow angular resolution which caused high noise rate to the diffractograms. The angular resolution of the pXRD is 5-55° while in the laboratory XRD it would be 2-120°. Concise angular resolution creates problems with those phases which would fall out of the range, and calcite could be one example that might not become visible in the pXRD diffractograms.

Sarala et al. (2019) and Koskinen (2018) suggested to have long enough a measurement time for pXRD measurements ranging from 15 minutes to 2 hours. This would reduce the noise rate and possibly clarify the diffractogram. The grain size distribution should be as even as possible: in their study it was observed that the best grain size would be within 0.063-0.150 mm range. In this case, less variation, more precision.

Uvarova et al. (2014) studied 200 drill core samples from a pyrite deposit at Nairne, Australia. The samples were measured with pXRD and pXRF and they were validated against the laboratory XRD as well as measurements done of standard samples and a SiO_2 blank sample. The samples were measured with pXRD using the Co anode, the angular range of 5-55°, the angular resolution of 0.25° 2θ FWHM (full width at half maximum) and a measurement time of 10 minutes. Laboratory XRD also used Co anode and had a data collection range of 2θ angle 5-90° with a step size of 0.02° and a measurement time of 7 minutes. The mineral assemblages were quantitatively analysed using RIR-based Diffrac.Eva software and the Rietveld-based Siroquant software. The results showed that the laboratory XRD exaggerated the amount of micas with both quantification methods although the Siroquant results were closer to the reality. On the contrary, phase abundances determined by pXRD were closer to the real ones. In any case, mineral abundances varied according to the instrument and data processing software used.

On the contrary, Burkett et al. (2015) observed a good overall performance between pXRD and laboratory-based XRD devices using the Rietveld-based Siroquant software in quantification. In their research they measured known concentrations with both devices using different measurement times (5, 10, 20 and 40 minutes). However, muscovite seemed to be an exception since it faced certain accuracy issues with lower concentrations (<10 %), which might have much to do with the tendency of plate-like crystals to align their normals with the axis of the sample holder, also known as preferred orientation (Rietveld 1969).

According to Burkett et al. (2015), 5 minutes was long enough a measurement time for qualitative analysis, and this applied also to minor mineral phases. Furthermore, the 5-minute measurement time seemed to work excellently in a quantitative analysis even with minor mineral phases, but the accuracy regarding them improved with longer measurement time.

There are several factors affecting to the reliability and accuracy of the measurements done by pXRD. Main factors affecting to the diffractogram quality are sample treatment procedures that go hand in hand with the grain size of the sample. The grain size distribution might have a significant effect on the quality of the data especially if too large particles are included to the measurement. (Koskinen 2018)

Too coarse sample material can be seen in example as rising of the background of the diffractometer. In any kind of XRD measurements careful preceding sample preparation procedures, such as grinding and milling of the sample for longer periods of time to pulverize it into very fine grain size, aim to homogenize the sample and minimize this effect. Long milling time aims also to avoid sorting due to broad grain size distribution.

However, it is impossible to develop a standard sample preparation procedure suitable for all mineral samples since it depends on the physical properties such as hardness of each mineral how it is broken down. Plate-like crystallites such as muscovite pose their own orientation problems to the sample preparation, and soft minerals such as chlorite and clay minerals might actually become amorphous if they are ground for too lengthy periods. (Billinge & Dinnebier 2008)

According to Sarala et al. (2019), the mineralogy of the sample has also its own effect on the measurement. In example, great differences in the specific gravity of the minerals of the sample, their crystal structure and fluorescence might cause errata to the data. Sample material itself with its amorphous and/or metamictic components naturally affect to the diffractogram quality. Amorphous and badly crystallized materials tend to produce diffraction data of low quality. If the reflections of a mineral would be typically very weak, there would be a risk that they would get drowned to the background noise.

Metamictic minerals such as zircon, allanite, pyrochlore and gadolinite, have loosely bound anions and cations and a distorted crystal structure, and therefore it is difficult to detect them using XRD (Sarala & Koskinen 2018; Sarala et al. 2019). Koskinen (2018) writes that moisture in the sample is another matter that might cause errata to the data. Particles might get clumped due to moisture, and this prevents their free movement in the sample chamber.

One important source of error is related to the magnetic minerals in the sample. If the sample is handled with metallic instruments, in example placed to the sample chamber with a metallic spatula, the metallic instrument attracts the magnetic particles, and they might stay on the surface of the instrument. Treating the sample with metallic instruments might also cause metallic contamination to the sample.

Sarala et al. (2019) notices in their study, that databases used as reference sources for identification might be incomplete and the quality of data might vary dramatically. Some of the interpretation software might lack essential features, such as tools for evaluation the reference data reliability and quality. In addition, Sarala and Koskinen (2018) represent that diffractogram quality might vary and especially in pXRD diffractograms there might be plenty of peaks that are hard to distinguish whether they have actual mineralogical responses or are they only background noise. Due to these peaks (or background noise) the interpretation software tends to suggest multiple different possible diffraction patterns. Since one and same mineral might have a varying elemental composition, it has also various diffraction patterns.

It is upon the person to choose the most matching diffraction patterns from a long list of possibilities, and this requires both knowledge and experience on the method itself. This leads to the fact, that interpretation is strongly human-dependent, and this of course might have an important effect on the results. These facts naturally exclude or at least strongly limit the theoretical possibility of automatic identification of minerals using pXRD.

A sample holder and its correct configuration is one source of error since the sample holder consists of two thin transparent Mylar films and the sample is placed between these films (Fig. 7). If the film is installed inside out, it causes an abnormal measurement result. The films might also break up which might be difficult to detect in the beginning if the breakage occurs within long period of time. This affects to the peak intensity, but the peak location stays the same. The peaks might turn wide, uneven, shallow and are not sharp anymore. The highest peaks might also stay lower than in a normal measurement. (Leväniemi 2020)

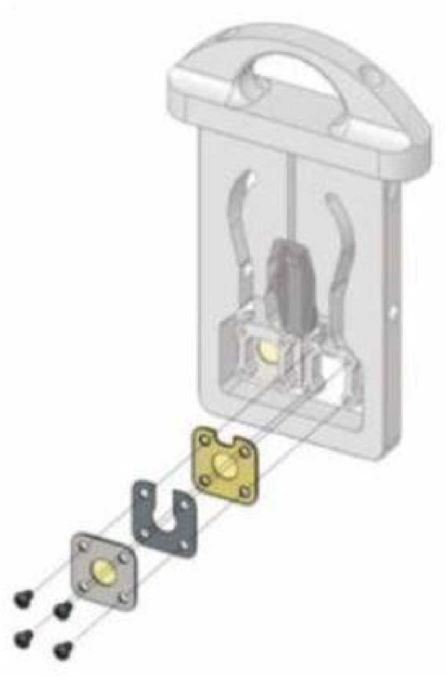

Figure 7. A correct configuration of a sample holder of Terra-542 portable XRD analyser (Olympus 2020).

It is good to be accurate when applying the sample powder to the sample holder since the grains must have enough space to move inside the sample holder but there should be also enough sample. Some minerals can also get packed to the corners of the sample holder, and therefore are not being included in the measurement. (Sarala et al. 2019)

Due to the inaccuracies of the pXRD, it was found out that it is not possible to use it for quantitative analysis: however, phase analysis of common rock-forming minerals is possible, and with some limitations it is possible to analyze accessory minerals (Sarala et al. 2019). However, Koskinen (2018) has represented that the pXRD is not a reliable method even for mineral identification, and that weakly crystalline samples and samples with amorphous phases produce poor diffraction results.

2.2 Spectroscopic methods

2.2.1 Principles of spectroscopy

Spectroscopy is the study of spectra that have been created by interaction of different substances with electromagnetic radiation. It studies light as a function of wavelength that has been scattered, reflected, or emitted from a medium that is in solid, gaseous, or liquid form. When photons penetrate a mineral, some of them would be absorbed while some would just pass through, and some of them are scattered from the surface of the mineral grain. This scattering can be observed and quantified. If the surface would be above the absolute zero, it would emit photons. (Clark 1999)

Human eyes cannot distinguish the infrared waves, but a spectrometer is able to observe and gather information of a wider wavelength range. The spectrometer (or spectrophotometer) is a device meant to measure spectral absorptions. The spectrometers have four variables that describe their competence: 1) spectral range, 2) spectral bandwidth, 3) spectral sampling and 4) signal-to-noise ratio (S/N). The absorption of photons by minerals occurs by different mechanisms. By reflectance or emission of light these different absorption processes and their relation to the wavelength gives information regarding the mineral chemistry. (Clark 1999)

There are certain presumptions that need to be applied when using the reflectance or the emission spectra of minerals. First, the optimal travel distance of the measured electromagnetic energy is the same (Clark & Roush 1984). Secondly, the spectral continuum (or the absorption intensity in relation to the background) of a mineral is considered to be a function of its abundance and the absorption coefficient. Therefore, its abundance can be defined from its absorption magnitude. (Hunt & Ashley 1979; Clark & Roush 1984) Thirdly, the wavelength of the characteristic absorption is controlled by the chemical composition of the mineral (Clark et al. 1990). Finally, scattering is always isotropic (Clark & Roush 1984; Morris et al. 1985).

The frequency bands of the electromagnetic spectrum (Figure 2) are also known as spectral ranges. The ultraviolet (UV) band is located within 0.001-0.4 µm range, and the visible light (VIS) within 0.4-0.7 µm range, followed by the near-infrared (NIR) wavelength range within 0.7-3 µm

(Clark 1999). Spectroscopic and remote sensing literature mentions also the visible, near-infrared (VNIR) wavelength region (~0.4-1 µm) and the shortwave-infrared (SWIR) wavelength region (1-2.5 µm) (Haest et al. 2012): however, in general these are not standard terms even though these spectral ranges are remarkable in geological uses (Clark 1999).

According to Clark (1999), the mid-infrared (MIR) wavelength (3.0-30 µm) hosts also the long-wave infrared range (LWIR, 7-14 µm), that has applications in mineral spectroscopy. Thermally emitted energy belongs also to this wavelength range: in Earth it would begin at 2.5-3 µm ranging up to 10 µm. Finally, there is the far-infrared (FIR) wavelength (30 µm-1 mm) that would have far IR and THF bands. Depending on the literature there is some variation within the wavelength ranges.

Spectral bandwidth describes the broadness of each spectral channel of a spectrometer. If the device has a limited spectral bandwidth, it will limit its capability to measure the absorption features. The bandwidths of a spectrometer should be narrow and spaced close by each other so that the spectrometer could actually measure narrow absorption features. The spectrometers usually use a Gaussian profile as the bandpass profile. The bandpass width is commonly ½ the distance of the frequencies of the function, also known as Full Width at Half Maximum (FWHM). Spectral sampling would describe how far the bandpass profiles of every channel would be as a function of wavelength. Signal-to-noise ratio (S/N) describes the spectrometers ability to do the measurement of the spectrum precisely enough. It is reliant on the subtlety of the detector, the spectral bandwidth, and how strongly the light is reflected or emitted from the material to be measured. (Clark 1999)

Each material has a complex refractive index which means that when a ray of light goes through a substance, it will be always partially attenuated, as expressed in Equation 11:

$$\mathrm{m} = \mathrm{n} - \mathrm{jK}, \tag{11}$$

where m = complex index of refraction, n = the real part of the index, j = $(-1)^{½}$, and K = extinction coefficient (Clark 1999). When the photons enter a substance, they will be absorbed as described already in Equation 3. Equation 12 shows that the complex index of refraction is related to the attenuation/absorption coefficient:

$$\mathrm{k} = \frac{4\mathrm{K}}{\lambda}, \tag{12}$$

where λ = wavelength of light. (Clark 1999)

Absorption happens due to electronic (Burns 1993) and vibrational (Farmer 1974) processes. Burns (1993) represents, that regarding the fundamentals of the electronic processes, in principle individual ions and atoms have energy states distinctive to them. In solid materials, isolated atoms might divide their electrons which can cause the energy level of these shared electrons to distribute over a larger scale known as energy band. According to Clark (1999), when a photon is absorbed, its energy level will change upwards, and when it is emitted, its energy state will change downwards. The emission of a photon commonly does not occur at the same wavelength than the absorption.

Crystal field effects are electronic processes related to insufficiently filled d sub-shells of transition metals (often Fe, but also Co, Ni, Cr and so on). In principle, an individual ion of the d orbital in any transition metal would have the same energy level (Burns 1993). When an atom of a transition metal would be placed within a crystal field, the energy levels divide shifting an electron from a lower to higher state. The valence state (like Fe^{2+}) and the coordination number of the atom influence on the energy levels, as well as the symmetry of the site where the atom is attached to (Clark 1999). Ligand types and metal-ligand interatomic distances have also an effect on the energy levels (Burns 1993).

These effects depend on the crystal structure of each mineral, and due to this variation, each ion is able to generate variable absorptions. This phenomenon allows the recognition of minerals using spectroscopy. Other electronic processes related to the absorption bands include charge transfers of electrons due to absorption of a photon, band gaps between conduction bands and valence bands, and colour centres caused by lattice defects due to in example impurities in a crystal. (Clark 1999)

In the vibrational processes, the molecules or the crystal lattices oscillate. These processes depend on the molecular bonds and the masses of the elements involved in the molecule. This kind of absorption is visible in the infrared spectrum when the molecule would be infrared active, or in other words, expresses a dipole moment. In this process molecules move and rotate, but they might also rotate partially or do not rotate at all. The latter is known as lattice mode. (Clark 1999)

2.1.2 Imaging spectroscopy in mineralogy

Imaging spectroscopy is a method that gathers and processes data from the electromagnetic spectrum. It has multiple names in use including hyperspectral imaging and imaging spectrometry, and the terminology can be relatively confusing. While spectroscopy studies electromagnetic radiation, spectrometry quantifies photons as a function of wavelength. Using the expression ‘hyper’ would be slightly exaggerating since it would refer to something enormous, and the coverage of most of the contemporary spectrometers would be some hundreds or, in maximum, thousands of channels instead of millions. Therefore, the recommended term to be used would be imaging spectroscopy. (Clark 1999)

Recent applications of imaging spectroscopy techniques applied in geology include in example identification of overall mineralogy (e.g., Clark 1999; Sarala et al. 2019), quantification of chemical composition of glacial till (Middleton et al. 2011), mineral exploration (Herrmann et al. 2001; Sun et al. 2001), REE ore grade estimation (Turner et al. 2014), alteration feature identification (Jones et al. 2005; Laukamp et al. 2011; Harraden et al. 2013; Sarala et al. 2019), drill core logging (Squire et al. 2007), and outcrop mapping by combining remote-sensing and hyperspectral techniques (Booysen et al. 2021a; Booysen et al. 2021b).

In imaging spectroscopy, before the measurement no sample preparation is needed except swiping away excess dust and having the sample dry during the measurement (Thompson 1999). During the measurement a ray of light of a spectrometer is pointed to the sample. The ray proceeds through the optical fiber cable to the measuring device where the visible life diffracts to different wavelengths. The receiver counts the number of photons that arrive to the receiver. Photons will be converted to electrons and will be stored as a characteristic time period. Electrons are then converted to voltage which receives a digital number (Clark 1999; Thompson 1999).

The result of the measurement will be a spectrum (Fig. 8), represented with a wavelength (in nm) on X-axis and reflectance on Y-axis. The absorption peak of the spectrum describes the area where the photons are absorbed in a certain molecular structure. The location, width and depth of the absorption peak contain information on the minerals. In principle, minerals with similar crystallographic structures and chemical compositions would have alike spectra. However, there might be delicate differences in the locations, depths, or outlines of the absorption spectra. (Thompson 1999)

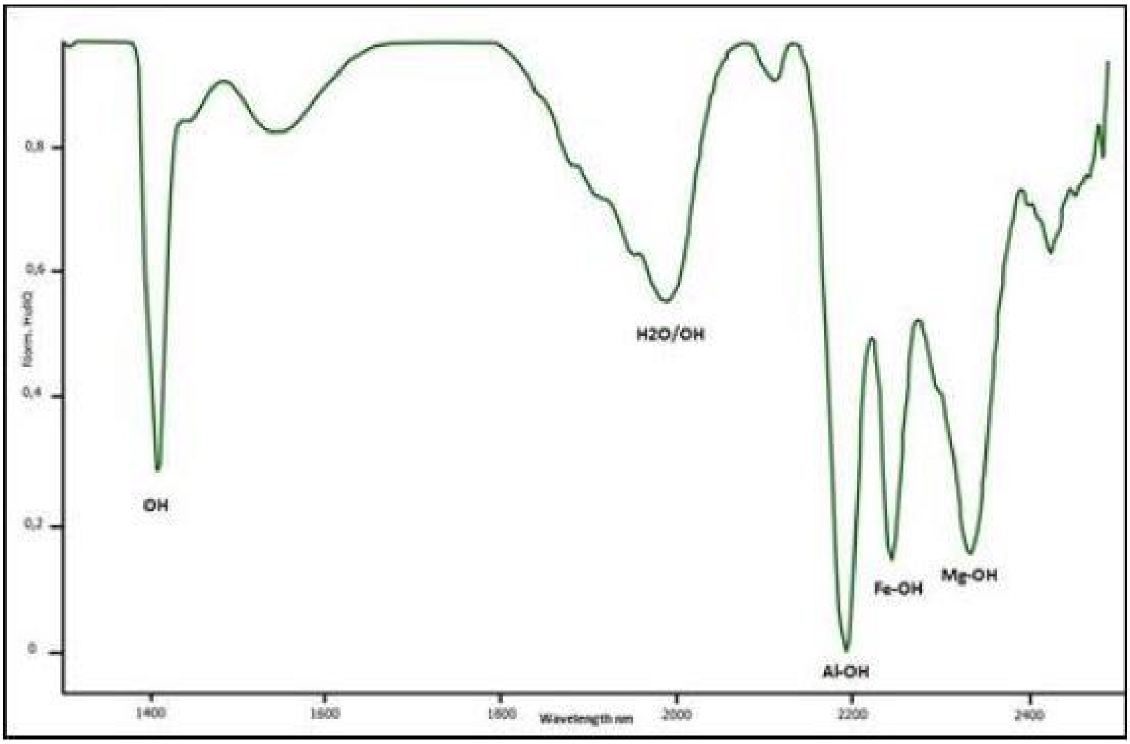

Figure 8. An example spectrum with characteristic peaks within visible, near-infrared (VNIR) and short-wave infrared (SWIR) wavelength regions (Leväniemi et al. 2020).

As depicted in Table 2, the VNIR wavelength region includes several iron oxides, iron hydroxides, iron sulphates, some amorphous phases such as ferrihydrite (Clark 1999), and REEs (Clark 1999; Booysen et al. 2021a). Olivine and pyroxene also have some of their characteristic absorption bands within the VNIR wavelength region (Clark 1999), like Fe^{2+} absorption features of olivine caused by crystal field transitions (Isaacson et al. 2014). However, their most distinguishable absorption features are located within the LWIR wavelength region (Clark 1999). In the case of olivine it is important also to remember that pure olivine with a formula of [$(Mg,Fe)_2SiO_4$] is not abundant in the Finnish bedrock but tends to be altered, and the VNIR reflectance features can be altered due to the substitution of minor cations such as Ni^{2+} or Cr^{2+} (Isaacson et al. 2014). The spectral characteristics of pyroxenes might also get affected by oxidation due to metamorphosis (McCanta & Dyar 2020).

Table 2. Spectrally diagnostic minerals (adopted from Booysen et al. 2021a). VNIR = visible, near infrared (0.4-1 µm), SWIR = short-wave infrared (1-2.5 µm) and LWIR = the long-wave infrared (7-14 µm) wavelength regions. Minerals appearing within 0.4-2.5 µm (VNIR and SWIR wavelength regions) are included in this study.

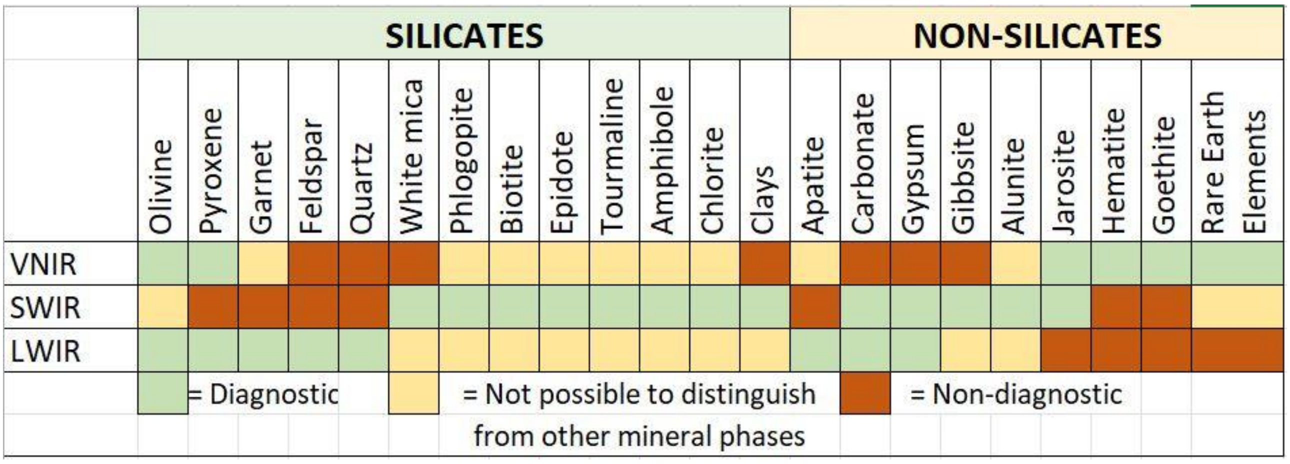

	SILICATES													NON-SILICATES								
	Olivine	Pyroxene	Garnet	Feldspar	Quartz	White mica	Phlogopite	Biotite	Epidote	Tourmaline	Amphibole	Chlorite	Clays	Apatite	Carbonate	Gypsum	Gibbsite	Alunite	Jarosite	Hematite	Goethite	Rare Earth Elements
VNIR	🟩	🟩	🟨	🟧	🟧	🟧	🟨	🟨	🟨	🟨	🟨	🟨	🟧	🟨	🟧	🟧	🟧	🟨	🟩	🟩	🟩	🟩
SWIR	🟨	🟧	🟧	🟧	🟧	🟩	🟩	🟩	🟩	🟩	🟩	🟩	🟩	🟧	🟩	🟩	🟩	🟩	🟩	🟧	🟧	🟨
LWIR	🟩	🟩	🟩	🟩	🟩	🟨	🟨	🟨	🟨	🟨	🟨	🟨	🟨	🟩	🟩	🟩	🟨	🟨	🟧	🟧	🟧	🟧

🟩 = Diagnostic 🟨 = Not possible to distinguish from other mineral phases 🟧 = Non-diagnostic

Iron oxides play an important role in mineral exploration since they might be the only visible hint of mineral deposits in the target. Their characteristic spectra are located within the VNIR wavelength region between 800-1000 nm (Cornell & Schwertmann 2003). In terms of spectral characteristics, these substances are complex, and there is a vast variation in the shapes of the absorption bands and positions (Clark 1999). In altered rocks, the spectral features appearing under the 1200 nm wavelength region are caused by different electronic transitions where iron is also associated (Hunt & Ashley 1979). However, the rare earth elements have their electrons so well protected from crystal fields close by so their energy levels do not vary that drastically. That is why they can be identified due to the existence of the ions in the mineral phase instead of their mineralogical features. (Clark 1999)

The SWIR wavelength region covers a large part of the rock-forming minerals, both silicate and non-silicate minerals. The wavelength region within 1300-2500 nm is especially important since the molecular bonds of the molecules OH, H_2O, AlOH, MgOH and FeOH are located within this region

(Thompson et al. 1999) which would be characteristic to several hydrous sulphates and carbonates as well as hydroxylated silicates (Squire et al. 2007). Silicate minerals include amphiboles, chlorite, white mica, epidote, tourmaline, phlogopite, biotite, and clay minerals. Non-silicates include carbonates, gypsum, gibbsite, alunite, and jarosite (Booysen et al. 2021a). The characteristic features within this spectral range are due to vibrational transitions (Hunt & Ashley 1979).

Third important wavelength region regarding the mineralogy would be the LWIR wavelength region including many important rock-forming silicate minerals such as quartz, feldspars, olivine, pyroxene and garnet, and non-silicate minerals like apatite, carbonates, and gypsum. (Booysen et al. 2021a)

The SWIR spectroscopy has had several beneficial applications in mineral exploration in epithermal porphyry, Fe-oxide-Cu-Au and VMS deposits (e.g., Thompson et al. 1999; Herrmann et al. 2001; Jones et al. 2005; Maydagán et al. 2018; Booysen et al. 2021b). Regarding the mineral exploration, a special interest is paid on certain features detectable with the SWIR spectroscopy, such as subtle variations of phyllosilicates (Harraden et al. 2013), phengitisation, and paragonitisation (Yang et al. 2011). Chlorite, white mica, and clay minerals have been used as ore vectors in example in porphyry deposits, and therefore there is a great interest in observing them in the spectroscopical data (Maydagán et al. 2018). The typical absorption spectra of white mica, chlorite and their mixture are represented in Figure 9.

White micas are one group of minerals of specific interest, and they appear within 2190-2228 nm wavelengths depending on the amount of Al in their composition (Jones et al. 2005). ‘White mica’ is a broadly used term that refers to a group of dioctahedral sheet mica that are often formed in medium-grade metamorphic conditions, and whose formation is connected to hydrothermal alteration. It refers to a muscovite-paragonite-celadonite solid solution series (Velde 1965). ‘Sericite’ is an often-used alternative term referring to the group of minerals belonging to the term ‘white mica’, and it is used to mean white mica of fine grain size that is formed due to hydrothermal alteration (Yang et al. 2011).

There is plenty of compositional variation within the white mica, described as $(K, Na)^{it}_{2}(Al, Fe, Mg)^{vi}_{4}(Si, Al)^{iv}_{8}O_{20}(OH)_{4}$. The formula describes the cations situated between layers, and iv and vi would be tetrahedral and octahedral locations. This chemical variation is usually due to Tschermak substitution. Phengite would be the midway composition of the muscovite-celadonite solid-solution series commonly occurring in metamorphic rocks formed often in high pressure conditions, having a composition of $Si^{iv}(Mg, Fe)^{vi} \leftrightarrow Al^{iv} Al^{vi}$ and an Si/Al ratio of >3/1. The substitution of Fe and Mg would refer to muscovite $[K_{2}Al_{4}(Si_{6}Al_{2})O_{20}(OH)_{4}]$ and celadonite $[K_{2}(Mg, Fe^{2+})_{2}(Al, Fe^{3+})_{2}Si_{8}O_{20}(OH)_{4}]$ (Velde 1965). The chemical variation of white mica is connected to physical and chemical factors, including pressure, temperature, pH, and chemical consistency (Velde 1967; Massonne & Scheyrer 1987).

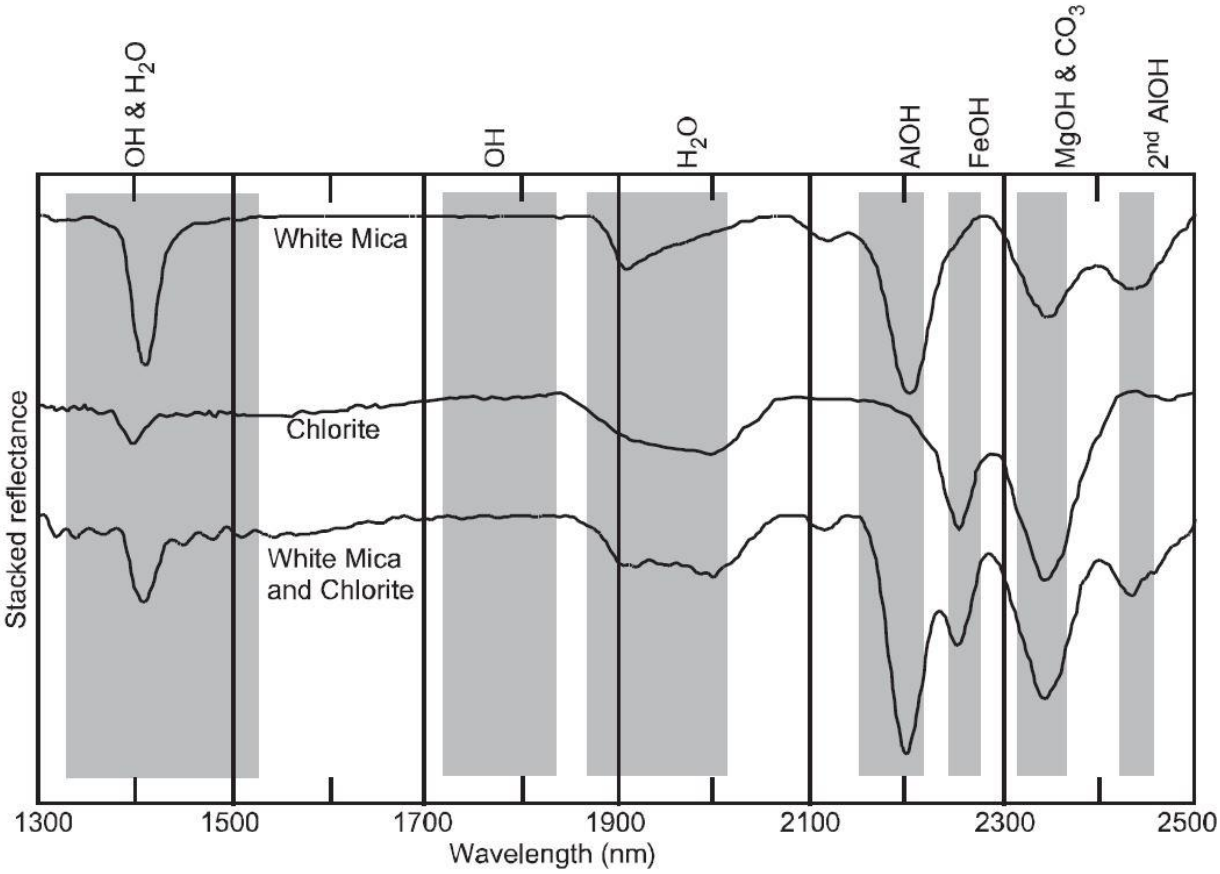

Figure 9. Short-wave infrared (SWIR) absorption spectra (Hull quotient corrected) of white mica, chlorite, and their combination (Jones et al. 2005, modified from Herrmann et al. 2001).

One of the endmembers is paragonite, the Na-rich mica, formed from Na substituting for K (Guidotti et al. 1994). Paragonite is perhaps not that common a mica: however, in VMS systems it might appear proximal to ore (Hannington et al. 1998; Herrmann et al. 2001; Jones et al. 2005). According to the study of Squire et al. (2017) at a high-sulfidation epithermal Au-Cu deposit of Peak Hill, Australia, muscovite would have its AlOH spectral features within 2200-2210 nm while paragonite would appear in the lower wavelengths of <2200 nm.

Sericitic, argillic, and advanced argillic alteration areas are important types of alteration when characterising VMS deposits (Bonnet & Corriveau 2007). Using the SWIR spectroscopy, it is possible to distinguish assemblages of phyllosilicates like illite, sericite, kaolinite and pyrophyllite by observing spectral absorption features within 1300-2500 nm. It is difficult to distinguish them from each other only by visual observation, but the SWIR spectroscopy can present more precise information of their variation. Considering the genesis of the ore this is important since different clay types might be genetically connected to the distribution of metals of interest (Harraden et al. 2013). Minerals in different alteration zones of VMS systems are represented in Table 3.

Jones et al. (2005) have studied the hydrothermal alteration zones of a VMS deposit of Myra Falls, Vancouver, British Columbia. It was found out that AlOH absorption in lower wavelengths (<2198 nm) correlates to reduced Fe, Fe + Mg, and Si/Al contents as well as greater Na/(Na + K) contents referring to sodic muscovites, referred as paragonite in other literature. These were located next to the ore deposit. AlOH absorption in higher wavelengths (>2206 nm) would show higher Fe, Fe + Mg, and Si/Al values and lower Na/(Na + K) values referring to phengitic, non-sodic muscovites in the distal part of the formation. There were elevated Zn, V, Fe and Mg contents in white mica proximal to the ore than in the distal part of the deposit. Systematic alteration correlating with the distance from the ore was observed in the case of chlorite group minerals: intermediate Mg-chlorite was proximal to ore while intermediate Fe-chlorite would have been further from the ore.

Table 3. Minerals in the VMS alteration system zonation (after Shanks 2012). Minerals in bold can be detected within the short-wave infrared (SWIR) and visible, near-infrared (VNIR) wavelengths.

	Diagnostic minerals		
Alteration type	Unmetamorphosed deposits	Greenschist facies	Granulite facies
Advanced argillic	**Kaolinite, alunite, opal, smectite**	**Kaolinite, topaz, pyrophyllite,** corundum, andalusite	Sillimanite, kyanite, quartz
Argillic	**White mica, illite, smectite, pyrophyllite, opal**	**White mica, illite, pyrophyllite**	Sillimanite, kyanite, quartz, **biotite,** cordierite, garnet
Sericitic	**White mica, illite, opal**	**White mica, illite,** quartz	**Biotite**, K-feldspar, sillimanite, kyanite, quartz, cordierite, garnet
Chloritic	**Chlorite, opal,** quartz, **white mica**	**Chlorite,** quartz, **white mica**	Cordierite, **phlogopite,** orthopyroxene, **orthoamphibole,** sillimanite, kyanite
Carbonate propylitic	**Carbonate (Fe, Mg), epidote, chlorite, white mica,** feldspar	**Carbonate (Fe, Mg), epidote, chlorite, white mica,** feldspar	**Carbonate**, garnet, **epidote, hornblende,** diopside, orthopyroxene

It is also possible to observe the chemical variation of chlorite group minerals by studying their typical absorption features of FeOH and MgOH. However, it has been found out that observing the compositional variation of chlorite is not reliable with samples with small quantities of chlorite compared to white mica, or where chlorite occurs together with epidote. The SWIR spectroscopy of chlorite can be used to study and define low-grade metamorphic rocks like pelites using a method called chlorite spectral index (CSI) (Doublier et al. 2010; Doublier et al. 2012). FeOH absorption feature position changes have been used successfully for ore vectoring in the Izok Lake VMS deposit where Mg-rich chlorite and biotite were found to be proximal to ore (Laakso et al. 2016).

According to Sarala et al. (2019), using the VNIR and the SWIR wavelengths in imaging spectroscopy with a pixel size of approximately 1.5 mm and measuring the soil in situ it was possible to identify clay minerals, Fe-oxides, and hydroxyl group and water containing minerals. Alteration zones were also identified. The VNIR and the SWIR analysis was fulfilled with the LWIR wavelength measurement, and garnet, pyroxenes, amphiboles, and zircons were also found in analyzed heavy mineral concentrates. When two heavy mineral concentrates were imagined with an equipment using only the SWIR camera, part of the heavy minerals were left unidentified. If typical main minerals of the samples were chlorite, quartz, apatite, and Fe-oxides, then the only ones detected were illite-kaolinite clays, some amphiboles, epidote, and Fe-oxides. Amphiboles were also observed to have been changed partially to Mg-clays (saponite) due to water absorption.

The spectral features of hydrothermally altered rocks do shift due to weathering: in fact, weathering can cause chlorite group minerals to disappear while white micas would be more resistant to weathering. However, weathering of white micas moves their typical primary absorption feature, which would be normally close to 2200 nm. Al-abundant white micas with an absorption wavelength less than 2198 nm showed a transfer to higher wavelength region of 2200-2202 nm and Al-poor white micas with the normal absorption wavelength more than 2208 nm moved to shorter wavelength region of 2205-2208 nm. White micas of intermediate composition were reported to be stable during weathering events. Regarding the alteration mapping, the white micas are more potential since they tolerate some weathering while chlorite would simply weather away. (Ehara Suryantini et al. 2005)

Water and hydroxyl (OH) groups produce their own characteristic absorption bands allowing to distinguish minerals containing them. The OH group has its first absorption band in 1400 nm, and the H-O-H bond with OH branches are observed close to 1900 nm. If a mineral would have an absorption band at 1900 nm, it would contain water. If it has only the absorption band in 1400 nm but not in 1900 nm, it would contain only the OH group. However, the OH group has several possible locations within a crystal lattice, and therefore there might be several OH features in a spectrum. (Clark 1999)

Carbonates produce characteristic vibrational absorption bands because of their CO_3^{-2} ion (Clark 1999). Characteristic spectral features of carbonate minerals like calcite and dolomite can be used to identify the purity and mixing of these minerals in a sample. Zaini et al. (2012) have observed that variation in grain size and mineral consistency within the sample effect on the characteristics of absorption features as well as reflectance values in calcite and dolomite samples in measurements made within SWIR and TIR wavelength regions. Varying grain size caused displacement of absorption band placements as well as changes in the FWHM and asymmetry of the spectral features of both minerals.

3 Volcanogenic massive sulphide deposits

3.1 Formation of volcanogenic massive sulphide deposits

The VMS deposits are base and often also precious metal accretions that are formed in a submarine setting (Hannington 2014). They belong to a bigger group of massive sulphide deposits (Lydon 1984). The VMS deposits have formed when warm, hydrothermal fluids have precipitated, circulated, and accumulated on top of and below the seafloor close to the vents of epithermal hot springs or black smokers, kind of submarine volcanoes (Hannington 2014).

The formation of the VMS is related to the process of partial melting of the crust and submarine hydrothermal volcanism (Hedenquist & Lowenstern 1994). Due to the partial melting metals gradually ascend through the crust and concentrate to the residual magma or hydrothermal fluid. The hydrothermal fluids are convectively circulated on top of a heat source, such as a magma chamber beneath a volcano (Fig. 10). The submarine hydrothermal system can be divided into three zones: the discharge zone on the top, the upflow zone in the middle and the reaction zone beneath (Franklin et al. 2005; Hannington 2014)

Similar between the VMS and sedimentary exhalative deposits (SEDEX), the close analogues of the VMS, is the precipitation of metals on top of and below a sea floor due to hydrothermal metal-rich sulphidic fluids that circulate in the rock. The saline seafloor basin is an anoxic environment, which is ideal for sulphide precipitation of the metalliferous brines via bacterial reduction. Bacteria-aided sulphide reduction might be in important role in formation of the VMS deposits as well. Within time the heavy metal-rich brine has been captured to a faulted sub-basin and sulphides will be deposited to the sea bottom. (Robb 2005)

In the VMS systems the host rocks of the ores are usually volcanic or volcanosedimentary, such as felsic or mafic tuffs or lavas, robust breccias, and rhyolitic domes (Lydon 1996). In Precambrian areas a promising environment for the VMS deposits would be high-temperature rhyolites: however, the occurrence of the VMS deposits is not limited only to these lithologies (Galley et al. 2007). In Phanerozoic environments there is a large variation in the VMS-associated mafic and felsic lithologies (Piercey 2009).

VMS deposits can be identified of synvolcanic structural features like calderas, growth faults, and intersections of faults that might have acted as structural controls of the ore, and perhaps fine-grained sedimentary rock units with graphite or high carbon contents that would indicate pauses in the volcanic activity. These units might even represent anoxic or sulphidic waters in the sea bottom that have thwarted oxidation of sulphides and weathering of the sea bottom. (Goodfellow et al. 2003) Synvolcanic dikes and sills might have been a heat source of the hydrothermal system and are usually connected to its footwall (Galley 1993). Within the prospect there might be known sulphidic mineralizations with a structural control and discordant veins, and within some distance of the mineralizations there might be Ba-containing or Cu-, Zn- and Pb-rich exhalites (Spry et al. 2000). Profuse amounts of white mica, chlorite (Galley et al. 2007) and tourmaline (Taylor & Slack 1984) act as clues of hydrothermal alteration related to the VMS.

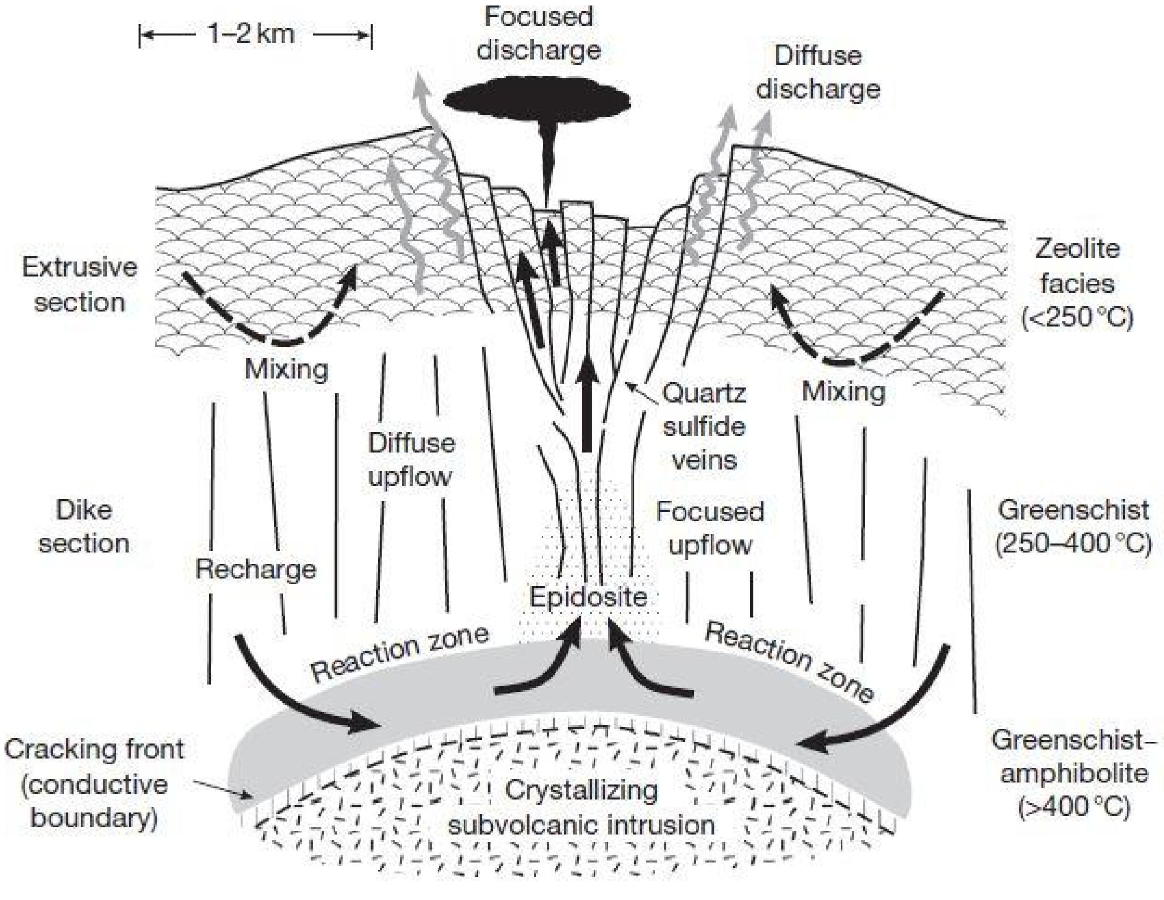

Figure 10. Schematic representation of a submarine hydrothermal system divided into discharge zone on the top, upflow zone in the middle and the reaction zone beneath (Hannington 2014, adapted from Alt 1995).

“Black smokers” are chimney-like pipes in extensional, volcanically active areas by mid-ocean ridges that vent above the sea floor hot, somewhat acidic, metal-rich and reduced hydrothermal fluids. Before entering the black smokers, the fluids are usually originally of sea water, that is initially cold, oxidizing and depleted of metals. Sometimes there might be a small magmatic fluid constituent involved. In the VMS systems these fluids leach the basaltic rocks of oceanic crust and by this process, the forming hydrothermal fluids become enriched in metal ions. When this fluid is heated up, it starts to ascend towards the sea bottom. In VMS systems, thermal energy usually comes to these systems from magmatic sources (Hedenquist & Lowenstern 1994). In addition, degassing magmas can separate metals from the source magma in favorable conditions. The quantity of sulphidic mineral in hydrothermal fluids is connected to the temperature and pH of fluids, cooling of the fluid during its adiabatic rise, and the amount of mixed fluids on the sea floor (Franklin et al. 2005).

Hydrothermal alteration is caused by warm hydrothermal fluids circulating in the bedrock. In the VMS systems, when the fluids circulate in the host rock, metamorphic alteration processes like chloritization, silicification, hydrolysis, carbonatization, epidotisation, albitization, anhydrite precipitation and argillic alteration occur, and metals precipitate (Franklin et al. 2005). These alteration processes, namely advanced argillic, chloritic, siliceous, and carbonate alteration can be used to find the VMS deposits (Bonnet & Corriveau 2007).

Tectonic settings of the VMS deposits are varying, but most commonly they are rift systems located on the mid-ocean ridges, along convergent plate margins where oceanic crust subducts beneath continental crust and volcanic arcs form. There are five lithostratigraphic groups of VMS deposits: 1. A bimodal-mafic group related to the beginning rifting of supra-subduction oceanic arcs. 2. Mafic group would refer to primitive oceanic back arc context, and 3. pelite-mafic setting to more mature oceanic back arcs. 4. Bimodal-felsic group is connected to the beginning rifting of supra-subduction epicontinental arc, and 5. siliciclastic-felsic group would take place in mature epicontinental back arc setting. (Franklin et al. 2005)

3.2 Mineralogy and structure of volcanogenic massive sulphide deposits

The VMS deposits are significant sources of base metals Zn, Cu and Pb: they host over 60 % sulphidic minerals, like pyrite, pyrrhotite, chalcopyrite, galena, and sphalerite, as well as native Ag and Au. Therefore, their role as a source of copper, zinc and lead is significant. The Cu-Zn deposits are commonly deposited on higher temperature conditions (up to 400 °C) on mafic volcanic rocks and have only limited amount of Pb while Zn-Pb-Cu deposits are deposited on felsic volcanic or sedimentary units in lower temperature conditions (Franklin 2005; Galley et al. 2007; Hannington 2014). The gangue minerals of the VMS deposits would be quartz, chlorite, gypsum, carbonates, and barite (Lydon 1984).

Zoning is characteristic particularly to the VMS deposits (Fig. 11), and it describes the movement of major elements in the upflow zone when the hydrothermal fluids are reacting with the rocks (Bonnet & Corriveau 2007). The zones are closely related to the temperature but also to the evolution of the fluids that have circulated in the rocks: however, the zones are formed when sulphidic minerals begin to precipitate from the hydrothermal fluids. In a classical VMS deposit, the center part contains a massive, zoned sulphide ore lens located close to the vent and below it a pipe-like structure (Lydon 1984).

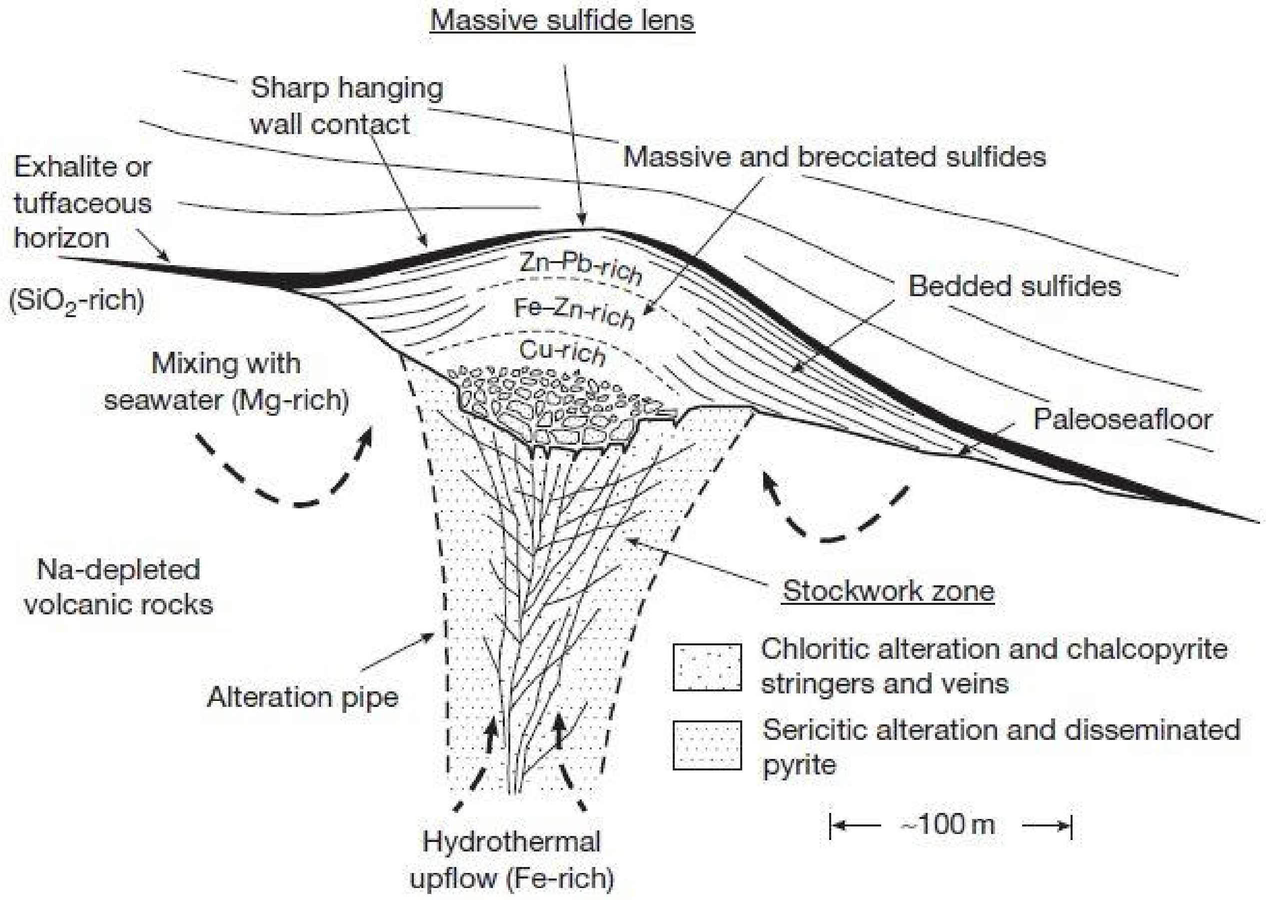

Figure 11. A cross-section of a classical volcanogenic massive sulphide deposit (Lydon 1984).

Mineralogy depends on the VMS deposit, but in Cu-Pb-Zn VMS deposit closest to the vent entrance there is a zone containing pyrite, chalcopyrite and possibly gold, formed in 300-350 °C. Above it there is another zone with sphalerite, chalcopyrite, pyrite and possibly galena, formed in 250-300 °C. The furthermost zone is formed in 250 °C and consists of sphalerite, galena, and pyrite, and possibly some gold, anhydrite and baryte (Lydon 1984). If the temperature would rise above 310 °C, the concentration of Zn would rise, and above 320 °C the contents of Fe and Cu would rise. Even though the temperature change is relatively small, it is enough to produce zoning between Cu occurring within higher temperature conditions, and Zn occurring in cooler temperatures (Large 1992).

Beneath the core there is a pipe-shaped stockwork/stringer zone consisting of disseminated sulphides in addition to heavy chloritization, surrounded by altered footwall rocks. Stringer zone tends to be a pipe-shaped zone wrapped to metamorphosed footwall sedimentary and/or volcanic rocks and might host disseminated or vein-type sulphide mineralizations. An exhalite or tuffaceous horizon is a typical feature above the whole structure that might reach tens on kilometres off the deposits. (Lydon 1984)

4 Geology

4.1 Regional geology

The bedrock of Finland is part of the Precambrian East European craton, which is located in the northern and eastern parts of Europe as well as northwestern Russia. Finland, Sweden, Norway, and northwestern part of Russia belong to Fennoscandia, and the area of Finland covers 1/3 of the Fennoscandian shield. The Finnish part of the Fennoscandian shield can be divided into four tectonic provinces: Karelia, Svecofennia, Norrbotten, and Lapland-Kola. Whole southern Finland belongs to the Svecofennia Province. (Luukas et al. 2017; Nironen 2017)

While the Karelia Province contains the oldest, Archaean bedrock sequences in Finland, the Svecofennia Province is constructed mostly of Paleoproterozoic material (Lehtinen et al. 2005). Due to the Paleoproterozoic Svecofennian orogeny 1.92-1.77 Ga (Lehtinen et al. 2005) new crust formed to the southern and central Finland by accretion of Southern and Western Finland arc complexes towards the Archaean mainland (Nironen 2017). This event initiated of a collision of several volcanic arcs and microcontinents, clearly separating the Svecofennia from the older Karelia province creating a major part of the Fennoscandian Shield (Lehtinen et al. 2005). During the orogeny, volcanic rocks of island arc -type and mafic to ultramafic intrusions penetrated to older more mixed and even turbiditic material. Supracrustal rocks accumulated on the sea floor, and after this, the Svecofennian orogeny thrusted and folded them to their current locations (Nironen 2017).

Crustal thickness of the Svecofennia Province resulted of crustal components placed upon each other during the collision. Mantle-derived magmas were intruded into the collision zone, resulting to the melting of the lower crust and this led to temperature rise on the upper parts of the crust as well. This caused partial melting and recrystallization of crustal rocks (Lehtinen et al. 2005), and formation of a large part of granitoids in Svecofennia Province (Lehtinen et al. 2005). There are also some mainly island arc-type volcanites usually occurring in groups mostly formed between 1.90-1.88 Ga, but in the northeast of Svecofennia Province the volcanites are bit older, approximately 1.93-1.91 Ga. These volcanites were injected into older turbiditic bedrock that are currently metamorphosed as metagreywackes and biotite paragneisses (Kähkönen 2005).

The end of the Svecofennian orogeny was when the Volgo-Sarmatian protocontinent collided with the Fennoscandian protocontinent in 1.82-1.80 Ga forming a new continent Baltica causing also transpressional deformation in southern Finland. After the Svecofennian orogeny there was a crustal stabilization time at 1.76-1.65 Ga (Nironen 2017). It was followed by rapakivi magmatism 1.65-1.54 Ga that is characterized by bimodal magmatism caused by intracontinental rifting (Lehtinen et al. 2005). On one hand there were felsic granites formed and on the other hand basic rocks, like anorthosites, gabbros and diabases. Crustal thinness and protruding mantle in these areas refer to extensional formation environment. In southern Finland there are also mafic dyke swarms coeval with rapakivi magmatism (Aro & Laitakari 1987).

4.2 Metsämonttu

Metsämonttu succession (Fig. 12) is a hydrothermal VMS Zn-Pb-Cu-Au-Ag deposit in the southwestern Finland. According to Nironen (2016), Metsämonttu is located in the southwestern part of the Orijärvi formation belonging to the Aijala Member of Kisko group. They are a part of the Paleoproterozoic 1.90-1.88 Ga old Uusimaa belt (Väisänen & Mänttäri 2002).

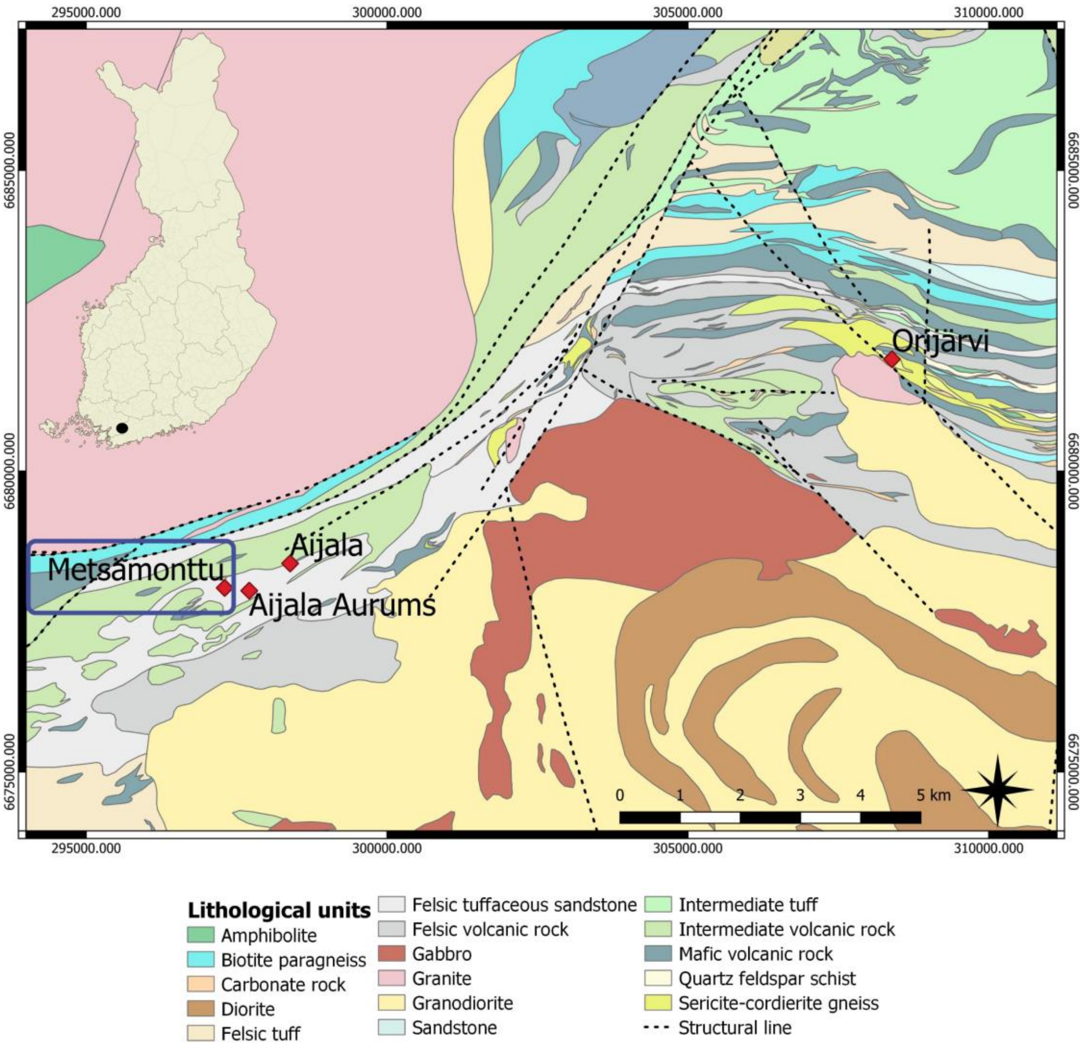

Figure 12. Geological map of the Aijala-Orijärvi area. Metsämonttu is located in the Aijala Member of the Orijärvi Formation (Nironen 2016). Geological maps: Bedrock of Finland scale free, modified data © Geological Survey of Finland (2021).

The rocks within the area of Orijärvi have been formed in a volcanic arc system 1.89 Ga years ago (Kähkönen 2005), in the early stages of an evolution of a volcanic arc complex in an extensional tectonic context (Väisänen & Mänttäri 2002). During the operational time of the Metsämonttu mine, altogether 1.5 megatons of ores were mined with average ore grades of 3.34 % Zn, 0.74 % Pb, 0.28 % Cu, 24.8 g/t Ag, 1.4 g/t Au (Puustinen 2003).

According to Nironen (2016), the Kisko group stratigraphically consists of five formations: Orijärvi, Vetio, Metsäkulma, Ahdisto and Salittu formations. They are bordered to the "Orijärvi triangle" area except the Salittu formation. In general, there has been great interest in the research of altered rocks of Orijärvi area (e.g., Eskola 1914, 1915; Schneiderman & Tracy 1991; Väisänen & Mänttäri 2002). Most importantly, the studies of Pentti Eskola made in Orijärvi led to the creation of metamorphic facies classification (Eskola 1915).

4.3 Metsämonttu deposit

The Metsämonttu deposit was found by Suomen Malmi Oy in the regional electromagnetic (EM) surveys in 1945. In 1948-1949 more precise surveys were done using the EM and magnetic methods (Outokumpu Oy, unpublished). The aeromagnetic data from the study area represent distinctive anomalies around Metsämonttu and Aijala as well as other ore targets of the Aijala-Orijärvi VMS zone, especially when approached the actual ore deposits (Koskela et al. 2019; Leväniemi & Hokka 2021). Magnetic measurements done in the 1940s show also, that Metsämonttu would be a part of the same sequence than Cu-Zn ore of Aijala (Raja-Halli 1949). The deposit is well detectable by magnetic and electric measurements (Koskela et al. 2019), and maps representing magnetic anomalies describe well measures, shape, position and at least to some degree also the quality of the sphalerite ore deposit of Metsämonttu (Suomen Malmi Oy 1949).

Four different metallic mineralization types have been identified from the area of Orijärvi. Metsämonttu, Aijala and Orijärvi belong to the first type consisting of Zn-Cu ± Pb, Au VMS mineralizations. There are some potential epithermal Au ± Cu mineralizations in the northern part of the area, banded iron formations (BIF) around Jussarö and Nyhamn, and small occurrences of skarn iron ores throughout the whole area (Eilu et al. 2012). It is important to notice that nearly all known ore deposits containing sulphides and oxides are located in the Aijala Member (Latvalahti 1979). Mining activities in Metsämonttu took place in two different time periods. The deposits closer to the surface level were mined in 1949-1958 and the deposits located deeper were mined in 1963-1974 (Warma 1975).

According to the description of Latvalahti (1979), Aijala-Orijärvi area hosts volcanic rocks that are mainly volcanoclastic, with some sequences originating from lava sources. Chemically they fall to calc-alkalic category, but there are some units containing tholeiitic compositions. Figure 13 shows that the area of Metsämonttu is located within felsic tuffaceous sandstones, and in the proximity of the contact of felsic volcanites and intermediate pyroclastic volcanites. There are three old mines within the area including Aijala Mine, Metsämonttu mine and Aijala-Aurums, a pit where some Pb ore was quarried.

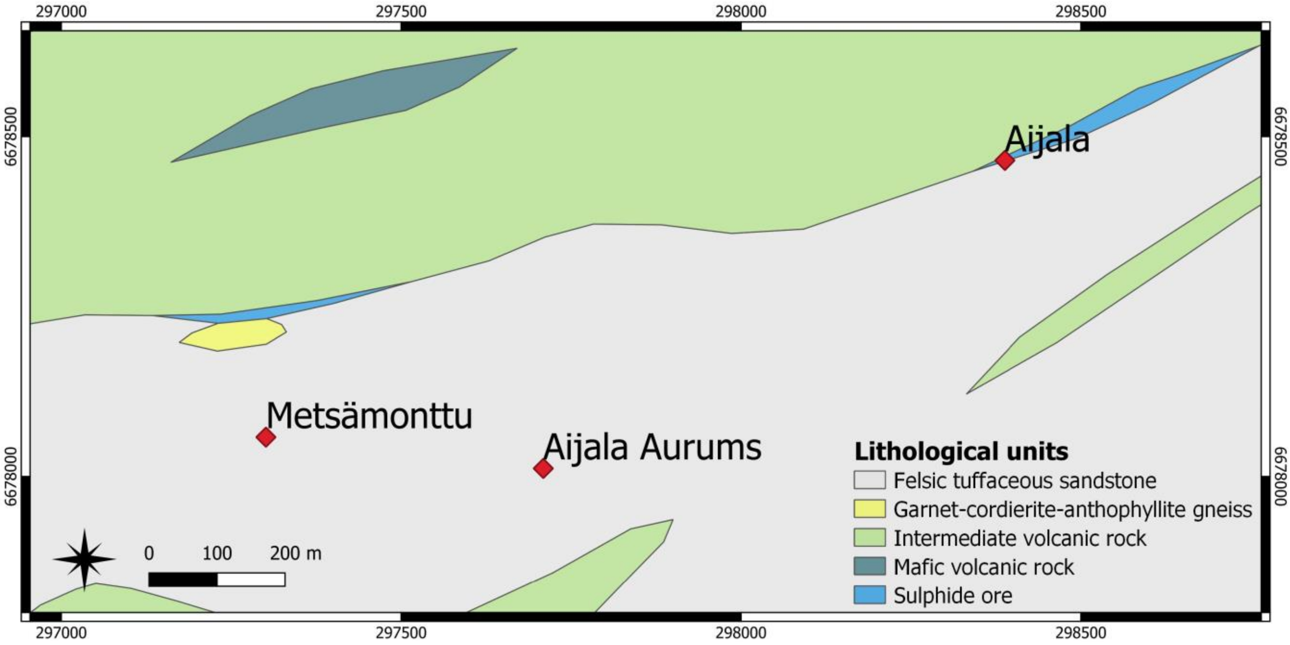

Figure 13. Regional geology of the Aijala-Metsämonttu region (Bedrock of Finland scale free, modified data © Geological Survey of Finland [2021]).

The altered lithologies of the area of Metsämonttu include different gneisses (cordierite mica, andalusite-cordierite-muscovite and cordierite-anthophyllite) and tremolite-diopside skarns, all produced by the metamorphic processes of the submarine VMS system (Eilu et al. 2012). The ore deposits are hosted by carbonate skarns as well as felsic metavolcanic units, and some of them are bordering to the cordierite-anthophyllite rocks. Parkkinen (1975) describes the cordierite gneiss close to the contact of felsic volcanic rocks and tholeiitic basalts to be also a host rock for the ores (Fig. 14).

4.4 Metsämonttu ore mineralogy, structure, and alteration

The ore minerals found from the Metsämonttu deposit are pyrite, pyrrhotite, galena, sphalerite, and chalcopyrite (Latvalahti 1979). The ore bodies are small, and they appear as assemblages of vertical, almost parallel, and vertically homogenous sulphidic mineral zones south from an intermediate volcanic bed. Widths of the zones vary from few centimetres to few metres, and the horizontal measures of the orebody are at least 70 x 400 metres (Fig. 14; Parkkinen 1975). Sulphidizations continue down to 800 metres depth. They have been formed during a quieter period of volcanic activity after powerful volcanic activity when hydrothermal, metal-carrying fluids were circulating in the porous, tuffaceous bed (Latvalahti 1979).

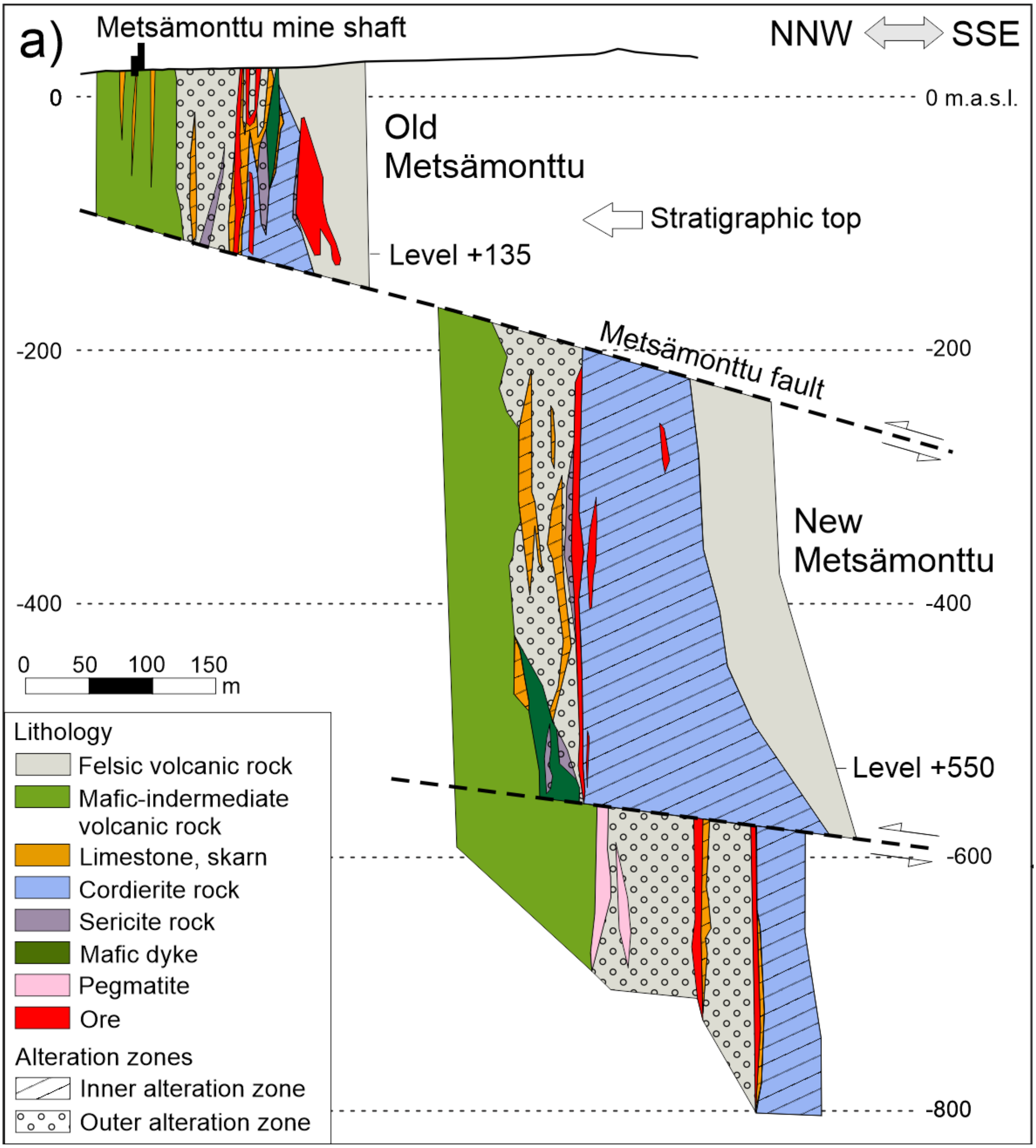

Figure 14. Section across the Metsämonttu ore deposit (Leväniemi & Hokka 2021, after Latvalahti 1979).

According to Latvalahti (1979), the ores appear as breccias, massive sulphide veins and sulphidic disseminations. The breccia ores are economically the most feasible ones since they are sub-massive, and they appear in tremolite-diopside-chlorite skarns, dolomitic limestones, and sometimes in quartz-rich lithologies. The ore minerals replace silicate minerals like pyroxenes and amphiboles in the wall rocks, fill fissures and cracks. The contacts between the wall rocks and ores are acute. Skarn- and dolomitic limestone -hosted breccia ores contain more Pb and Ag than other ore types while the cordierite mica gneiss and quartz rock -hosted breccias contain more Fe-sulphides and some sphalerite and occasional chalcopyrite. Sulphidic disseminations are connected to the breccia ores, and they also replace silicate minerals. Pyrrhotite and pyrite are found in cordierite-anthophyllite rocks, and only pyrite is found in sericitic and muscovitic gneisses. Mostly pyrrhotite- and pyrite-containing veins are common throughout the deposit, and they may extend from an inch to several metres.

Ore deposits of Metsämonttu can be also divided based on their chemical composition. Latvalahti (1979) distinguished three different orebodies: 1) Zn-Pb, usually hosted by skarns and dolomitic limestones. Main minerals occurring within this ore type would be pyrite, pyrrhotite, galena, and sphalerite, with accessory arsenopyrite, chalcopyrite, magnetite, boulangerite, molybdenite, and tetrahydrite. In addition, native Au and Ag would be connected to the occurrence of galena (Leväniemi & Hokka 2021). 2) Zn-Fe, found from the cordierite gneisses. Main minerals include sphalerite, pyrite and pyrrhotite with accessory galena, chalcopyrite, ilmenite, magnetite, and marcasite. 3) Cu lenses, hosted by cordierite gneisses. Main minerals include Cu-bearing chalcopyrite, pyrite, and pyrrhotite, with accessory sphalerite, galena, native Au, and Cu-containing cubanite. According to Mäkelä (1989), usually the wall rocks are diopside-tremolite skarns, muscovite gneisses, and quartz rocks.

Several deformation events have affected the ore bodies of Metsämonttu: there has been fault displacement events that have split the ore bodies to different zones (Parkkinen 1975; Latvalahti 1979), as represented in Figure 14. According to Mäkelä (1989), the displacement would be 270 metres to north to the uppermost fault of Metsämonttu and 80 metres to the fault that is located lower. The zones have been named the upper being Old Metsämonttu that was mined first, and the lower being New Metsämonttu.

The formation of the sulphidic zones might be related to a certain volcanosedimentary deposit, but the principal structural controls are schistosity and vertical lineation. Sulphidizations can be also divided to three different age groups. The oldest group would be pyrites containing Cu and Zn. Pb-containing ore generation is more complex and younger, and sometimes appears together with pyrites, sometimes apart from them. Fracture zones containing chalcopyrite as lenses, pockets or dispersed seem to represent the youngest generation (Parkkinen 1975). It is interpreted that due to later deformations and folding the sulphides were remobilized, and this has given the orebodies of the deposit their current characteristic elongated form (Latvalahti 1979).

According to Latvalahti (1979), the peak metamorphism reached the lower-pressure amphibolite facies with the pressure of 3 kb and the temperature of 650 ± 30 °C. Hydrothermal alteration and the following metamorphic processes are strongly present in the lithologies of Metsämonttu area. Hydrothermal alteration has partially destroyed the primary structures and textures of the volcanic rocks, and primary minerals have been replaced by the secondary ones (Eskola 1914; Mäkelä

1989). However, some of the primary structures have been preserved, such as pillow lavas and laminar and layered structures of the tuffites (Latvalahti 1979).

Formation of the mineralizations is also closely connected to the alteration processes. The structurally controlled ores are bound to an alteration zone, that is split to inner and outer zones, as described in Figure 14. The ores are mainly located between these two zones. The inner alteration zone is characterized by silicification and Mg-Fe-metasomatism, and is dominated by cordierite-anthophyllites, cordierite-biotite gneisses, dolomite-containing limestones, and tremolite-diopside-chlorite skarns. Sericitisation is strong in the outer zone, which is mostly consisting of metamorphosed felsic lithologies. Below the ore and related to it there is a cordierite-anthophyllitic alteration pipe of a funnel shape, that probably would have been formed inside or next to a discharge channel. On top of the ores and in some places under it there are often cordierite-containing sericite and muscovite gneisses and schists that are described to be blanket-like due to their conforming behavior. (Latvalahti 1979)

Alteration in the area occurs as a loss of Na and Ca as well as enrichment of K, Fe and Mg (Eilu et al. 2012). The principal alteration type in the exterior alteration area in Metsämonttu is sericitization (Leväniemi & Hokka 2021) that produces mainly muscovite. Due to sericitisation, feldspar becomes unstable, and this might cause the loss or gain of potassium, and loss of calcium and sodium. Quartz and albite might be formed as by-products, and if plagioclase is demolished, this might cause the formation of paragonite, as in Equations 13-15:

$$\mathrm{3NaAlSi_3O_8 + K^+ + 2H^+ \leftrightarrow KAl_3Si_3O_{10}(OH)_2 + 3Na^+ + 6SiO_2} \tag{13}$$

albite fluid muscovite fluid quartz

$$\mathrm{3KAlSi_3O_8 + 2H^+ \leftrightarrow KAl_3Si_3O_{10}(OH)_2 + 2K^+ + 6SiO_2} \tag{14}$$

orthoclase fluid muscovite fluid quartz

$$\mathrm{4(Na,K)AlSi_3O_8 + 2H^+ \leftrightarrow NaAlSi_3O_8 + KAl_3Si_3O_{10}(OH)_2 + 6SiO_2 + 2Na^+} \tag{15}$$

alkali feldspar fluid albite muscovite quartz fluid

According to Mathieu (2018), another typical alteration process of the VMS deposits present also in Metsämonttu is chloritisation, which causes gains of Fe and Mg and eventually creates chlorite (Equation 16). This alteration type is very dominant in the drill cores of Metsämonttu.

$$\mathrm{2KAl_3Si_3O_{10}(OH)_2 + 3H_4SiO_4 + 9Fe^{2+} + 6Mg^{2+} + 18H_2O = 3Mg_2Fe_3Al_2Si_3O_{10}(OH)_8 + 2K^+ + 28H^+}$$

muscovite fluid chlorite fluid (16)

According to Latvalahti (1979), in this area the Mg-Fe-metasomatism would be described with the gain of MgO, FeO, Al_2O_3, and TiO_2, and with the loss of SiO_2 and Na_2O. Silicification could be seen as the rise of SiO_2, and the depletion of all other elements. According to Ratsula (2016), the hydrothermal alteration in the Orijärvi area has reduced the amount of Ca, Na, and As in all the altered rocks while Mg and F have been enriched into them. Al, Fe and P contents on the contrary did not show significant differences between altered and non-altered rocks. Higher Mg contents are possibly due to precipitation of Mg transported by hydrothermal fluids while Na and Ca have probably been diluted from the protoliths to the fluids.

5 Materials

Four selected drill cores MM-190, MM-196, MM-198 and MM-241 from the area of Metsämonttu mine were chosen for more detailed pXRD and imaging spectroscopy analysis. The measurements have been done as a part of the process development project of GTK. Originally the project has been a subproject of a *Battery mineral potential survey* project of GTK that has begun in the year of 2019 with a special focus on analyzing the applicability of different handheld analyzers to data collection of brownfield targets. The material contains over 500 drill logs from Outokumpu Oy and dozens of archived drill cores. The geochemical data available from the area is limited to the main elements and trace elements of ore geological interest.

All the studied four drill cores have been drilled in 1959-1961 and their diameter is 22 mm. The drill cores were chosen since they contain relatively altered lithologies prominent for further investigations related to metamorphic phase transitions. The drill core MM-190 was logged by geologist Arno Varma and the rest of the three cores were logged by geologist A. Stenberg. The drill cores have been drilled for exploration purposes. (Outokumpu Oy 1959a-c; Outokumpu Oy 1961)

As presented in Figure 15, all the drill cores have been obtained from the unit, that has been classified as felsic tuffaceous sandstone. All four drill cores have been drilled 150-300 metres south of the Metsämonttu mine main building. The drill cores MM-196 and MM-198 locate very close to each other. In the surroundings there are some mafic and intermediate volcanic rocks, and in the main area of Metsämonttu mine there are garnet-cordierite-anthophyllite gneisses.

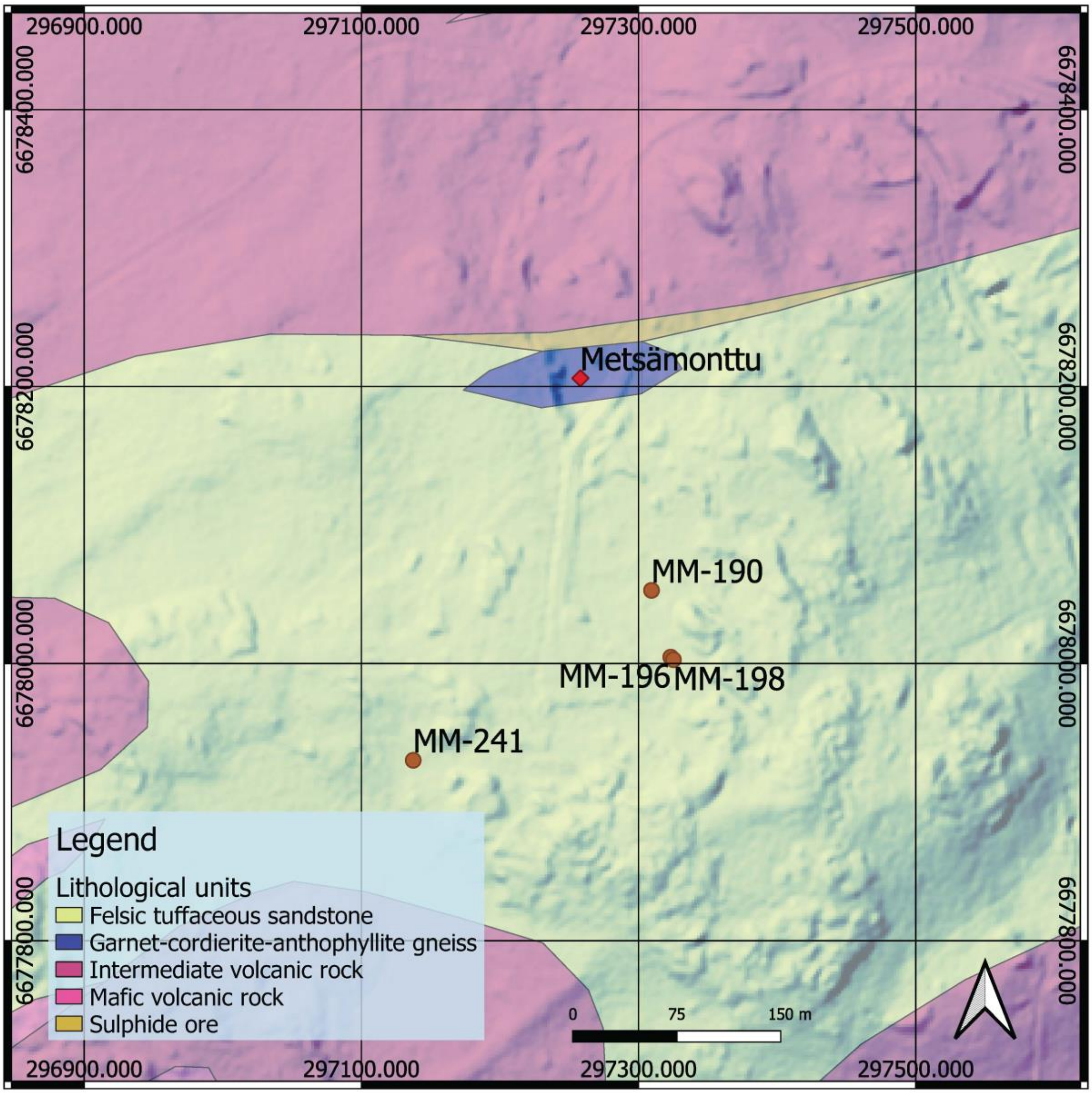

Figure 15. Map of the drill cores MM-190, MM-196, MM-198 and MM-241. The drill cores have been obtained south from Metsämonttu mine. (Bedrock of Finland scale free, modified data © Geological Survey of Finland [2021]; CC BY 4.0, Hillshade 2 m, contains modified data from the National Land Survey of Finland Topographic Database 10/2021)

The lithologies represented in Figure 16 are based on the original logging data by Outokumpu Oy (1959a-c, 1961). GTK has gathered the archived drill core logging data in 2019, digitized the data, and during this process combined some lithological units that have been logged. It is worth to notice that according to recent, yet unpublished observations the sequences originally named “quartz porphyry” are not of felsic origin as interpreted by Latvalahti (1979) but most likely consist of mafic units. It is important to notice that the lithologies here are described in a simplified manner, and some of the smaller lithological units are merged to larger ones.

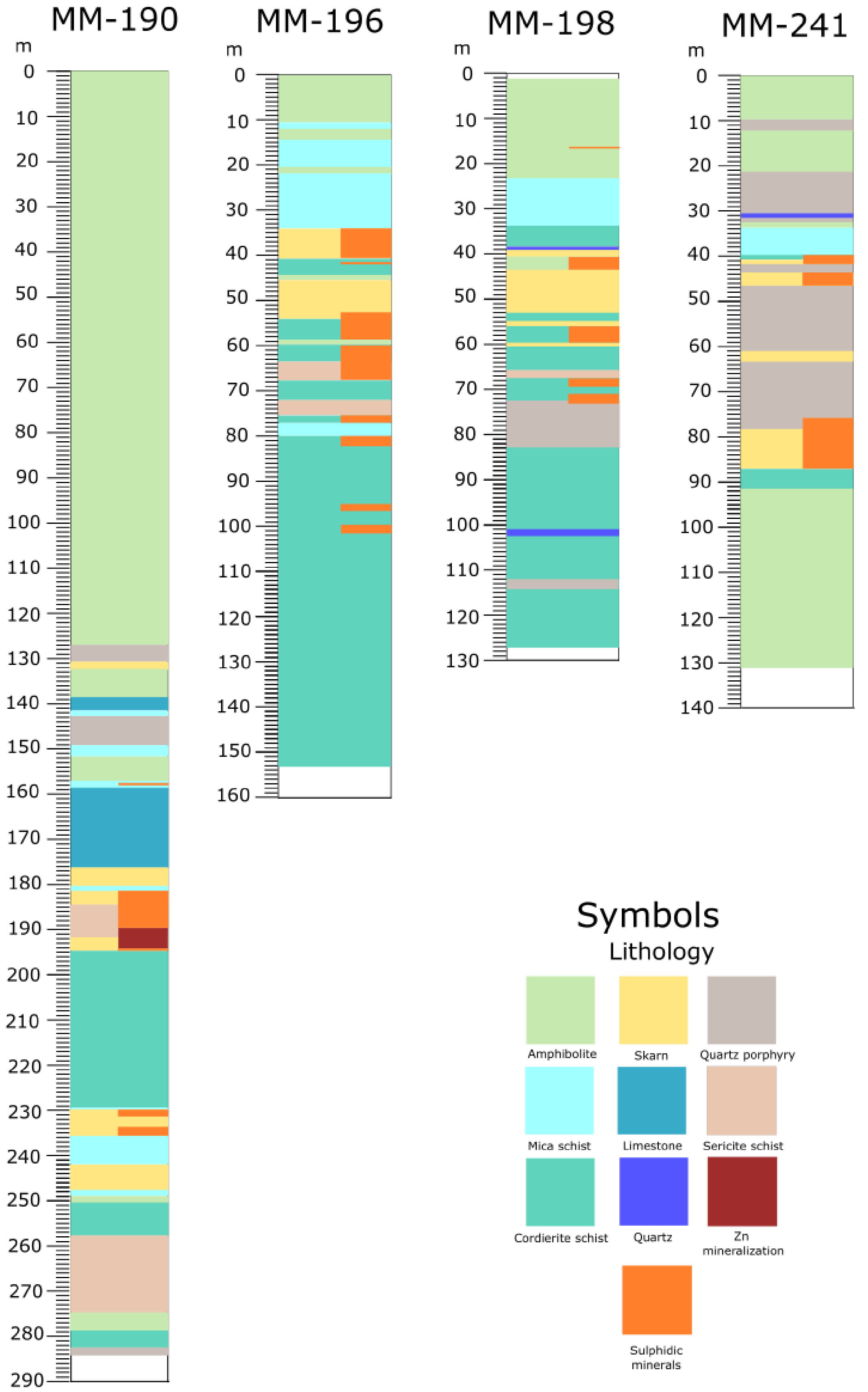

Figure 16. Lithologies of the studied drill cores. Drawing modified from the original drill core loggings by Outokumpu Oy (1959a-c, 1961).

5.1 Drill core MM-190

MM-190 is a 284.4 m long drill core (6678052.8544 N, 297309.3243 E, -255.62 Z EUREF-FIN) drilled from the +320 level. It was logged in 1959 by geologist Arno Varma (Outokumpu Oy 1959a). Dips of the core were 64.35° at 0 m, 56° at 95 m, 46.5° at 195 m and 30.5° at 284.4 m depth. The azimuth of the drill core is 141.3225°.

As stated in the original drilling report (Outokumpu Oy 1959a), the drill core begins with a long amphibolite sequence (Fig. 17) that is cut by schistose quartz porphyry unit in the depth of 127.10 m. Lithologies change to more diverse direction in this point: under the quartz porphyry appears a layer of skarn with limestone with porous cracks filled with quartz (130.70-132.50 m). Under it the amphibolite alternates with skarned limestone, mica schist and quartz porphyry. In the depth of 157.6 m there is a 6 cm wide quartz vein with some arsenopyrite in the mica schist, following by the alternation of limestone, skarn, and mica schist. Sulphidic minerals (mainly pyrite) appear sparsely in the depth of 181.66 m in skarn that is cut with a sequence of sericite schist (186.5-189.8 m) with a small amount of pyrite.

Figure 17. A piece of the drill core MM-190 taken from the depth of 105 metres. The amphibolite sequence dominates the beginning of the drill core. Photo: Geological Survey of Finland.

Zinc ore appears in a cordierite gneiss sequence in the depth of 189.80 m continuing together with disseminated iron sulphides for the first couple of metres. Then the host rock changes to skarn with the ore body continuing down to 194.03 m. After this point there are couple of points where sulphidic minerals re-appear. Cordierite schist sequence in the depth of 212.70-221.80 m hosts some pyrite. Tremolite skarn in the depth of 229.90-231.50 m hosts some pyrite and in the depth of 233.90-235.72 m some galena. The skarn alternates with the mica schist until they are cut with a short amphibolite sequence (249-250.65 m).

In the end of the drill core there are couple of longer sequences of cordierite schist that surround the sericite schist unit (257.80-274.40 m) and the amphibolite unit (274.40-282.60 m) in between. The drill core ends to the quartz porphyry unit in the depth of 284.40 m.

5.2 Drill core MM-196

MM-196 is a 153.6 m long drill core (6678004.653 N, 297323.1769 E, -257.33 Z EUREF-FIN) drilled from the +320 level. It was logged in 1959 by geologist A. Stenberg (Outokumpu Oy 1959b). Dips of the core were 49.33° at 0 m, 49° at 10 m, 49.2° at 25 m, 31° at 75 m and 14° at 153.6 m depth. The azimuth of the drill core is 162.0425°.

Sulphidic ore minerals (galena, pyrrhotite and pyrite) occur first as weak and dispersed in skarn at 34 m depth. Then the host rock changes to brecciated cordierite gneiss carrying some galena and pyrite at 40.60 m depth. In the depth of 44.30 m the cordierite gneiss is cut by a short sequence of amphibolite (44.30-45.20 m) and then a quartz vein (45.20-45.30 m), and then the host rock changes again to skarn with small amounts of pyrite and pyrrhotite in the depth of 45.30 m. There is a rapid alternation of cordierite schist and skarn between 52.80-58.75 m depth, cordierite schist carrying arsenopyrite and skarn having small amounts of pyrrhotite disseminated.

In the depth of 54 m begins a sequence of cordierite gneiss with plethora of sulphidic minerals including arsenopyrite (in the depth of 54-54.30 m) and in the depth of 56.90-58.76 m pyrite, sphalerite, pyrrhotite and chalcopyrite (without arsenopyrite). The cordierite gneiss is cut sharp with an amphibolite vein (58.75-59.45 m). Sulphidic mineralizations continue under the amphibolite vein in another cordierite gneiss sequence within the depth interval of 59.70-63.85 m. Cordierite gneiss is cut by a sericite schist sequence (Fig. 18) in the depth of 63.85 m which alternates with the cordierite schist.

Figure 18. A piece of the drill core MM-196 taken from the depth of 73 metres. Sericite quartz sequence shows schistosity. Photo: Geological Survey of Finland.

Sulphidic ore minerals (pyrrhotite, sphalerite and chalcopyrite) re-appear again between the depths of 75.25-77.82 m in the cordierite gneiss sequence and continuing in the depth of 77.10 m to the mica schist sequence. This sequence is short and does not seem to carry ore minerals. Under it a longer sequence of the cordierite gneiss continues from the depth of 80 m until the end of the drill core. There are several minor sulphidic mineralizations in this sequence: the first one is in the depth of 80.10-82.20 m with chalcopyrite, pyrrhotite, sphalerite and galena. The next one is in the depth of 95.20-96.83 m with pyrite, sphalerite, and galena. Seemingly the last one is located in the depth of 99.70-101.45 m carrying pyrite, galena and pyrrhotite.

5.3 Drill core MM-198

MM-198 is a 127.4 m long drill core (6678002.7762 N, 297325.1406 E, -254.56 Z EUREF-FIN) drilled from the +320 level. It was logged in 1959 by geologist A. Stenberg (Outokumpu Oy 1959c). Dips of the core were -52.12° at 0 m, -45.5° at 30 m, -34.5° at 63 m and -23° at 127.4 m depth. The azimuth of the drill core is 163.7992°.

The drill core begins with a long sequence of amphibolite. There is a small amount of arsenopyrite in the depth of 17.30 m. There is some disseminated pyrite in skarn between 39.10-40.70 m and first sulphidic grains (pyrite and pyrrhotite) are observed in the depth of 40.70-43.50 m in the amphibolite sequence (Fig. 19) and later a small amount appears in the cordierite gneiss in the depth of 55.40-59.45 m.

Figure 19. A piece of the drill core MM-198 taken from the depth of 43 metres. Dark sulphidic mineral grains are visible in the amphibolite (hornblende gneiss). Photo: Geological Survey of Finland.

In the depth of 66.97-69.16 m sphalerite accompanies pyrite and pyrrhotite in the cordierite gneiss. The cordierite schist sequence is cut by thin layers of skarn (69.85-70.40 m), quartz porphyry (70.40-70.99 m) and amphibolite (70.99-71.36 m), until another thin cordierite schist sequence begins with pyrite, pyrrhotite, sphalerite and chalcopyrite. The cordierite schist is cut in the depth of 72.06 m by a quartz porphyry sequence carrying a small amount of galena and pyrite in 71.36-72.90 m depth. The rest of the drill core is dominated by the cordierite schist with slight alternation of quartz porphyry sequences and a thick quartz vein in the depth of 101.35-102.55 m.

5.4 Drill core MM-241

MM-241 is a 131.4 m long drill core (6677930.3753 N, 297137.3862 E, -441.82 Z EUREF-FIN) drilled from the +510 level. It was logged in 1961 by geologist A. Stenberg (Outokumpu Oy 1961). Dips of the core were 50.26° at 0 m, 38° at 50 m, 38° at 90 m and 36° at 131.4 m depth. The azimuth of the drill core is probably 163.0325°: however, in the drilling report it is unclear due to unclear writing.

This drill core differs slightly of the three other drill cores. It is located 150-200 m southwest of the other localities presented in this study. The drill core is dominated by amphibolitic sequences in the beginning and the end of the core, and it has relatively large proportion of quartz porphyry. It barely has any cordierite gneiss present. First sulphidic minerals, pyrite and pyrrhotite, appear dispersed in the depth of 39.90-40.75 m in the cordierite gneiss sequence.

Under the cordierite gneiss the skarn begins to alternate with the quartz porphyry. In the depth of 44.76-46.40 m there appears some galena hosted by the skarn. The sequence changes to a longer quartz porphyry unit in the depth of 46.50 m. In the depth of 67.75-73.30 m there is a fractured zone, hosting a 5 cm wide clay layer in the depth of 71.40 m.

Quartz porphyry begins to have some skarn mixed into it in the depth of 75.90 m and some galena and sphalerite in places. Within 77.15-78.15 m there is galena, pyrite, and sphalerite. The unit shifts to a long tremolite skarn sequence in the depth of 78.15 m, with several different sulphidic mineral concentrations containing galena, sphalerite, and chalcopyrite (Fig. 20).

Figure 20. A piece of the drill core MM-241 taken from the depth of 85 metres. There are sphalerite, galena and chalcopyrite hosted by tremolite skarn. Photo: Geological Survey of Finland.

The rest of the unit has chloritized and ends to a cordierite schist unit with pinitization and without sulphidic minerals. The end part of the drill core >91.5 m is amphibolite (Fig. 21) with some epidote and grossular garnets in places without sulphidic minerals.

Figure 21. A piece of the drill core MM-241 taken from the depth of 125 metres from the amphibolite sequence. Photo: Geological Survey of Finland.

6 Followed methodology

Selected drill cores were measured with a pXRD, a handheld spectrophotometer with the SWIR and the VNIR wavelengths, a pXRF analyzer, and petrophysical methods. Sample preparation included cleaning the drill core and for the pXRD, samples were pulverized by Dremel and sieved under 150 microns before adding to the sample holder. Measurements were done every 1 meter from the drill cores with all other methods except the pXRD where the interval was 10 metres due to longer sample treatment procedure. Leväniemi et al. (2020) describes the measurements and their calibrations in detail and here they are described only briefly. The aim of the measurements was to define geochemical, petrophysical and mineralogical features of the drill cores.

The measurements were done in 2019-2020 by GTK. The SWIR and VNIR spectroscopy were done by GeoPool Oy of all the cores with ASD Terraspec 4 Spectrophotometer. The measurements with another spectrometer, ASD Terraspec© Halo (further mentioned as Halo), were done by GTK. (Leväniemi et al. 2020)

6.1 The portable X-ray diffraction measurements

6.1.1 The portable X-ray diffraction measurement procedure

The pXRD measurements were done with Olympus Portable Onsite XRD Terra-542 (Fig. 22) device that uses 30 kV high-voltage power supply for the generation of X-rays. The device has a 1024x256 pixel 2D charge-coupled device sensor with a Peltier cooler. The X-ray radiation source was a cobalt tube.

Figure 22. The front panel of Olympus Portable Onsite X-Ray Diffraction (XRD) Terra-542 device. Photo: Jenniina Siira.

There is also a vibrating, piezo-harmonic sample holder whose purpose is to randomize the grain orientations during the measurement. During the measurement, the device stays still but the sample is rotated by the vibrating sample holder. Otherwise, the device does not contain moving parts such as the laboratory devices. The functional temperature range of the device is -10° - 35° C (Olympus 2020). The energy resolution was 0.25° 2θ FWHM and the angular resolution was 5-55° 2θ. The required sample amount was 15 mg (Leväniemi et al. 2020).

10 m systematical sampling interval was longer compared to other methods since the pXRD sample preparation process is more time-consuming. The purpose of systematical measurements was to test what additional value does non-directional mineralogical data collecting bring.

The samples were drilled from the rock surface using a diamond drill from 1 x 2 cm area. The sample powder was gathered on a piece of paper and then moved on a sieve. The samples were sieved so that their grain size would be <150 μm. Dry sample powder was placed in between the Mylar films of the measurement chamber. The amount of sample powder was evaluated visually: the ideal exact sample amount would be 15 mg but there should be also enough powder to fill half of the measurement chamber so the material could rotate well enough in the chamber. The excess powder was blown away before placing the measurement chamber to the device.

Samples bearing sulphide minerals were measured with 150 hits and other samples with 85 hits. These samples demanded longer measurement time due to fluorescence, especially in the presence of galena. This amount of time was sufficient to detect 3-5 mineral phases. After the measurement the sample chamber films were cleaned with ethanol and compressed air.

Quality assurance was made using an in house quartz standard that was measured at least daily and whenever there was a doubt that there is some uncertainty in the measurements. At least every 10th measurement was therefore the quartz standard. The quartz standard was also used to check the peak locations and intensities. In addition, there were other mineral samples by Chemplex used. (Leväniemi 2020)

6.1.2 Processing the portable X-ray diffraction data with XPowder software

The pXRD measurements were interpreted using XPowder software version 2010.01.35. In the software the identification of the minerals is done using a database including mineral peaks and intensities. The used database was American Mineralogist Crystal Structure Database (AMCSD) which includes over 14000 crystallographic and mineralogic diffraction patterns.

Lower d-spacing was set to 1.65 and higher d-spacing to 70.0. Background subtraction was applied to all spectra. To some of the spectra with plenty of background noise the elimination of noise using Fourier transform was tested in order to eliminate higher frequencies in the Fourier transform with a cutoff value. The function then calculated the inverse transform producing a filtered diffractogram. However, since it was noticed that elimination of background noise influenced semiquantitative proportions of mineral phases, the proportions were calculated from the diffractograms with no background noise elimination.

Diffraction patterns were identified by using Advanced search function where 2 theta gap was set to 0.30 and matching criteria to “2 reflections”. Next, the software identifies the first crystal or phase that it thinks to be the closest match provided by using the “Automatic” check up in the “Least squares fitting” sub-menu.

At least 3-5 main phases were identified either automatically or manually from each measured sample in order to calculate the d-spacing. Those patterns were selected which represented the best possible fit of the diffraction pattern as well as intensity. In addition, some other interesting and relevant phases were included to the phase interpretation when necessary. When enough phases were selected, the unchecked (and unwanted) phases were eliminated by clicking “Unchecks” button.

A semi-quantitative analysis was run automatically after identifying the phases by clicking “Quantitative” function. XPowder calculates the proportion of each phase by non-linear least square approach for the whole diffractogram. It uses all the reflections caused by each component, and by taking all this data into account, it tries to minimize the effects caused by preference orientation (Martin 2008)

R-value, also known as a residual index, is defined in Equation 17:

$$\mathrm{R} = \frac{\Sigma\,|\mathrm{F_{obs}} - \mathrm{F_{calc}}|}{\Sigma|\mathrm{F_{obs}}|}, \tag{17}$$

where F = structure factor. Its sum covers all the reflections of measured X-rays and their calculated correlatives, and it can be used to evaluate the quality of analysis (Massa & Gould 2004; Will 2006) In order to derive good R-values, those diffraction patterns with best fitting intensities were chosen. XPowder includes the R-value to the calculation.

XPowder calculates the Reference Intensity Ratios (RIR) of phase references of all patterns (Chung 1974) and μ/ρ (mass attenuation coefficient) values from the chemical and density data stored in the database. XPowder tries to evaluate the proportion of amorphous material in the sample by calculation Global Amorphous Stuff % (GAS) with the following Equation 18:

$$GAS = \left\{\left[\frac{(\Sigma\, I_i)}{N}\right]^2 + \sigma^2\right\}^{\frac{1}{2}}, \tag{18}$$

where I = diffracted intensity in the point I, N = number of measured points in the X-ray pattern and σ = standard deviation of I_i. (Martin 2008)

In the end of the interpretation, refractory cards were created including all known phases to them to evaluate future diffraction patterns having the same kind of mineralogical features. The resulting data were weighed according to w = 1/√Counts with “Weight data” function. The d-space values of the patterns were also refined with “Refine 2-theta” function. Finally, statistics were included to the resulting diffractogram as well as to the Log file.

All the diffractograms of each drill core were also gathered and stacked in order to observe alterations within each drill core. In this point the diffractograms were smoothed using Fourier transform to create a coherent visual appearance. Smoothing with other methods, such as the least squares method was also tested, but the results were not that great for this dataset.

6.2 The near-infrared spectroscopy

6.2.1 The near-infrared spectroscopy measurement procedure

The SWIR and the VNIR spectroscopy were done with a handheld ASD Terraspec 4 Portable NIR Spectrophotometer (serial number FSFR 2131; further mentioned as Terraspec) by Malvern Panalytical. The spectral range is 350-2500 nm, resolution is 3 nm @ 700 nm and 6 nm @1400/2100 nm, wavelength reproducibility is 0.1 nm and wavelength accuracy 0.5 nm. The device has 2151 channels. The VNIR detector is a 512-element silicon array, and the SWIR 1 & 2 detectors are Graded Index InGaAs photodiodes that are TE cooled. The signal-to-noise ratio of VNIR is 9000:1 @ 700 nm, SWIR 1 is 9000:1 @ 1400 nm, and SWIR 2: 4000:1 @ 4100 nm. The operating temperature is 0-40 °C. The device used RS3™ spectral acquisition software which is compatible with The Spectral Geologist.

The measurement time was 7.0 seconds with 1 meter interval. All drill cores were also measured with the Halo analyzer by GTK. Both devices identify minerals within 350-2500 nm wavelength. The minerals to be identified with this method should contain hydroxyl group(s) (-OH) and C-O bond(s). There were no results of all the measurements since the device measures only one wavelength region. The calibration was done with a blanco sample accompanied the device each time when the device was restarted. Additional calibrations were not used when the data were produced.

The samples were washed and dried before the measurement to remove excess dust. The measurements were taken directly from the sample surface when the sample was completely dry. Measurement points were drawn on the sample with a pencil and the measurement was done from the according depth to the mark so that the area marked with the pencil would not fall to the measurement area. Reference and collateral samples were measured with the Halo analyzer in the same way as the actual drill cores.

6.2.2 Processing the near-infrared spectroscopy data with The Spectral Geologist software

The NIR spectra measured by Terraspec were used for the interpretation. The obtained spectra were afterwards treated and interpreted with TSG software by CSIRO. TSG uses its own reference library in mineral interpretation. The SWIR library contains approximately 493 samples that reflect 60 pure substances (mainly minerals, but also some synthetic materials and water), and the VNIR library contains 17 classes with 90 spectra. TSG uses The Spectral Assistant™ (TSA) algorithm, which is a linear unmixing algorithm using a rapid subset selection procedure in the spectral analysis of the samples (Berman et al. 2011).

The reference libraries of TSG were used in mineral interpretation and automatic interpretation was run for all four drill cores. Up to three mineral phases were identified by using the automatic interpretation of each measurement point. The measurement window of the spectrometer was larger than the diameter of the samples, and it can be seen in all the results in the beginning of the spectra in the wavelength area of visible light. This was considered in interpretation and since all the measurements were made in a similar manner, the results are comparable among each other.

However, the libraries of TSG are not extensive, and the automatic mineral identification does not always work in an ideal manner. Some of the spectra might not get interpreted by the software itself, possibly because the shape of the spectrum or the absorption feature locations or their depths do not follow precisely the reference library. This might be due to alteration (McCanta & Dyar 2020) or weathering (Ehara Suryantini et al. 2005) of the mineral. Therefore, all the spectral data had to be interpreted from each drill core. The preliminary interpretation was done by GeoPool Oy in 2019, and the interpretations were still double-checked during the writing process of this thesis, especially in cases when the spectra had been interpreted as “Aspectral”. The measured spectra were compared to the spectra of the reference libraries to detect whether the spectra would correlate to each other or not.

The device stores the spectra in *ASD file format which is brought to TSG either one spectrum by one or all spectra as a set. In the SWIR analysis, the minimum output values were set to begin from 1300 nm to exclude the VNIR data and include only the SWIR data to the analysis. Maximum output value was not determined.

Overall picture of the drill cores and their mineralogy was examined using the “Summary” section. “Log” section was used to analyze numerical data of the dataset. This section also included automatically interpreted mineral phases. “Norm. HullQuot” column represents the location of the peaks and data quality while “Error sTSAS” column would describe data quality even more precisely with a numerical value. When error value would be <1000 the data would be still reliable enough for interpretation. Log section allows to create new columns for new numerical data obtained from the original dataset by using a function “New Scalar”.

“Spectrum” section was used to analyze a singular spectrum compared to the spectra of the reference library or another mineral. Information from this section was used to evaluate and interpret the data quality. The summary section was used to obtain and visualize general information of the cores: their mineral, elemental and mineral group distribution.

After bringing in the dataset including all the spectra of all four drill cores to the TSG, the data quality was evaluated using the information provided by the “Error sTSAS” column in the “Log” section. In this dataset peak locations and depths for peaks of 2200 nm (AlOH), 2255 nm (FeOH) and 2335 nm (MgOH) were included to the analysis. Depth of the peak of the water (1910 nm) was also calculated and included to the data. Table 4 summarizes the used central wavelength and radius values:

Table 4. Central wavelength and radius values used in the processing of the SWIR data.

Peak	Central wavelength, nm	Radius
AlOH	2204	24
MgOH	2335	35
FeOH	2255	15
Water	1910	30

6.3 The portable X-Ray Fluorescence

The pXRF measurements were measured with Vanta™ Handheld X-Ray Fluorescence Analyzer by Olympus (ID: SN804043). Measurements began in August 2019. Calibration mode used was Geochem. Two beams were used with measurement time of 30 seconds + 30 seconds. Each sample was measured once. The greatest voltage was 40 ekV. Geochem calibration is able to analyze the contents of the following elements: Mg-S, K-Ca, Ti-Zn, As-Se, Rb-Mo, Ag, Cd, Sn, Sb, Hg and Pb-Bi. The measurements were done from the round, thin surfaces of the drill core.

Each sample to be measured was cleaned with water few months prior to the measurements and just before the measurement dust was removed from their surface by wiping them with a dry cloth. Boxes containing the drill cores were brought inside the hall several hours before the measurement to avoid surface moisture to weaken the elemental concentration. The analyzer was switched on at least 45 minutes before the actual measurements began. It was connected to a laptop (Panasonic CF-19) and operated using Vanta Desktop software (version number 3.16.66). The samples were placed on a protective plate under a radiation safety cupola. There were wooden controllers taped on the protective plate of the device to be able to target the samples always in the middle of the measurement window in a similar manner.

In the beginning of the measuring week a CalCheck function was run for the device and each day was started by measuring the Blank standard provided by the device manufacturer. Two factory-made standards, Blank and NIST 2711A, were used as in house calibrations in following deviations in the function of the analyzer. They were measured in turn after every ten samples. NIST 2711A standard was replaced with a new one in the middle of the measurement period due to a breakage of the original standard. (Leväniemi et al. 2020)

6.4 Petrophysical methods

6.4.1 Density

The density was measured by air-water scaling with Precisa BJ6100D scale. Weighting range was up to 6100 g, readability 0.1 g, response time 2 s, reproducibility 0.1 g and linearity 0.2 g. Standards were measured after every 20 samples, in the beginning and in the end of each drill hole. The measurements were made with 1 meter interval first by placing the sample as dry on a scale and then placing it to a scaling basket inside the water. The underwater scaled reading was recorded, and then the next sample was placed to the scaling basket. In general, it would be better to conduct the density measurements when the sample would be saturated of water in example after soaking the sample in water for one day. However, in this study it was chosen to do the measurements in above-mentioned manner due to large sample amount and timetable limitations.

The measurement procedure is described in full by Leväniemi et al. (2020). Data calibration report and more precise results are presented by Leväniemi (2019).

6.4.2 Magnetic susceptibility and conductivity

Both magnetic susceptibility and conductivity were measured with KT-20 S/C handheld magnetic susceptibility and conductivity meter with 10 kHz frequency and 2.54 cm diameter correction. The samples were oriented vertically to the sensor of the meter. The measurement was repeated three times from the same elevation around the sample with 120° angle. The measurement procedure is described in full by Leväniemi et al. (2020). The data calibration report is presented by Leväniemi (2019).

7 Results

An overlook was casted on the geochemical data measured with the pXRF to make some geochemical classification of the samples. Regardless appearances and origin of the rocks all studied analyses were used for the diagrams to present the general geochemical affinity. The Nb/Y vs. Zr/Ti classification diagram (Fig. 23) by Pearce (1996, modified after Winchester & Floyd 1977) focuses on the immobile element ratios in classification which is suitable for this dataset since the lithologies are very altered. According to the diagram (Fig. 23), majority of the studied volcanic rocks can be classified as basalts, andesites or basaltic andesites.

Chemical variations in the hydrothermally altered rocks are due to input or take off of the mobile elements in open system conditions (Franklin et al. 2005). These variations in the system can be described analysing changes in individual elemental contents by using ratios between different elements, Pearce element ratios (Pearce 1968), conventional indicator indices such as the Chlorite-Carbonate-Pyrite Index (CCPI, Large 2001a) or the Alteration Index (AI, Ishikawa et al. 1976). These can be used as ore vectors (Large et al. 2001b).

Certain indices, such as the magnesium number (Moore & Ault 1965), the CCPI, the AI, and the muscovite saturation index (Kishida & Kerrich 1987) were tested to observe the alteration within the drill cores and its possible connection to the appearance of the ore minerals. The geochemical data gathered from Metsämonttu are unfortunately insufficient since the data have been measured with pXRF analyser and therefore lacks the contents of sodium oxide (Na_2O). Many of the typical classification diagrams could not be applied and the emphasis had to be put on analysis of distribution of heavier, immobile elements.

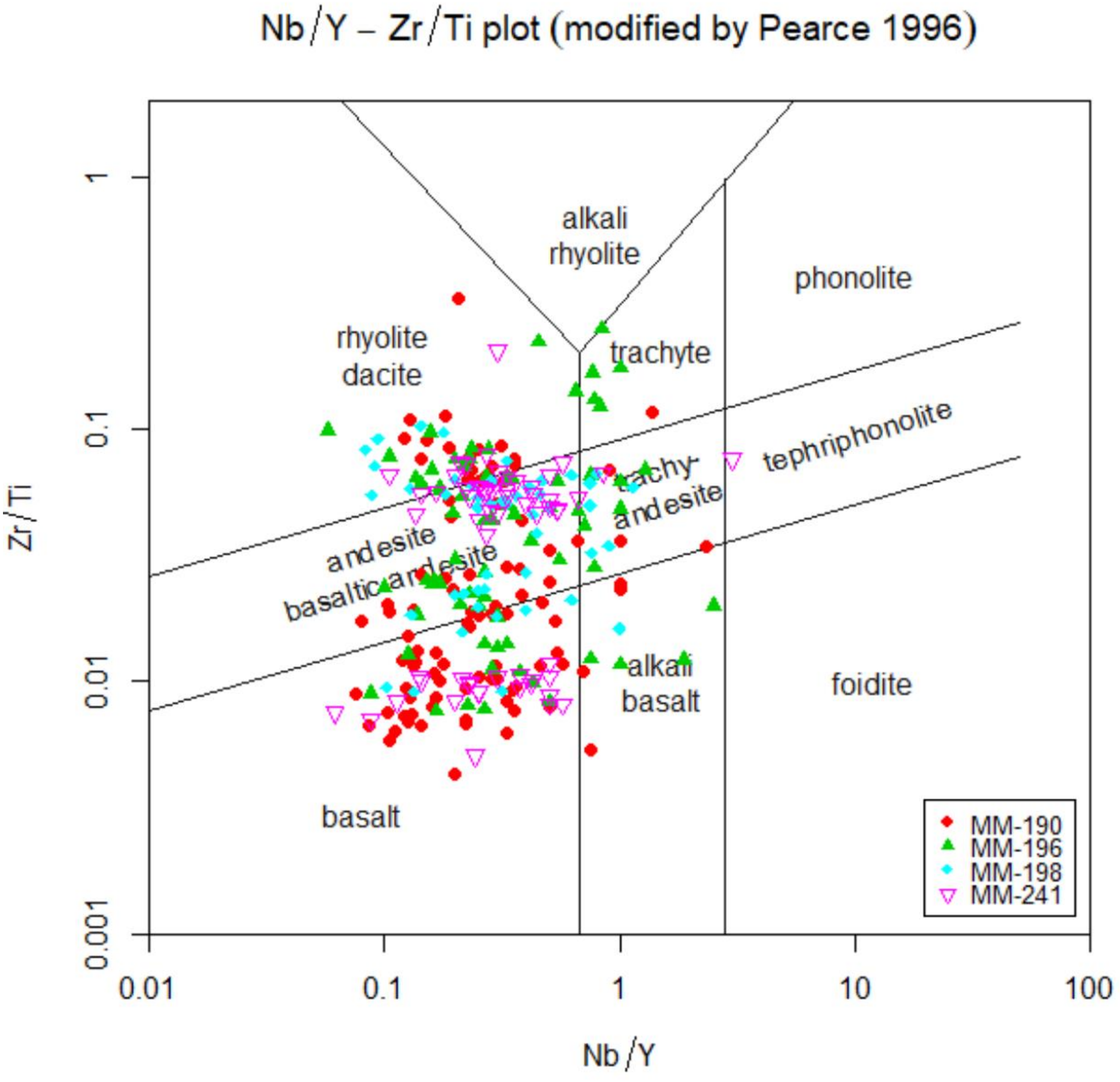

Figure 23. Zr/TiO2 v. Nb/Y diagram (Pearce 1996, after Winchester & Floyd 1977) of the volcanic rocks of the drill cores MM-190, MM-196, MM-198 and MM-241.

The magnesium number (Mg#) in Equation 20 describes the fractionation of the magmas:

$$Mg\# = \frac{\mathrm{Mg}}{Mg+Fe} \times 100 \qquad (20)$$

In this calculation it is assumed that total iron would be Fe^{2+} (Moore & Ault 1965). In the drill core MM-190 there is a sharp increase in the magnesium number in the depth of 158-176 m where the lithological unit shifts to limestone (Figs. 16 and 24). When the lithological unit alternates to skarn and the sulphidic ore minerals (pyrite, sphalerite, chalcopyrite, and pyrrhotite) appear, there are some rapid changes up and down in the magnesium number. Similar kind of rapid changes can be seen later in the drill core in the depth of 230-235 m where sulphidic minerals reappear.

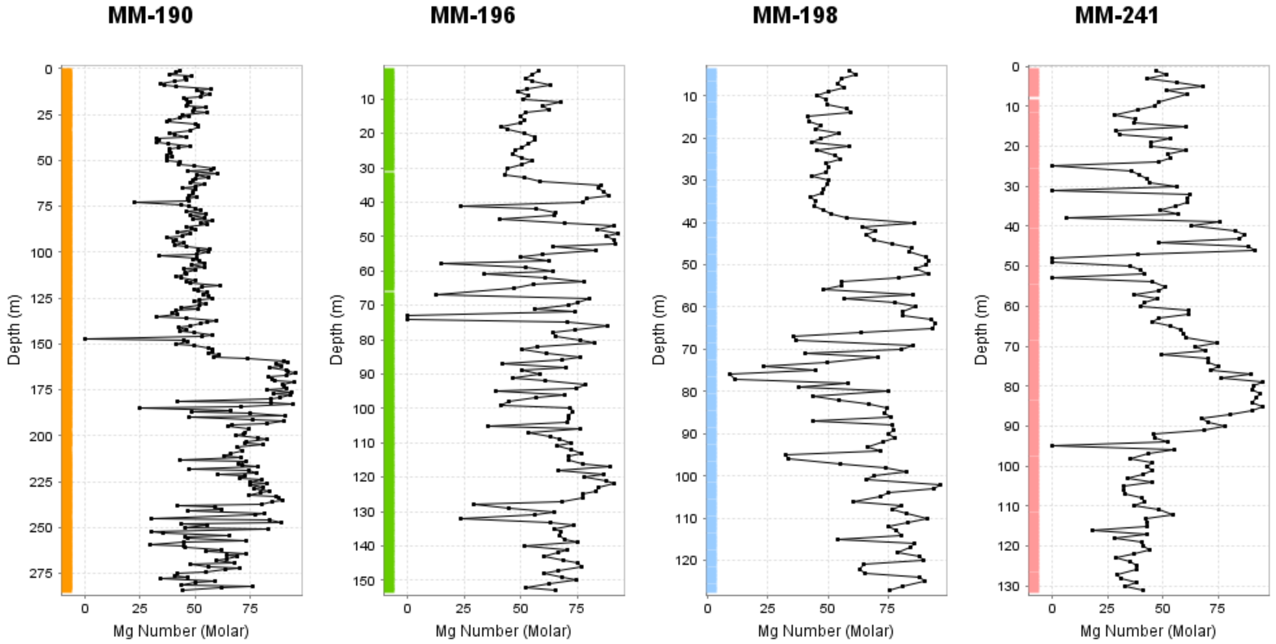

Figure 24. The magnesium number of all the four drill cores plotted against the depth of the drill core.

In the drill core MM-241 there is a gradual increasing trend in the magnesium number when the lithological unit changes to the quartz porphyry unit that alternates with the skarn (Fig. 16). When the quartz porphyry shifts to skarn, the magnesium number increases up to almost 100. In the drill core MM-196 the sulphidic minerals appear as dispersed, and when they appear, the magnesium number seems to decrease. The same trend can be seen in the drill core MM-198 where the magnesium number falls when sulphidic minerals appear (Fig. 16). These trends might mean that the occurrence of the sulphidic minerals would be connected to the fractionation of basaltic magmas. However, there are also complex hydrothermal processes behind their occurrence that have caused the alteration of the host rocks.

The Alteration Box Plot (Fig. 25) is a binary diagram based on the CCPI (Equation 21), and the AI (Equation 22), and applies well to the VMS systems (Large 2001a).

$$\mathrm{CCPI} = 100 \times \frac{\mathrm{FeO+MgO}}{\mathrm{FeO+MgO+Na_2O+CaO}} \tag{21}$$

$$\mathrm{AI} = 100 \times \frac{\mathrm{K_2O+MgO}}{\mathrm{K_2O+MgO+Na_2O+CaO}} \tag{22}$$

Both indices are meant for characterising certain types of alteration. In example, AI describes well sericitisation and chloritisation (Ishikawa et al. 1976) and evaluating the degree of hydrothermal alteration (Gemmell & Large 1992), but also Ca-metasomatism may affect to this index. It is important to notice that when counting CCPI and AI from the basis of mean values obtained from recently formed volcanic rocks, this would refer to shifts related to magmatic fractionation. The alteration indices are also controlled by the precursors, and this might cause challenges to their interpretation (Mathieu 2018).

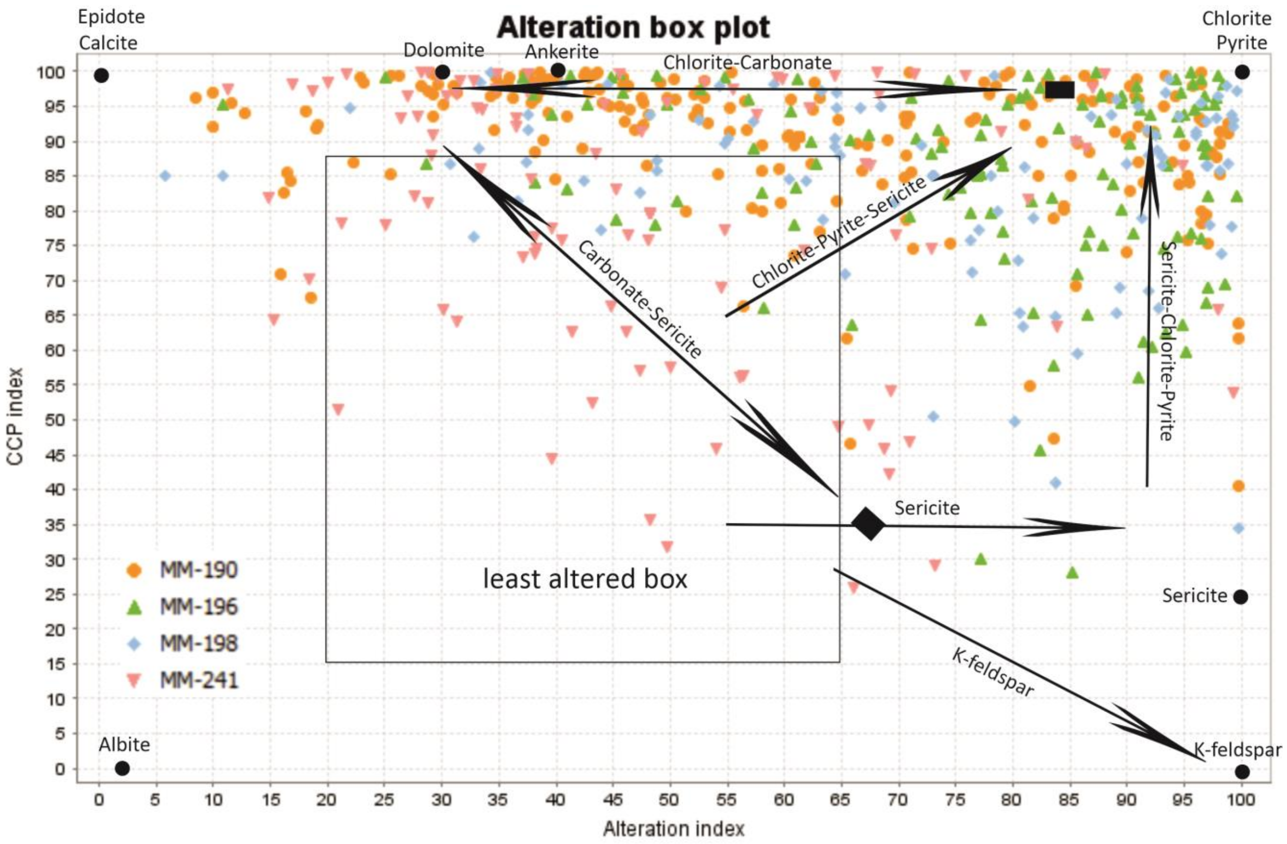

Figure 25. A modified Alteration Box Plot (after Large 2001a) of all the drill cores. The Alteration Box Plot is based on the Chlorite-Carbonate-Pyrite Index (100 x (FeO + MgO)/(FeO + MgO + Na_2O + CaO)) and the Alteration Index (100 x (K_2O + MgO)/(K_2O + MgO + Na_2O + CaO)). Na_2O values are missing from the dataset due to the data collection with portable X-ray fluorescence method.

Since Na_2O values are missing, the Alteration Box Plot here is represented as a modified version without potassium values. Overall, there is a trend towards the chlorite-pyrite corner of the plot caused by intense chloritisation with a significant emphasis on the chlorite-carbonate line as well especially in the case of the drill core MM-190. This most likely refers to the alteration processes occurred in the skarns and carbonate rocks in the material. On the contrary, many of the data points of the drill core MM-241 fall to the least altered box (Fig. 25).

Together with CCPI and AI two other indices, Chlorite index (CI) and Hashiguchi index were plotted against the depth of the drill core. The CI (Saeki & Date 1980) in Equation 23 is an index meant to quantify chloritisation:

$$\mathrm{CI} = \frac{\mathrm{MgO+Fe_2O_3}}{\mathrm{MgO+Fe_2O_3+2\times CaO+2\times Na_2O}} \tag{23}$$

The CI here is a modified one since it is counted without Na_2O values. It describes the gain of Fe and Mg as chlorite, and the deprivation of CaO and Na_2O when feldspars get destructed.

The Hashiguchi index (Hashiguchi et al. 1983) is another alteration index defined in Equation 24:

$$\text{Hashiguchi index} = \frac{\mathrm{Fe_2O_3}}{\mathrm{Fe_2O_3 + MgO}} \tag{24}$$

This index describes the addition of Fe as Fe_2O_3, and in this dataset it is a powerful tool since it allows to observe the alteration within the drill cores without using Na_2O values.

The muscovite saturation index (molar 3K/Al) is a saturation index that can be used for observing the intensity of alteration (Kishida & Kerrich 1987). As depicted in Figure 26, in the drill core MM-190 the muscovite saturation index does not seem to follow the zinc mineralisation (Fig. 16). The muscovite saturation index rises in the depth of ~120-125 m, 145 m, and 250 m. In the drill core MM-196 there are rises in the depth of ~70 m and around 100 m. The highest values of this index are found in the drill core MM-198 in the depth of 30 m, ~58 m and ~68 m. Within the drill core MM-241 there are no significant rises but rather a constant zig-zag pattern down to ~95 m.

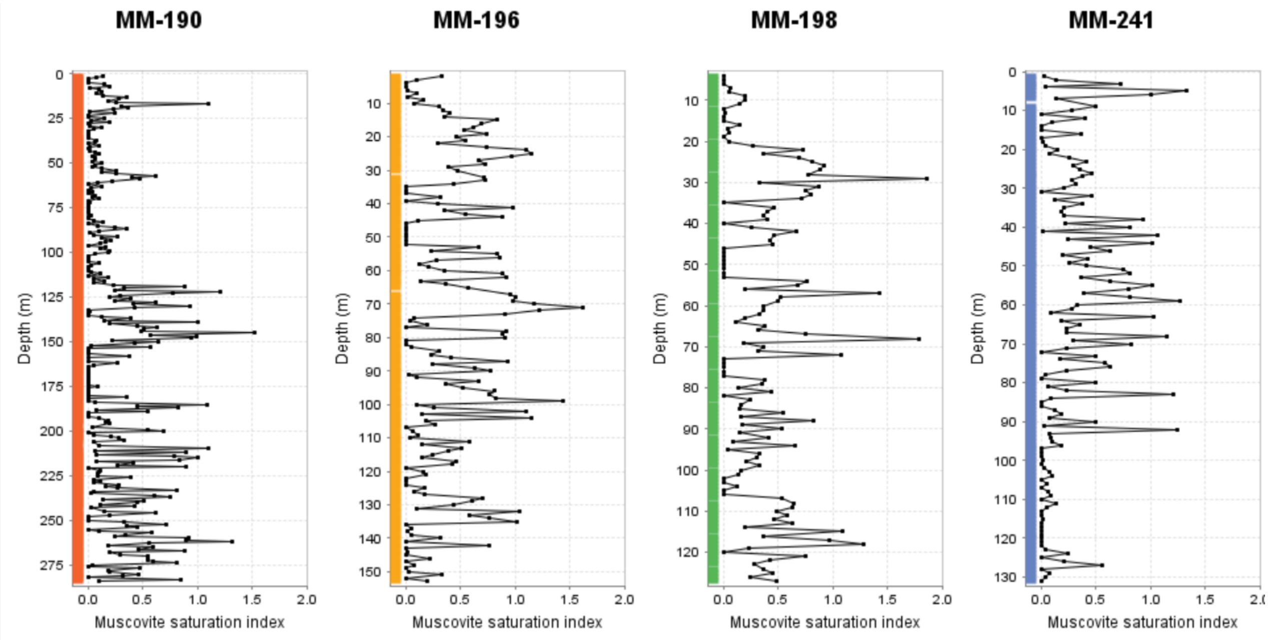

Figure 26. The muscovite saturation indices (molar 3K/Al, after Kishida & Kerrich 1987) of the drill cores MM-190, MM-196, MM-198, and MM-241 plotted against the depth of the drill core.

Ratios based on heavier elements such as Rb/Sr ratio could be used for approximation of the behaviour of the Al (McNulty et al. 2020). It has been reported that Rb/Sr ratios would be <0.1 for minimally altered rocks, 0.1-0.5 for weakly altered rocks, 0.5-1.0 for moderately altered rocks, 1.0-2.0 for strongly altered rocks and >2.0 for intensely altered rocks (McNulty et al. 2020; Gisbert et al. 2021).

Considering the petrophysical data, density should increase in the presence of metallic or mafic ore minerals (Airo & Säävuori 2013) while conductivity should be pretty much proportional to the sulphur content (Koskela et al. 2019). The magnetic anomalies are connected to the presence of ferrimagnetic minerals (Airo & Säävuori 2013), like magnetite (Fe_3O_4) and pyrrhotite ($Fe_{(1-x)}S$, where $x \leq 0.13$) (Dekkers 1989). According to Leväniemi & Hokka (2021), the distributions of the magnetic susceptibility and the density are multimodal. Based to the variation of the density and the magnetic susceptibility values these can be grouped to nine clusters that can be linked further to the lithogeochemical equivalents. In general, the ore minerals correspond well to the density and the conductivity anomalies while there is more irregular variability in the magnetic susceptibility.

Distribution of the mineral phases of all four drill cores measured using the SWIR spectroscopy shows a strong emphasis on different chlorite group phases (Fig. 27). There is a significant proportion of identified muscovite as well. This points out, that chlorite alteration is in an important and well observable role in these drill cores while muscovite alteration is not as strongly present as the chlorite alteration.

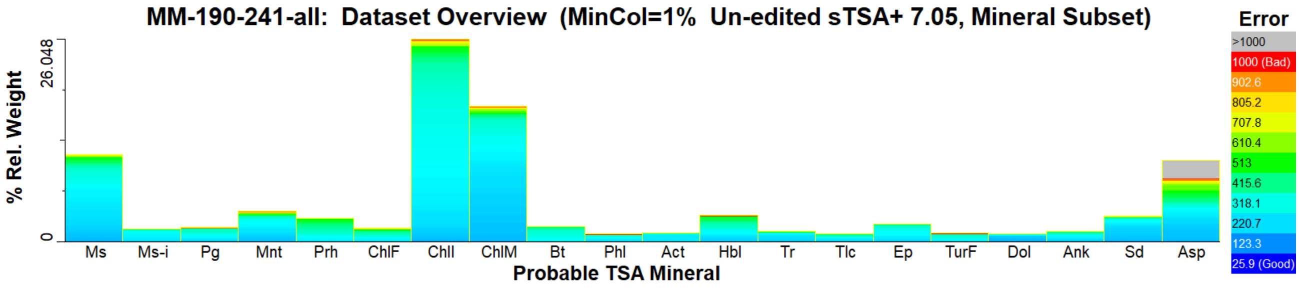

Figure 27. Distribution of mineral phases present in all drill cores detected by the SWIR spectroscopy and automatically identified with The Spectral Geologist software.

Sericite crystallinity is the depth value of AlOH (2200d) divided by the depth value of water (1910d). It can be used to evaluate the crystallinity of mica. The water content of the minerals can be also defined from the SWIR data by observing the absorption feature of water around 1900 nm (Clark 1999).

7.1 Results of drill core MM-190

A short overlook on the petrophysical and geochemical data of the drill core MM-190 in Figure 28 shows rapid and sharp increases in CaO contents that are tightly connected to the skarn and limestone units. The long amphibolitic sequence (0-127.10 m) in the beginning of the drill core is in fact cleaved with narrow skarn zones, and therefore this can be seen as sharp increases in CaO contents within the sequence. There is also a considerable TiO_2, P_2O_5 and As content anomalies in the depth of 40-50 m within the amphibolite unit, a peak in conductivity, and a small increase in S content, magnetic susceptibility and density. There are also singular peaks of Cr and Ni contents observed in the diagrams in the depth of 25 m.

In this drill core there are certain visible trends towards the mineralisation that appears within 189.80-194.03 m (Outokumpu Oy 1959a). The appearance of Cu-, Pb-, and Zn-bearing minerals corresponds well with the rise of density and conductivity in 185-190 m (Fig. 28). There is more irregular variability in the magnetic susceptibility in this drill core.

MM-190

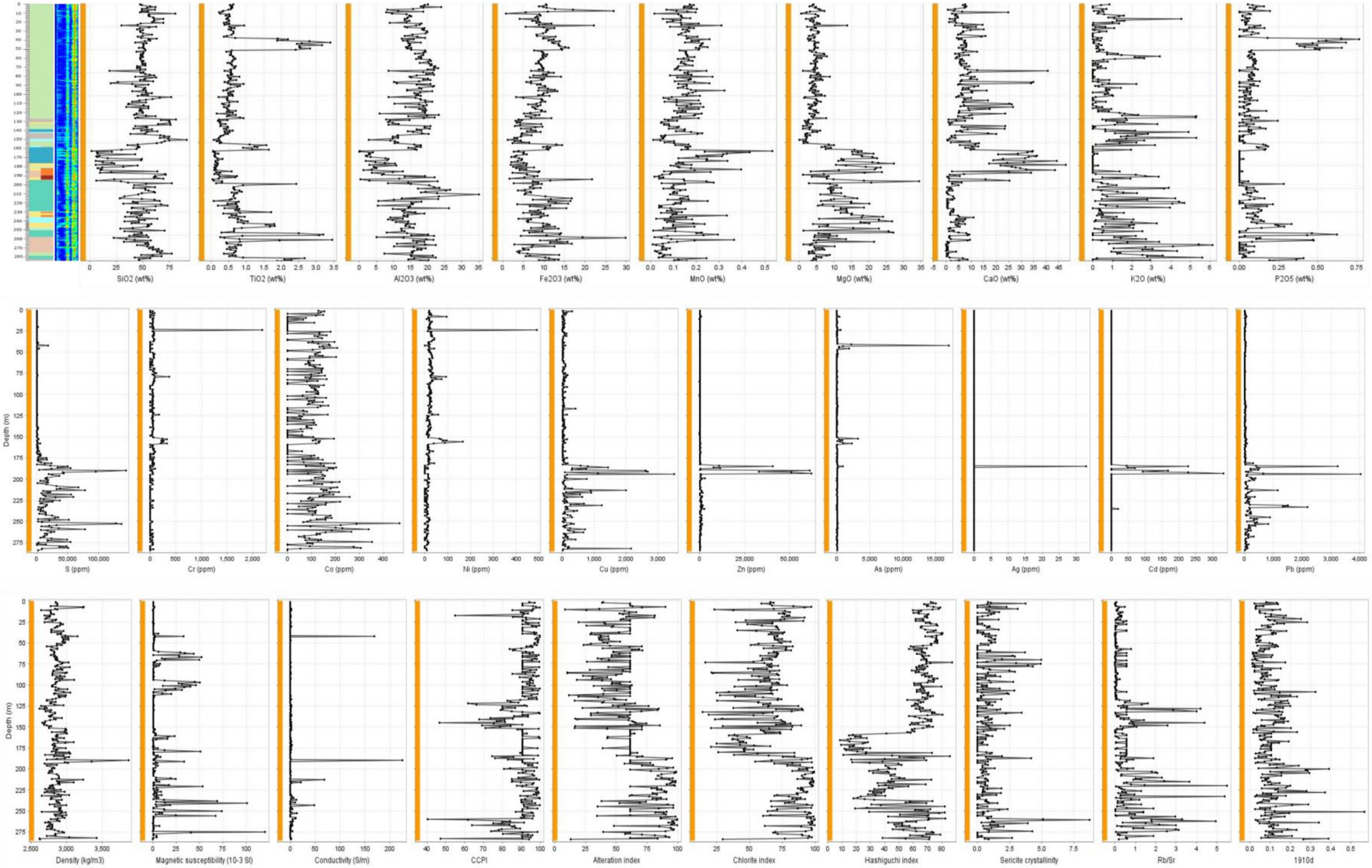

Figure 28. The geochemical, petrophysical, and alteration data of the drill core MM-190. On the upper left corner there is the logged lithology of the drill core. Explanations of the lithology as in Figure 16.

The CI forms pretty much similar a pattern than the AI (Fig. 28). Before the mineralisation there is a significant collapse, and when the ore minerals appear, there is a clear rising trend. The Hashiguchi index produces even more negative anomaly just before the mineralisation. When the ore minerals appear, a similar kind of rise appear than in the AI and the CI contents.

The Rb/Sr ratio does not form a distinctive pattern towards the mineralisation (Fig. 28), but it indeed shows that within this drill core the lithologies are very altered (>2.0) in several areas. The most altered lithologies are located between 125-130 m, 145-150 m, 215-235 m, and around 260 m (Figs. 16 and 28). A steep increase can be observed in the sericite crystallinity in 260 m, and in the water absorption peak in 250 m at the same time with an increase of S, Fe_2O_3, TiO_2 contents, and in the magnetic susceptibility.

The summary of the SWIR data (Fig. 29) shows that there is a great emphasis on chlorite group minerals within this drill core. Some muscovite and hornblende are also observed, and smaller amounts of biotite, montmorillonite, epidote, prehnite, and siderite. A considerable amount (approximately 1/6) of the data points that were identified as aspectral were of bad quality (>1000).

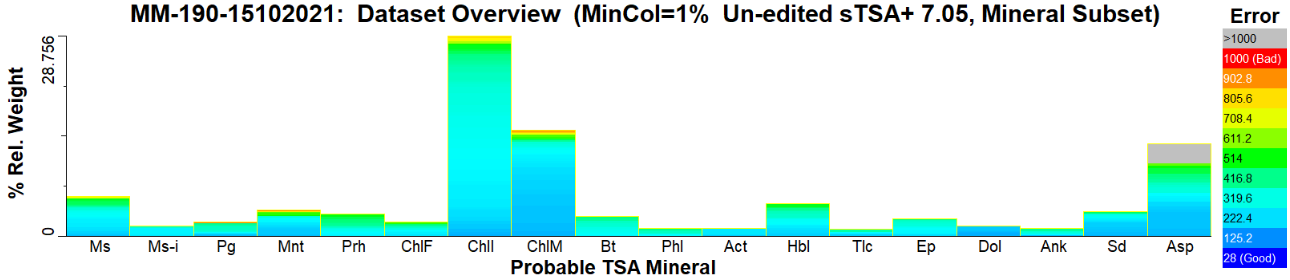

Figure 29. The summary of the mineral phases in the drill core MM-190 detected by short-wave infrared (SWIR) spectroscopy and automatically identified by The Spectral Geologist.

The mineralogical data measured with both the SWIR spectroscopy and the pXRD was visualised and compared to each other (Fig. 30). The SWIR wavelength was chosen since it covers most of the rock-forming minerals that are identifiable within these low wavelengths. The data were visualised using those data points that had measurement data recorded with both methods so the comparison would be possible.

Considering the mineralogical variation within the whole drill core (Fig. 31) using the whole SWIR data, the proportion of Mg-chlorite is growing around the Zn-ore. In a group level the strong presence of chlorite within the whole drill core can be observed very clearly, and the pXRD data support this observation even though they do not show that much of variation within the drill core. An elemental distribution shows an increase in Ca and Mg contents just before the ore appears, which would refer to the dolomitic limestone unit. Beginning approximately from the altered lithologies after the Zn-ore, the presence of montmorillonite increases towards the end of the drill core and could refer to argillic alteration.

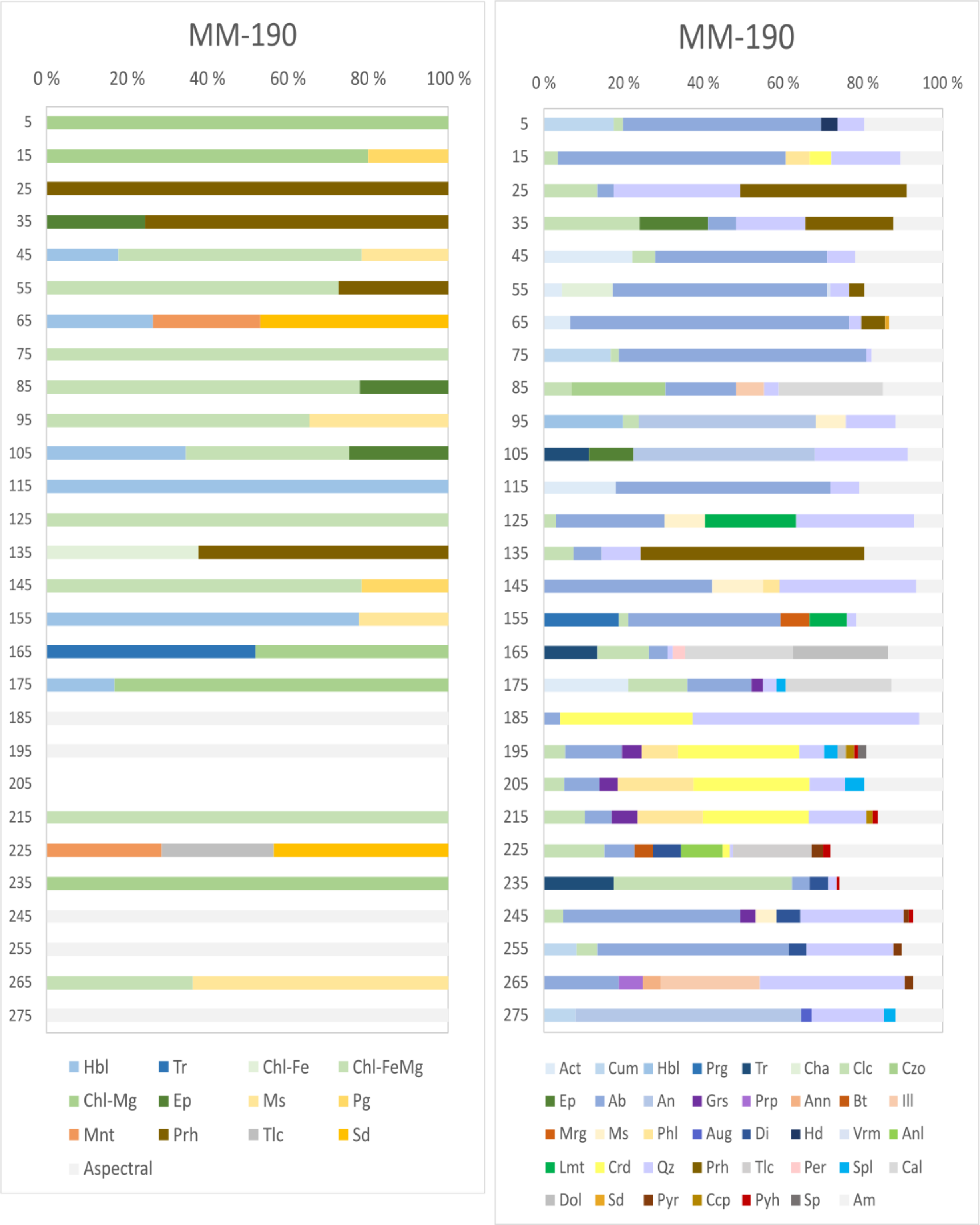

Figure 30. The mineralogical data of the drill core MM-190 by mineral. Left: The short-wave infrared (SWIR) data. Right: The portable XRD (pXRD) data. Abbreviations: Act = actinolite, Cum = cummingtonite, Hbl = hornblende, Tr = tremolite, Cha = chamosite, Chl-Fe = Fe-chlorite, Chl-FeMg = Fe-Mg-chlorite, Chl-Mg = Mg-chlorite, Clc = clinochlore, Czo = clinozoisite, Ep = epidote, Ab = albite, An = anorthite, Grs = grossular, Prp = pyrope, Ann = annite, Bt = biotite, Ill = illite, Mrg = margarite, Ms = muscovite, Phl = phlogopite, Pg = paragonite, Aug = augite, Di = diopside, Hd = hedenbergite, Vrm = vermiculite, Anl = analcime, Lmt = laumontite, Crd = cordierite, Qz = quartz, Prh = prehnite, Tlc = talc, Per = periclase, Spl = spinel, Cal = calcite, Dol = dolomite, Sd = siderite, Pyr = pyrite, Ccp = chalcopyrite, Pyh = pyrrhotite, Sp = sphalerite, Am = amorphous

In the beginning of the drill core in 5 m there is only Mg-chlorite visible in the SWIR data, even though the pXRD was able to also identify cummingtonite, hedenbergite, albite, and quartz from the sample (Fig. 30). Within 15-35 m no amphiboles are detected with neither method. Instead, in 15 m there is paragonite as a mica in the SWIR data, but in the pXRD data it is shown as phlogopite.

In 25 m there is prehnite visible in both data: in the SWIR data it is the only mineral phase detected while in the pXRD there is also quartz, albite, and clinochlore. Prehnite together with epidote is identified by both methods in 35 m, but the pXRD shows again that there is more mineralogical variation: clinochlore, quartz and albite.

Amphiboles reappear again in 45 m (Fig. 30). TSG identifies the amphibole phase as hornblende, while the pXRD recognizes the amphibole as actinolite. TSG software identifies muscovite from the data, but it does not fit into the pXRD interpretation. In 55 m TSG software does not identify any amphiboles: instead, it finds prehnite and a Fe-Mg-containing chlorite group phase. In the pXRD data these both are visible, but at this point instead of clinochlore, chamosite is identified alongside with actinolite, albite, vermiculite, and quartz. These observations find support from the old drill core loggings that describe the “amphibolitic” unit in between 49.80-101.80 m being fragile, mangled, and having plenty of thin skarn bands (Outokumpu Oy 1959a; Fig. 16).

Both the pXRD and the SWIR data (Fig. 30) show a small amount of prehnite, amphiboles, and siderite in 65 m. However, the presence of siderite is not supported with the Fe_2O_3 or CaO content measurements, but there is a rise in the magnetic susceptibility data. Since the amount of siderite is so small and as a mineral it should be paramagnetic, it probably is not producing the anomaly in the magnetic susceptibility data.

The pXRD data (Fig. 30) in the depth of 165 m reveals that the limestone unit within the depth of 158.40-176.20 m first consists of a combination of calcite and dolomite with some tremolite, clinochlore, albite, quartz, and periclase as an alteration product of dolomite. This can be seen as an increase not only in CaO content but also in MgO content in Figure 28 and was thus expected. Afterwards, in 175 m the composition shifts to calcitic one with no more dolomite including albite, clinochlore, quartz, spinel, and grossular. The old logging does not describe this variation (Outokumpu Oy 1959a).

In the depths of 185 m, 195 m, 245 m, 255 m, and 275 m TSG identified the spectra to be aspectral (Fig. 30), and therefore could not identify the minerals. It is a bit unfortunate since the mineralisation would be located in between 189.80-194.03 m, and it is surrounded by sulphidic minerals. In 185 m it is understandable that TSG identifies the sample to be aspectral since the sample contains cordierite, quartz, and albite, and those minerals are not visible within the SWIR wavelength. However, in the case of the rest of the data points read as “aspectral” it is also peculiar that TSG has not identified any minerals of them. At this point the old log describes the lithological unit to be skarn variation (Outokumpu Oy 1959a; Fig. 16) which also contrasts with the pXRD data (Fig. 30).

According to the pXRD data (Fig. 30), in 195 m phlogopite, clinochlore, and dolomite would be major minerals that should be possible to identify with the SWIR spectroscopy. In addition, in this depth there is cordierite, albite, quartz, spinel, grossular garnet as well as ore minerals, chalcopyrite, pyrrhotite, and sphalerite. In 245 m there would be some clinochlore and muscovite amongst the possible minerals identifiable with the SWIR spectroscopy, and some quartz, albite, grossular, diopside, pyrite, and pyrrhotite. In 255 m cummingtonite and clinochlore should have been possible to identify from the SWIR data; albite, quartz, diopside, and pyrite were identified by the pXRD.

In the SWIR data (Fig. 30) there are also some data missing in 204-205 m since the spectrometer gave completely empty measurements from these data points. The pXRD data (Fig. 30) show that in 205 m there is cordierite, phlogopite, albite, clinochlore, grossular garnet, quartz, and spinel. TSG should have been able to show at least the chlorite-group and mica counterparts of these minerals. There are also empty data points in the depth of 117 m and 216 m, but these points were not measured with the pXRD.

In general, the pXRD data (Fig. 30) show very little variation in the chlorite group mineral composition. In most of the samples it is identified as clinochlore ($Mg_5Al(AlSi_3O_{10})(OH)_8$), but in the depth of 55 m it is identified as chamosite ($(Fe^{2+},Mg,Al,Fe^{3+})_6(Si,Al)_4O_{10}(OH,O)_8$). Considering the amphiboles, TSG has recognized mostly hornblende from the SWIR data except tremolite in 165 m. On the contrary, the pXRD has identified more different amphiboles: mostly actinolite and cummingtonite, but there are observations of tremolite and singular observations of pargasite and hornblende.

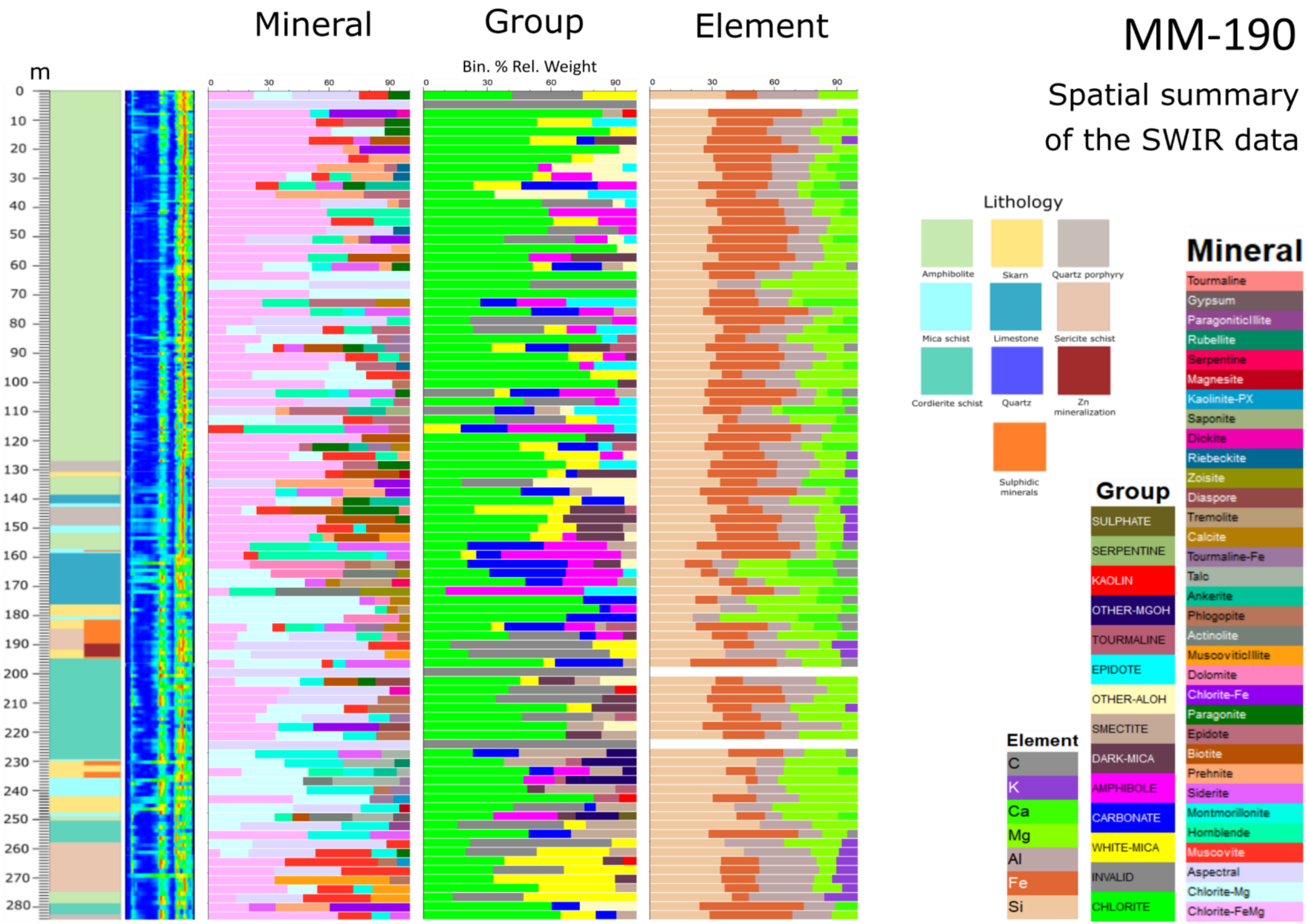

Figure 31. The visualized lithological and short-wave infrared (SWIR) data of the drill core MM-190.

Considering the anomalies in the magnetic susceptibility data within the drill core, it can be seen that some of them would be connected to the Fe-oxide phases identified with the VNIR spectroscopy (Fig. 32). A large part of the VNIR data were identified as aspectral and there were also many empty measurements. However, within this drill core there are some observations of “galvanised iron” and “Zn-Al alloy” identified by TSG, and some of these observations show correlation with the magnetic susceptibility data (Fig. 32). These automatic mineral identifications do not reflect the actual compositions of these phases, since galvanised iron is iron coated with zinc. However, these data points might refer to some iron oxides that the spectrometer was able to observe, but TSG was just not able to name these phases correctly.

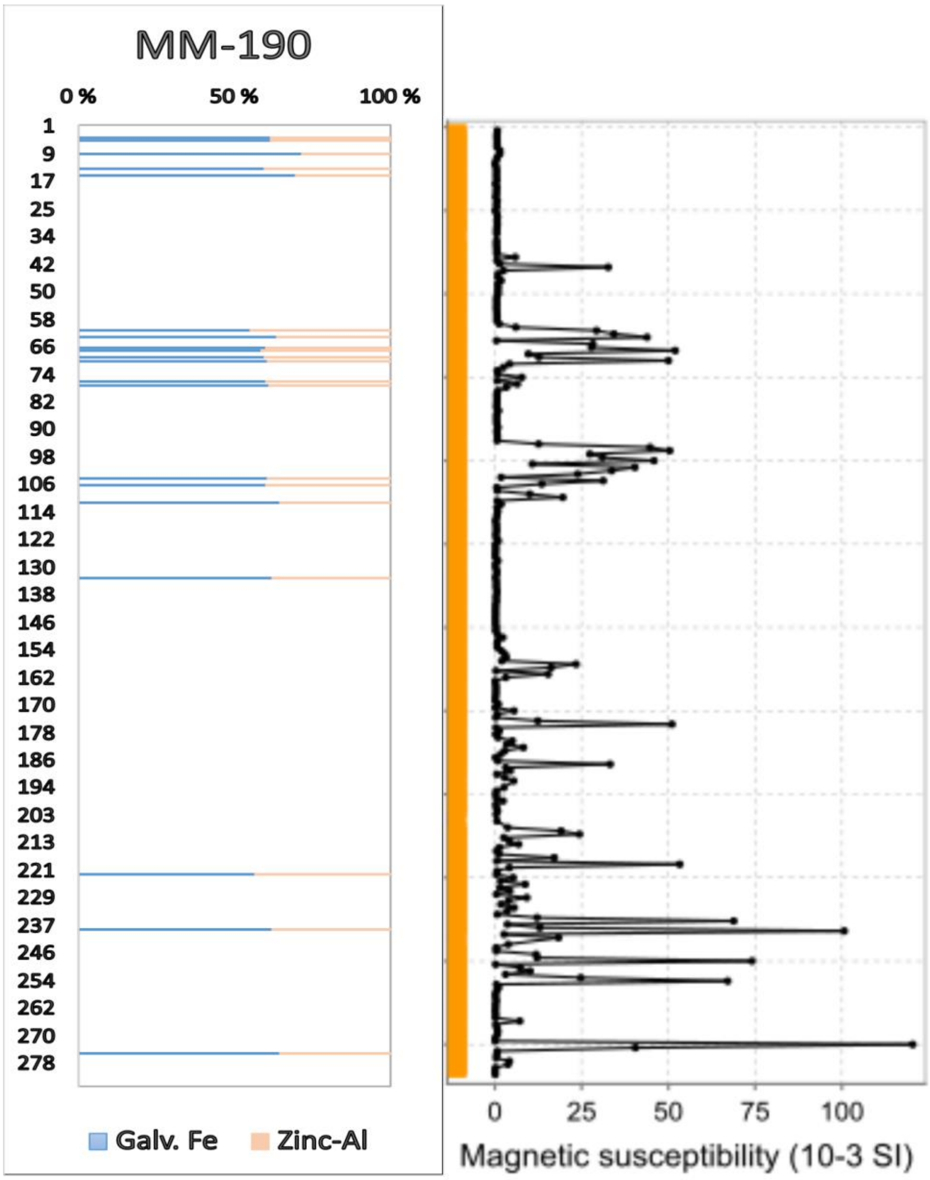

Figure 32. Visible, near-infrared (VNIR) and magnetic susceptibility data plotted against the depth of the drill core MM-190.

The wavelength positions of AlOH (2200 nm), FeOH (2255 nm) and MgOH (2335 nm) were plotted against the depth of the drill core, and this data were compared to the logged lithologies of the drill core (Fig. 33). This approach reveals that when the amphibolitic sequence begins to shift to the limestone in the depth of ~150 m, there is a shift in the FeOH and MgOH peak locations. In the Chlorite index and the Hashiguchi index (Fig. 28) this can be seen as a sharp, declining trend. When the lithological unit changes to the sericite schist in the depth of ~258 m, this can be seen as a shift in the MgOH peak locations to the 2330-2350 nm interval.

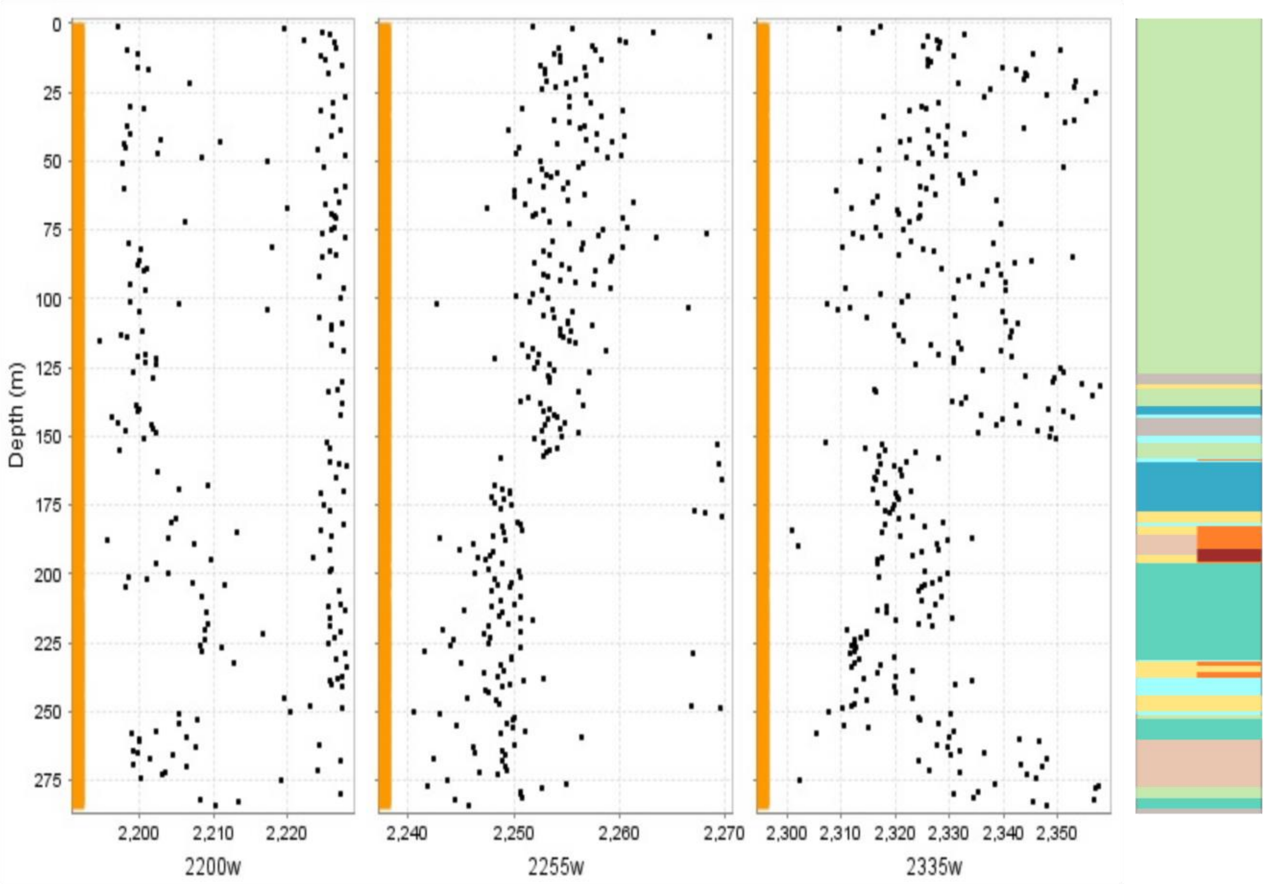

Figure 33. The wavelength positions of AlOH (2200 nm), FeOH (2255 nm) and MgOH (2335 nm) absorption features plotted against the depth of the drill core MM-190. The horizontal scale is in nanometres. On the right-hand side there is the logged lithology of the drill core. Explanations of the lithology as in Figure 31.

The wavelength positions of AlOH absorption features (Fig. 33) seem to be splitted into three different compositional groups within the whole drill core. The paragonitic, sodic (high octahedral Al) group with AlOH wavelength <2200 nm would mostly appear within 0-155 m in the amphibolitic unit and 255-275 m in the sericite mica unit. The potassic, muscovitic group (2200-2210 nm) is located in the large part of the whole drill core with the most dense data point concentrations within 160-230 m in the altered skarn, sericite schist and cordierite schist sequences, and within 250-284 m in the sericite schist, amphibolite, and cordierite schist units. Acidity has been probably the factor that has shifted the equilibrium of the white mica.

The phengitic (low octahedral) group (>2210 nm) is extending throughout the whole drill core (Fig. 33), and refers to high pressure conditions (Velde 1965). Therefore, there are less distinctive alteration trends visible in the AlOH peak locations, but in example when the lithological unit changes to the sericite schist in the end of the drill core, the AlOH peak locations shift from phengitic compositions to ~2200-2210 nm interval of muscovitic composition. This can be also seen in Figure 30 in more precise mineralogical SWIR data.

7.2 Results of drill core MM-196

This drill core begins with a short sequence of amphibolite and gradually alternates to the mica schist (Fig. 16). Within this drill core the sulphidic minerals appear as disseminated and are hosted by skarn, cordierite schist, and sericite schist lithologies. As can be seen from the geochemical data in Figure 34, the skarn units are characterized with the decrease of SiO_2 and Al_2O_3 contents and the increase of CaO, MgO and MnO contents. The end part of the drill core is mainly cordierite schist that first alternates with sericite schist, then with mica schist. The rest of the drill core (80-153.60 m) is logged as cordierite schist with several narrow, mineralized zones with sulphidic minerals (Fig. 16). The density, conductivity, and magnetic susceptibility anomalies correlate well with the observed and logged ore minerals (Fig. 34).

The CI and AI ratios show both similar trends in this drill core (Fig. 34). There are rapid decreases adjunct to the skarn units, and the indices show also high values within the cordierite schist units. The trends of CCPI remind the AI and CI contents except there is a steep dip within the depth of 70 m in a cordierite schist unit. Hashiguchi index shows similar kind of decreasing trends with skarn units than the CI and AI, but there is also a gradual decrease within the cordierite schist unit with a minimum value being located in 122 m. In the depth of 121.90-122.00 m there is a narrow, chloritized clay-containing zone that can be seen as an increase in MgO content. Just before this narrow zone there is a sharp rise in Cu content in 119 m depth that correlates with the conductivity data and can be seen also as a small peak in the magnetic susceptibility data.

The similar gradually decreasing trend seen in Hashiguchi index can be seen in MgO content, but the minimum value is in the depth of 128 m, after the clay-containing zone (Fig. 34). After this there is a relatively rapid increase seen in MgO content, Hashiguchi index, and sericite crystallinity as well as simultaneously as two sharp decreases in CCPI ratio. There is also a small conductivity anomaly in the depth of 136 m within the cordierite schist unit. It seems to correlate with increasing SiO_2 and K_2O contents, and a Rb/Sr anomaly located at the same level.

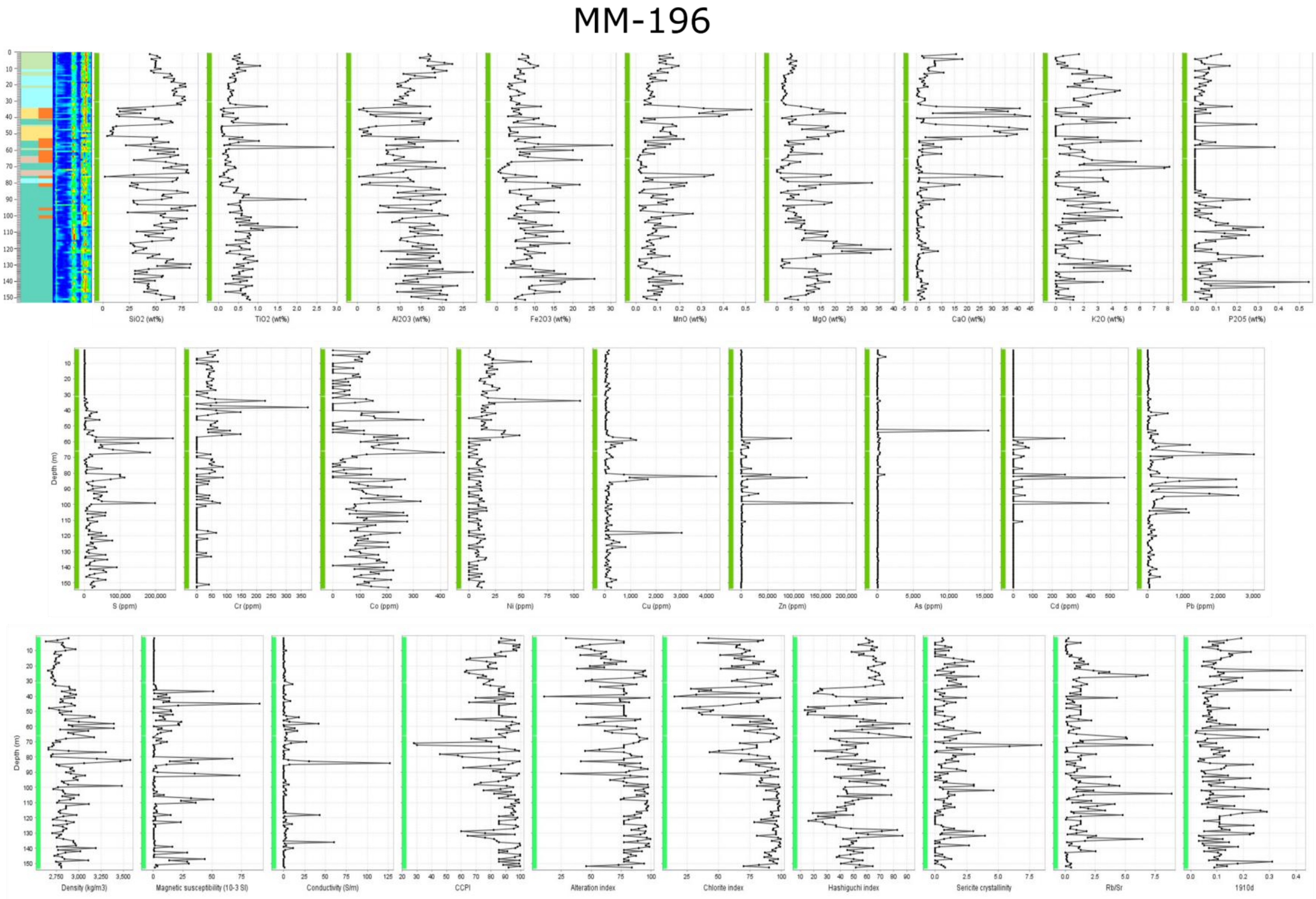

Figure 34. The geochemical, petrophysical, and alteration data of the drill core MM-196. On the upper left corner there is the logged lithology of the drill core. Explanations of the lithology as in Figure 16.

As represented in Figure 35, in the drill core MM-196 there is an emphasis on the presence of chlorite group minerals, but also a considerable amount of muscovite. Some montmorillonite is also observable in the data. A considerable amount of the measured phases is identified as aspectral within the SWIR wavelength.

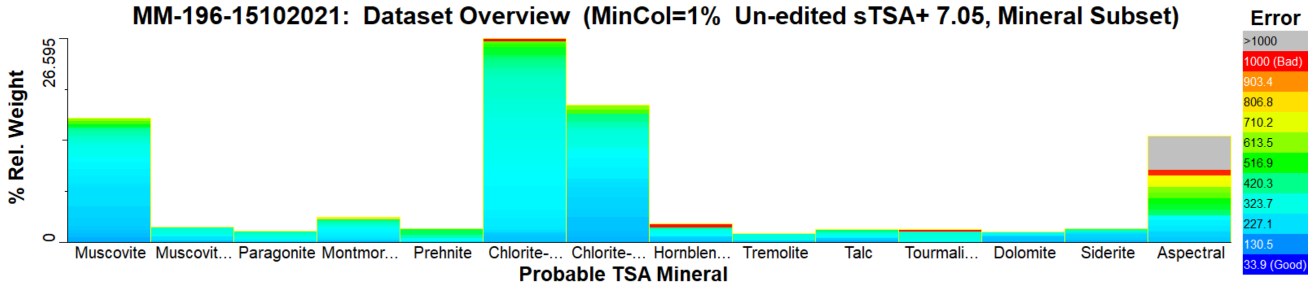

Figure 35. The summary of the mineral phases present in the drill core MM-196 detected short-wave infrared (SWIR) spectroscopy and automatically identified by The Spectral Geologist.

The comparative mineralogical SWIR and pXRD data in Figure 36 give differing results when compared to each other. The amount of amorphous material is a considerable one in the pXRD measurements from the depths of 51 and 140 m.

The amount of cordierite varies considerably within the drill core (Fig. 36) even though the cordierite schist is a dominant lithological unit (Fig. 16). According to the pXRD data (Fig. 36), the amount of cordierite decreases towards the mineralisation showing signs of pinitization. Pinitization can be seen first as cordierite altering to chlorite, muscovite, and quartz or aluminium silicate (like cyanite, andalusite and sillimanite), and then breaking down to chlorite, aluminium silicate or pyrophyllite, and quartz together with simultaneous sericitization (Ogiermann & Kalt 2000).

Andalusite is observed only in the depth of 87 m associated with a large amount of cordierite, quartz, and albite, and with no sulphidic minerals (Fig. 36). In the next measurement point in 98 m the cordierite amount is halved, while quartz, illite, muscovite, clinochlore, and albite are abundant, and pyrite reappears. In 101 m there is only small amount of cordierite left, and instead, plenty of phengite, albite, clinochlore, quartz, and vermiculite is evident. A small amount of pyrite and pyrrhotite is present. In 106 m cordierite is no more observed: instead, there is plenty of quartz, chamosite, albite, pargasite, montmorillonite, and spinel, and a good amount of pyrite, pyrrhotite, and sphalerite.

However, in the next measurement point in 125 m ¼ of the sample is cordierite with albite, quartz, clinochlore, illite, talc, and pyrope. As accessory minerals montmorillonite, pyrite, and sphalerite are observed (Fig. 36). Nevertheless, it seems that cordierite has been broken down again in 133 m: remaining there is a great amount of quartz, illite, albite, clinochlore, and biotite, but no sulphidic minerals. In the end of the drill core cordierite reappears but in a less extent. It is accompanied by phlogopite, clinochlore, albite, quartz, and again some pyrite.

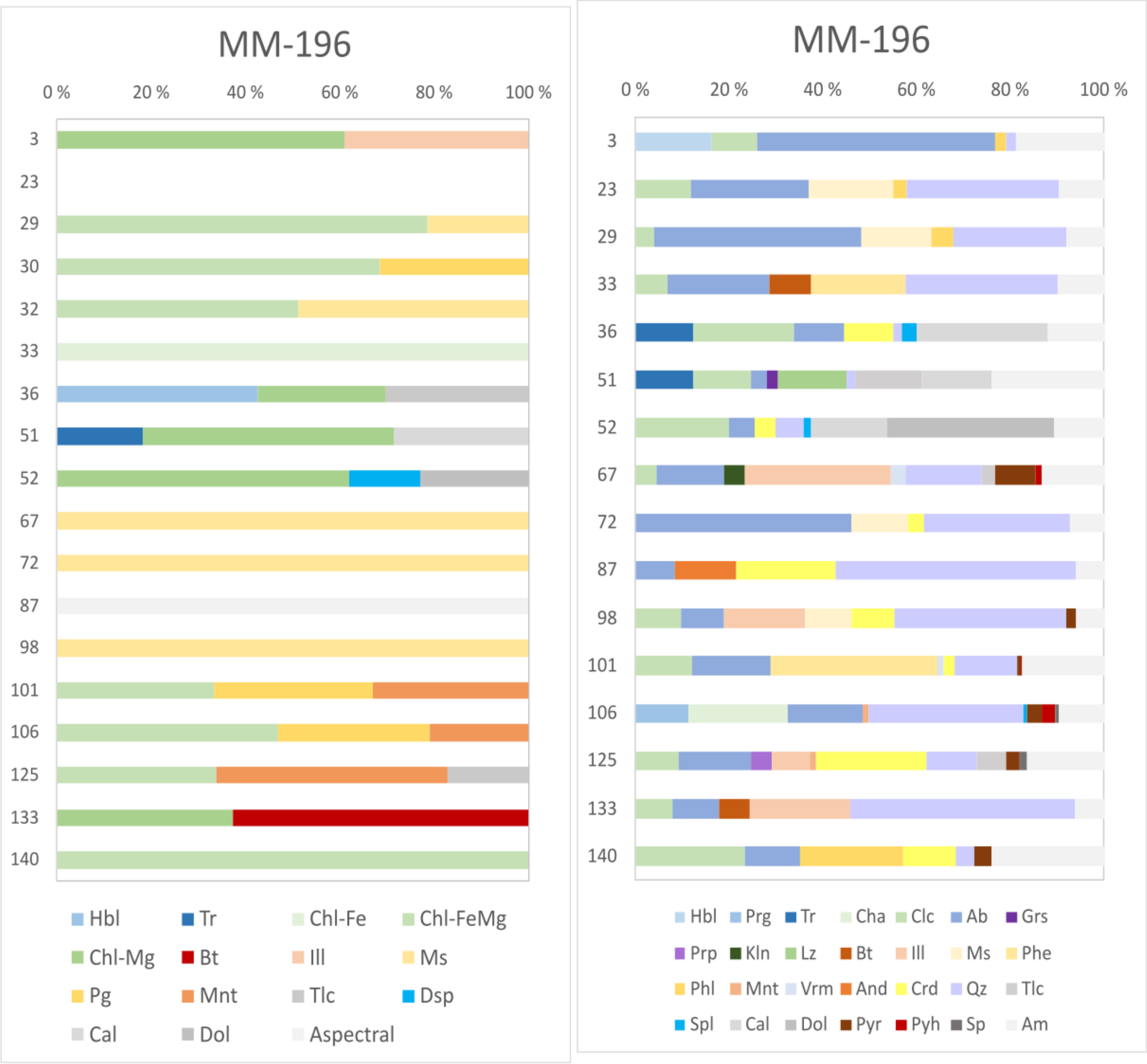

Figure 36. The mineralogical data of the drill core MM-196 by mineral. Left: The short-wave infrared (SWIR) data. Right: The portable XRD (pXRD) data. Explanations as in Figure 30.

The SWIR data consisting of all the data from this drill core (Fig. 37) show a correlation with most of the detected and logged ore deposits and the Mg-containing chlorite group phases. In several of the areas associated with the ores there is also montmorillonite present referring to argillic alteration. Both Mg-bearing chlorite and montmorillonite re-appear within the logged cordierite schist between 115-130 m where there is also some talc.

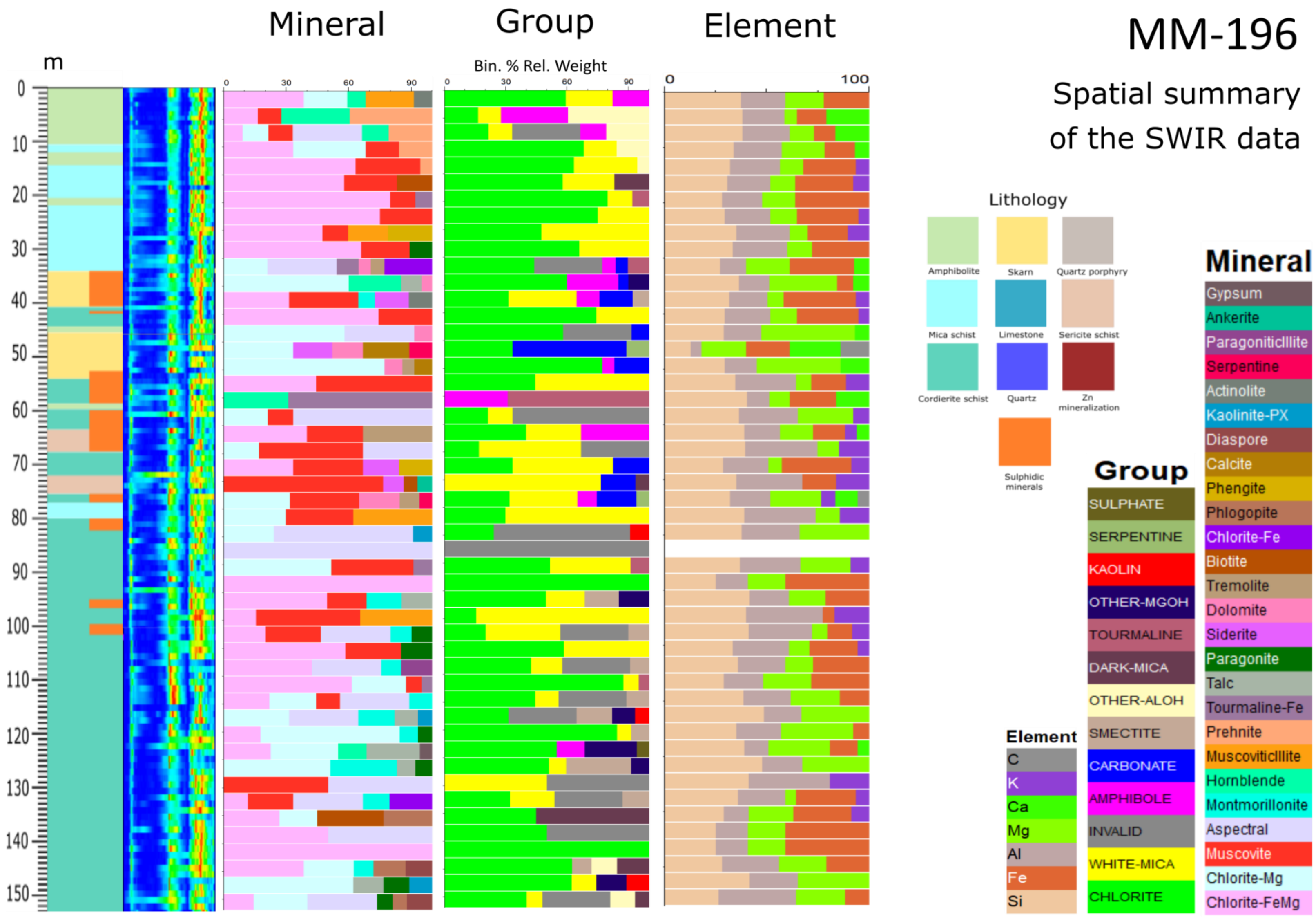

Figure 37. The visualized short-wave infrared (SWIR) data of the drill core MM-196.

Within this drill core it is slightly more difficult to tie the lithological units to the wavelength positions of AlOH, FeOH, and MgOH absorption features (Fig. 38) than with the drill core MM-190. In the beginning of the drill core in the amphibolite unit the wavelength positions of MgOH absorption features occur within 2320-2330 nm, and when the unit shifts to the mica schist, the MgOH absorption features shift to >2340 nm wavelength region. When there is a change to the skarn, the MgOH absorption features move to 2310-2340 nm scale. After the end of the skarn unit the cordierite schist begins to alternate with the sericite schist, and the MgOH absorption features appear in a wider range.

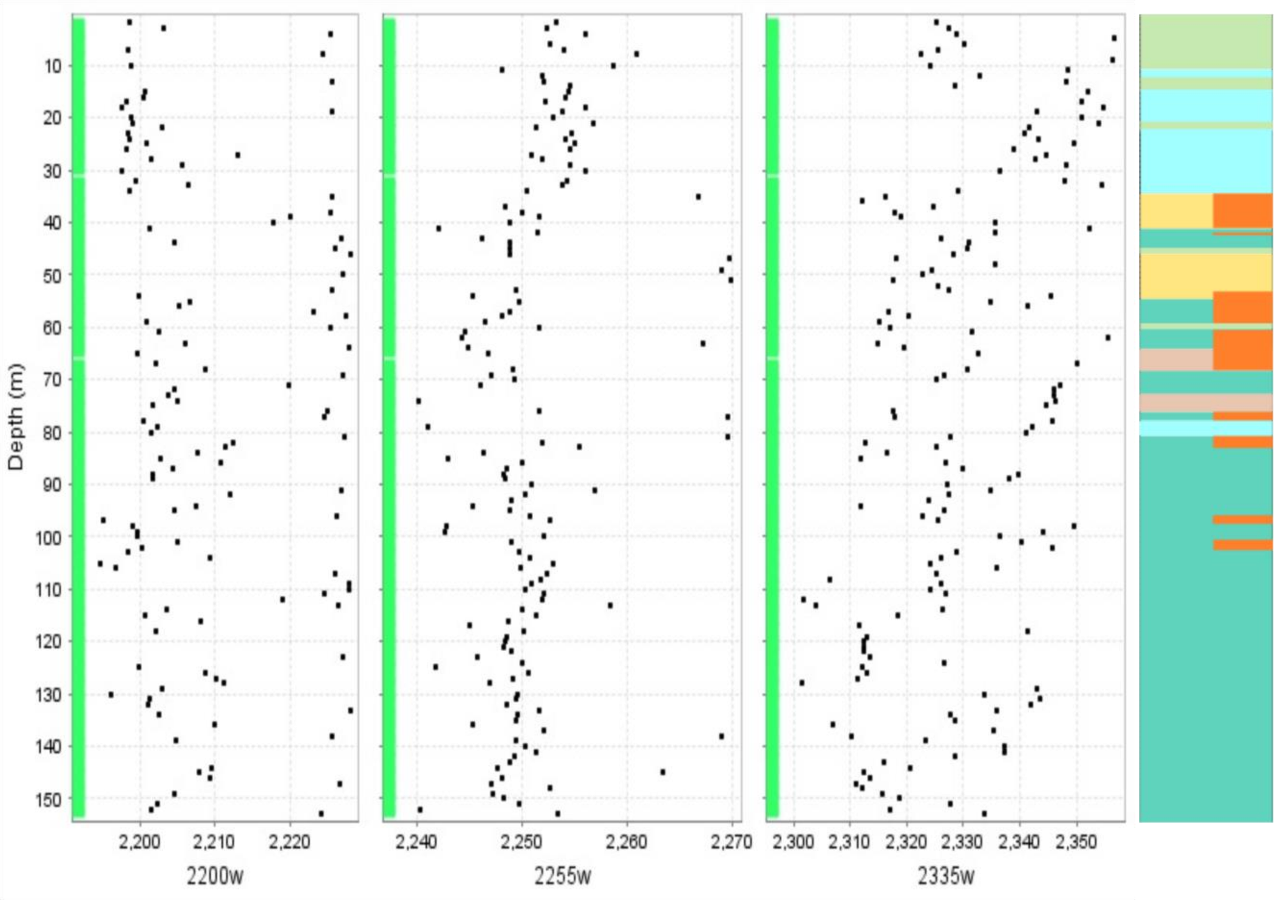

Figure 38. The wavelength positions of AlOH (2200 nm), FeOH (2255 nm) and MgOH (2335 nm) absorption features plotted against the depth of the drill core MM-196. The horizontal scale is in nanometres. On the right-hand side there is the logged lithology of the drill core. Explanations of the lithology as in Figure 37.

The wavelength positions of AlOH absorption features are splitted into three different compositional groups within this drill core as well (Fig. 38). The paragonitic group with AlOH wavelength <2200 nm is not that well distinguishable one in this drill core. Majority of the AlOH absorption features are plotted between 2200-2210 nm to the muscovite group. Almost throughout the whole drill core there are also some phengitic white mica (>2210 nm). The white mica compositions do not seem to be that well connected to the appearance of the sulphidic minerals.

7.3 Results of drill core MM-198

Considering the recorded lithologies (Fig. 16), this drill core is very similar to the drill core MM-196. Both are located very close to each other, and the drill core MM-198 is 30 metres shorter than the drill core MM-196. It also begins with a short sequence of amphibolite and then sharply alternates to mica schist. The drill core MM-198 hosts a quartz porphyry unit within 72-83 m that does not appear in the drill core MM-196, and the sericite schist unit it has is a very narrow one, only 20 cm wide. The appearance of sulphidic minerals within this drill core is bound to the skarn and cordierite schist units. The end part of the drill core is mainly cordierite schist that first alternates with the skarn and then shortly turns to the sericite mica and then to the wider quartz porphyry unit.

As can be seen in Figure 39, the skarn units (39.10-60 m) show a decrease in SiO_2 and Al_2O_3 contents, and increase in CaO, MgO and MnO contents. Some of the K_2O measurement data are missing within 46-53 m and therefore there seems to be a drop in these values.

The presence of sulphidic minerals in the depth of 70-85 m can be seen well as increases in S, Cu, Zn, Ag contents, and as density and conductivity anomalies (Fig. 39). In addition, there is a decrease in SiO_2 and Al_2O_3 contents and an increase in TiO_2 and Fe_2O_3 contents. The dispersed sulphidic minerals in the depth of 55-67 m are not that well visible in the geochemical and the density data but can be seen as magnetic susceptibility and conductivity anomalies.

In the end of the drill core there is a considerable high MgO, Pb, and Ag contents, and conductivity and magnetic susceptibility anomalies (Fig. 39). It is not recorded in the original loggings that here would be any sulphidic minerals (Outokumpu Oy 1959c), but in the visual drill core logging their presence was obvious.

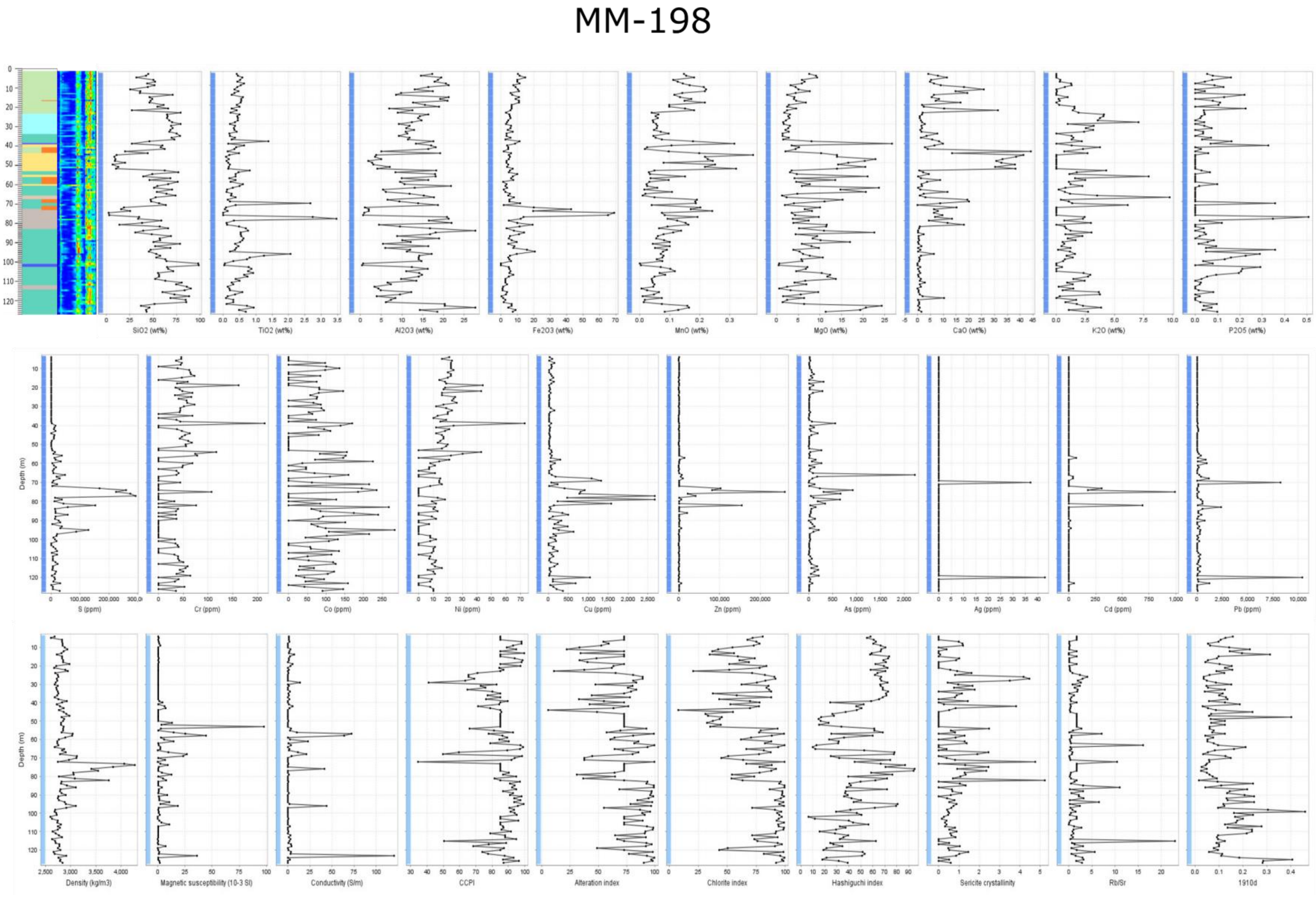

Figure 39. The geochemical, petrophysical, and alteration data of the drill core MM-198. On the upper left corner there is the logged lithology of the drill core. Explanations of the lithology as in Figure 16.

The distribution of minerals according to the SWIR data in the drill core MM-198 (Fig. 40) resembles a lot the similar data obtained from the drill core MM-196. The chloritic alteration is well evitable in both as well as abundant amount of muscovite. Since the drill cores are located relatively close to each other, this makes sense. However, in the drill core MM-198 there is more montmorillonite and prehnite present than in the drill core MM-196.

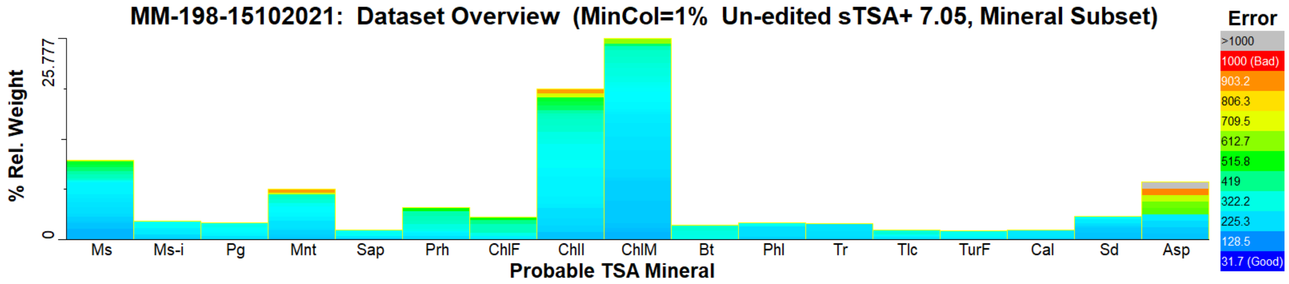

Figure 40. The summary of the mineral phases present in the drill core MM-198 detected by short-wave infrared (SWIR) spectroscopy and automatically identified by The Spectral Geologist.

Figure 41 shows, that the first pXRD measurements in the depths of 4 m and 14 m have a considerable amount (<20 wt%) of amorphous material according to XPowder, and therefore the mineral interpretations here should be approached with care, especially regarding their relative contents. The pXRD diffractogram in 4 m is unclear, but it clearly shows that there is prehnite together with albite, chamosite, and quartz present. The SWIR data confirm the presence of prehnite and Fe-containing chlorite group mineral.

The pXRD diffractogram in the depth of 14 m is unclear. It shows a considerable amount of albite, clinochlore, some epidote, calcite, quartz, cordierite, and montmorillonite (Fig. 41). The SWIR data (Fig. 41) confirms the presence of Mg-rich chlorite, epidote, and montmorillonite. There is also some hedenbergite as a pyroxene present. It is a mineral that can be often found in skarns. However, this lithological unit has been logged as diopside-amphibolite.

In the depth of 17.30 m some arsenopyrite appears according to the original logging (Outokumpu Oy 1959c). It can be seen as a small peak in arsenic in the geochemical data (Fig. 39), but it is missing in the pXRD data from the 17 m depth since there were no arsenic-bearing mineral phases identified with the pXRD (Fig. 41). This is probably due to small sample amount needed for the pXRD analysis, so the sample taking has been local and does not cover large area. The pXRD data in Figure 41 show a relatively large amount of albite, actinolite, muscovite, diopside, quartz, and clinochlore, and the SWIR data identify Fe-Mg-containing chlorite group phases, hornblende, and muscovite.

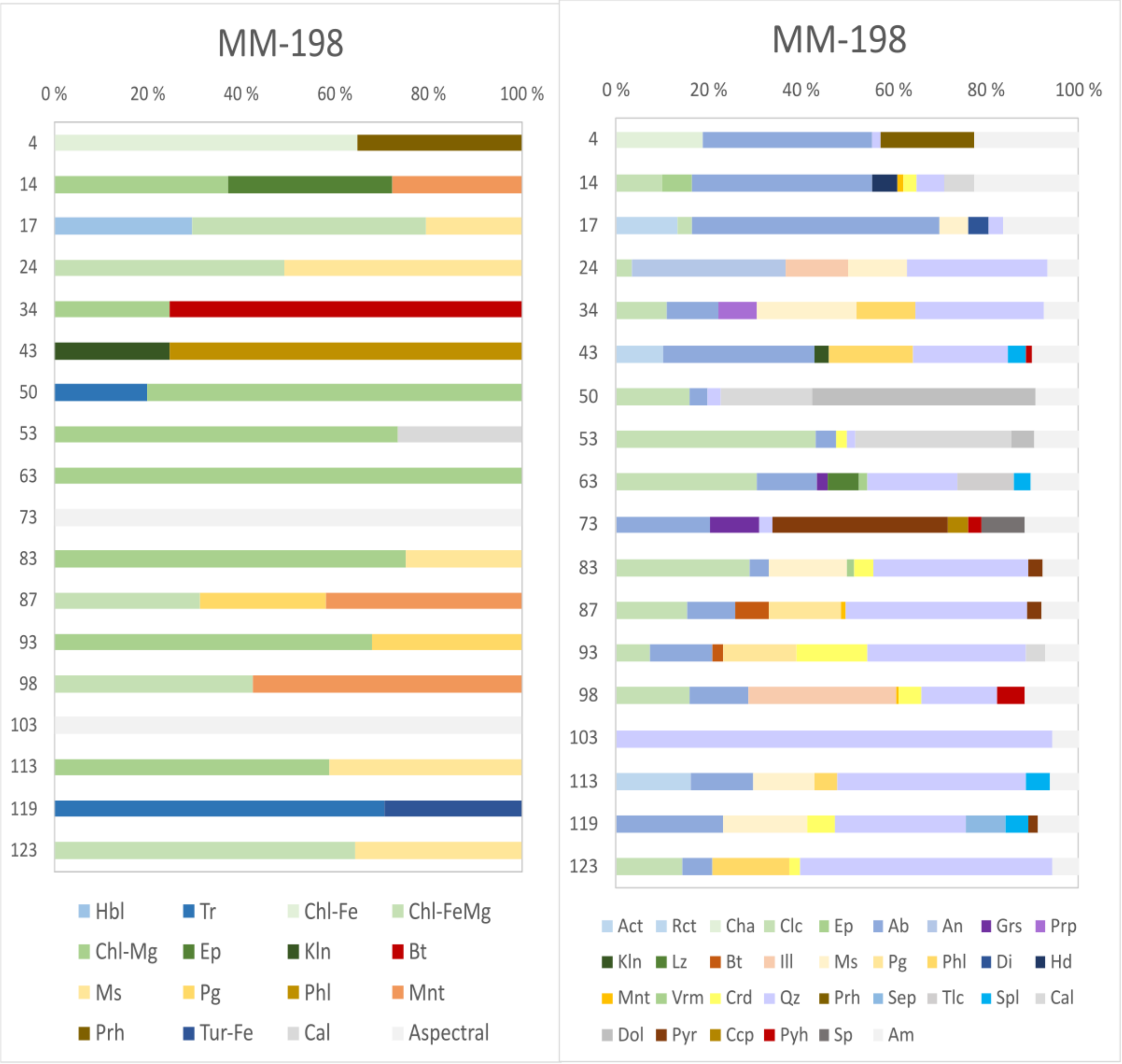

Figure 41. The mineralogical data of the drill core MM-198 by mineral. Left: The short-wave infrared (SWIR) data. Right: The portable XRD (pXRD) data. Explanations as in Figure 30.

As can be seen in the visualized SWIR data in Figure 42, a significant Mg-chlorite anomaly around the sulphidic minerals is appearing in the depth of 40.70-43.50 m and 55.40-59.45 m. The former is surrounded by the carbonate rocks, and the latter is surrounded by the cordierite schist (Fig. 16; Outokumpu Oy 1959c). Around the next mineralizations in the depth of 66.97-67.41 m and 71.36-72.90 m there are more complex and altered lithologies of white mica, montmorillonite, prehnite, and ankerite. Here ankerite is probably bearing some manganese also visible in the elemental distribution data by TSG. TSG has been able to identify siderite here as well, which would be one of the Fe-bearing minerals.

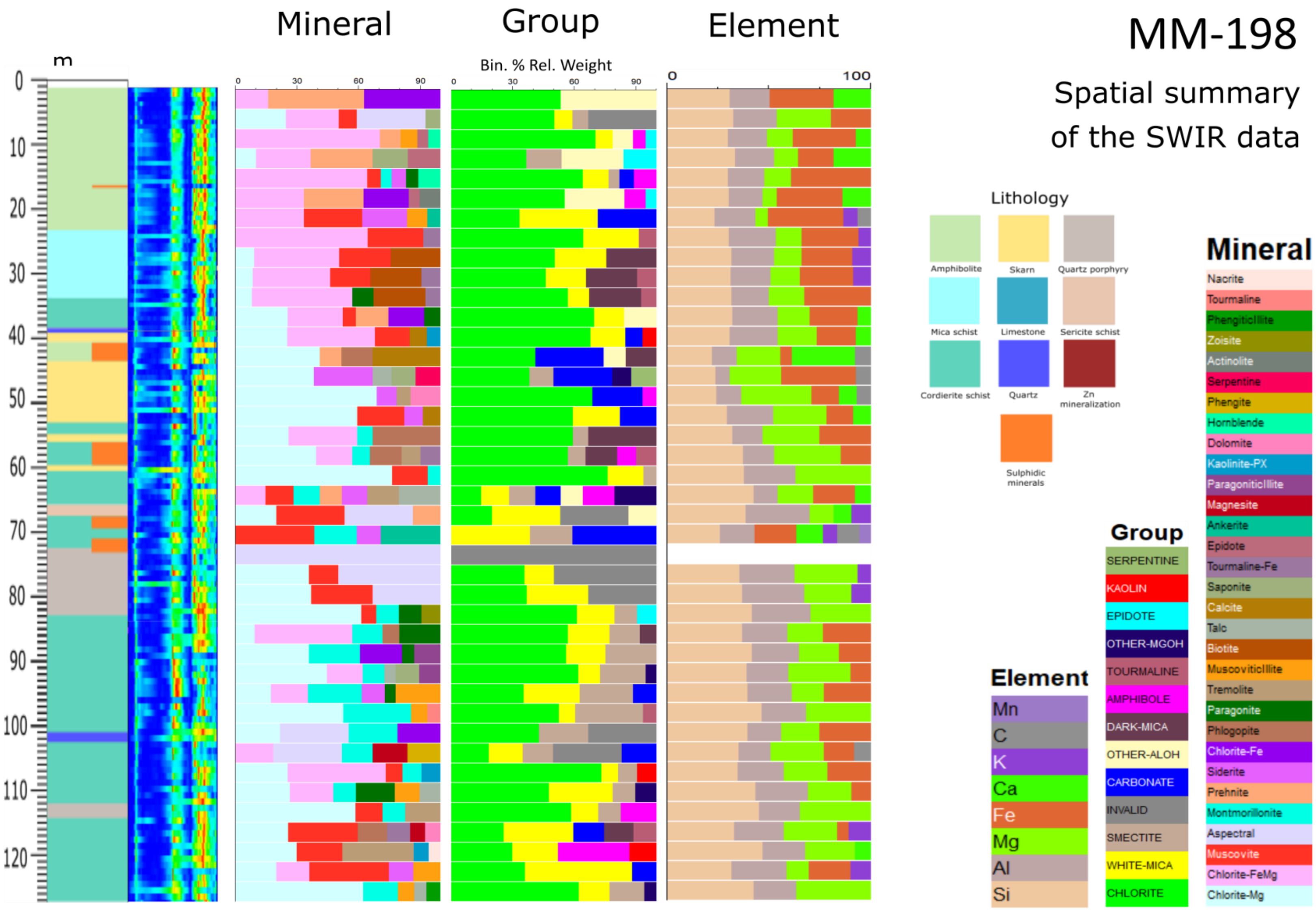

Figure 42. The visualized short-wave infrared (SWIR) data of the drill core MM-198.

In the depth of 73 m some data is missing from the SWIR data (Fig. 42) since the spectrum has been interpreted aspectral by TSG. The pXRD data (Fig. 41) show a pyrite-rich zone with plenty of sphalerite, chalcopyrite, and pyrrhotite. There is also plenty of grossular garnet, quartz, and albite present. There is again some data missing in 103 m in the SWIR data (Fig. 42) since TSG identified the mineral content as aspectral. The pXRD data (Fig. 41) here show only quartz and some amorphous material, and according to the original logging data (Outokumpu Oy 1959c), there is a quartz vein in the depth of 101.35-102.55 m. The natural explanation for this would be that the sample has been taken from the quartz vein and not from the following cordierite schist unit.

The wavelength positions of the AlOH, the FeOH and the MgOH absoprtion features of the drill core MM-198 in Figure 43 show slightly unclear trends in connection with the lithologies. Perhaps the most distinguishable trends can be seen within the FeOH absorption feature wavelength positions. In the beginning of the drill core within the amphibolite sequence most of the FeOH absorption features are located within 2250-2260 nm. The wavelength positions of the FeOH absoprtion features stay more or less within 2250-2255 nm in the mica schist unit, and shift to 2245-2250 nm range in the skarn and the cordierite schist. There is more variation within the quartz porphyry unit.

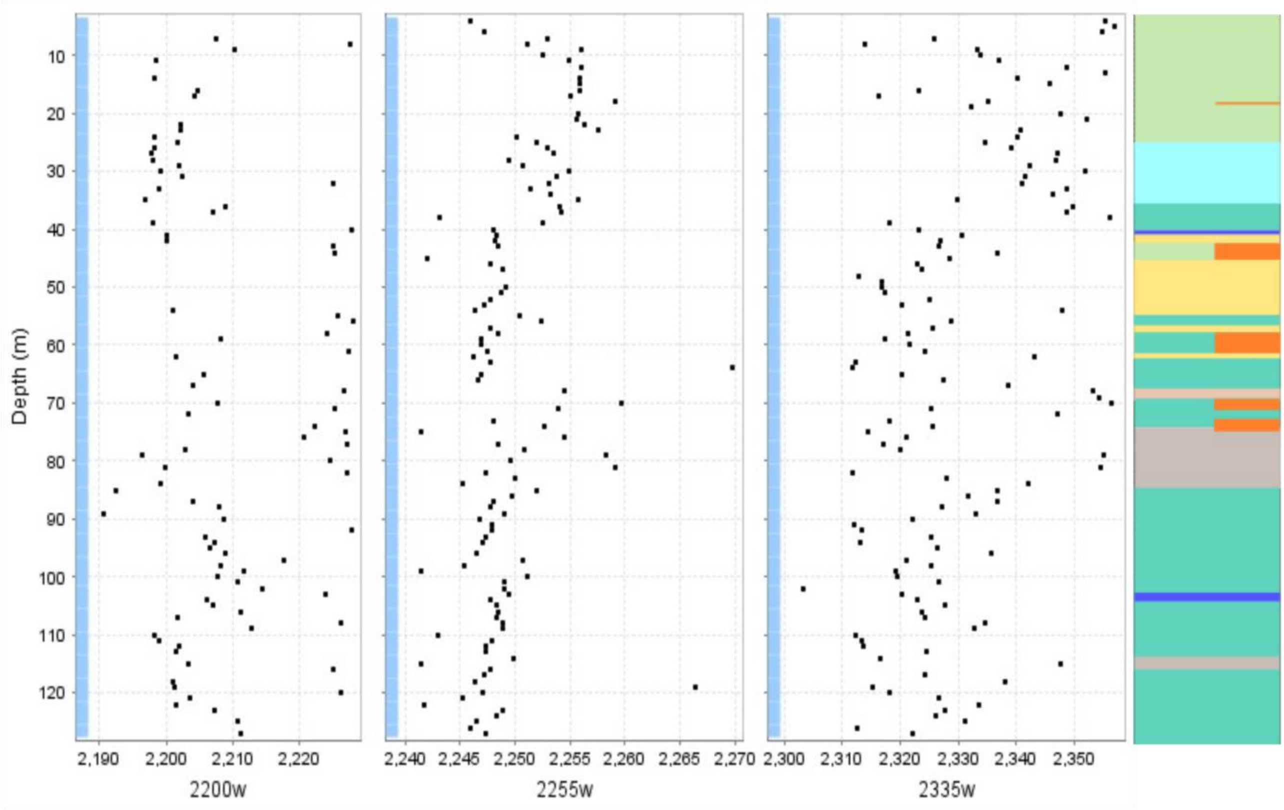

Figure 43. The wavelength positions of AlOH (2200 nm), FeOH (2255 nm) and MgOH (2335 nm) absorption features plotted against the depth of the drill core MM-198. The horizontal scale is in nanometres. On the right-hand side there is the logged lithology of the drill core. Explanations of the lithology as in Figure 42.

In the beginning of the drill core some of the AlOH absorption feature locations show paragonitic compositions (<2200 nm) within the amphibolitic and the mica schist sequences (Fig. 43). Regarding the sulphidic minerals, there is a slight trend in the AlOH absorption feature locations: when the sulphidic minerals appear in the depth of 40 m, the wavelength positions of the AlOH absorption features shift to the phengitic scale (2225-2230 nm). It is more difficult to find any clear trends in the MgOH absorption feature locations. There seems to be a division between muscovitic (2200-2210 nm) and phengitic (>2210 nm) compositions within the area where the sulphidic minerals appear, which probably reflects the lithological variation of these sequences. In the amphibolite unit, the wavelength positions of the MgOH absorption features are dispersed to a wider scale, but when the unit shifts to the mica schist, the MgOH absoprtion features shift to >2340 nm scale.

7.4 Results of drill core MM-241

This drill core is very different to the other drill cores in this dataset in terms of lithology. According to the previously recorded lithologies (Fig. 16), it begins and ends with amphibolitic sequences, and in the middle, it is dominated by large sequences of quartz porphyry. There is only a narrow sequence of cordierite schist present. Sulphidic minerals are dominantly hosted by skarn units, as in the other drill cores (Outokumpu Oy 1961).

In Figure 44 in the amphibolite unit within 12.17-21.55 m there is an increase in TiO_2, P_2O_5, Fe_2O_3, and MnO contents, and a decrease in SiO_2 content. In the larger skarn unit in 78.15-87.08 m there is a decrease of Al_2O_3 content and an increase of MgO content with smaller increases in CaO, Fe_2O_3, and MnO contents.

The appearance of sulphidic minerals can be seen as increases of S, Cu, Zn, Ag, Pb, and some Cd contents with noticeable density and conductivity anomalies (Fig. 44) in 39.90-40.75 m, 44.76-46.40 m, and 75.90-87.08 m. The appearance of sulphidic minerals can also be seen as increases in Rb/Sr ratio and decreases in Hashiguchi index. In addition, there are increases in Cu, As and some S contents in the beginning of the drill core (in 17 m) where the amphibolite unit has been logged to be slightly broken and coarse-grained. Cr and Ni contents show also sharp increases in the depth of 20 m. In the end of the drill core a magnetic susceptibility anomaly starts from ~90 m, and the Hashiguchi index increase together with CCPI. There is also an individual peak of Cu content in 122 m. This unit has been logged as more or less even amphibolite with some epidote-grossular garnet agglomerations (Outokumpu Oy 1961).

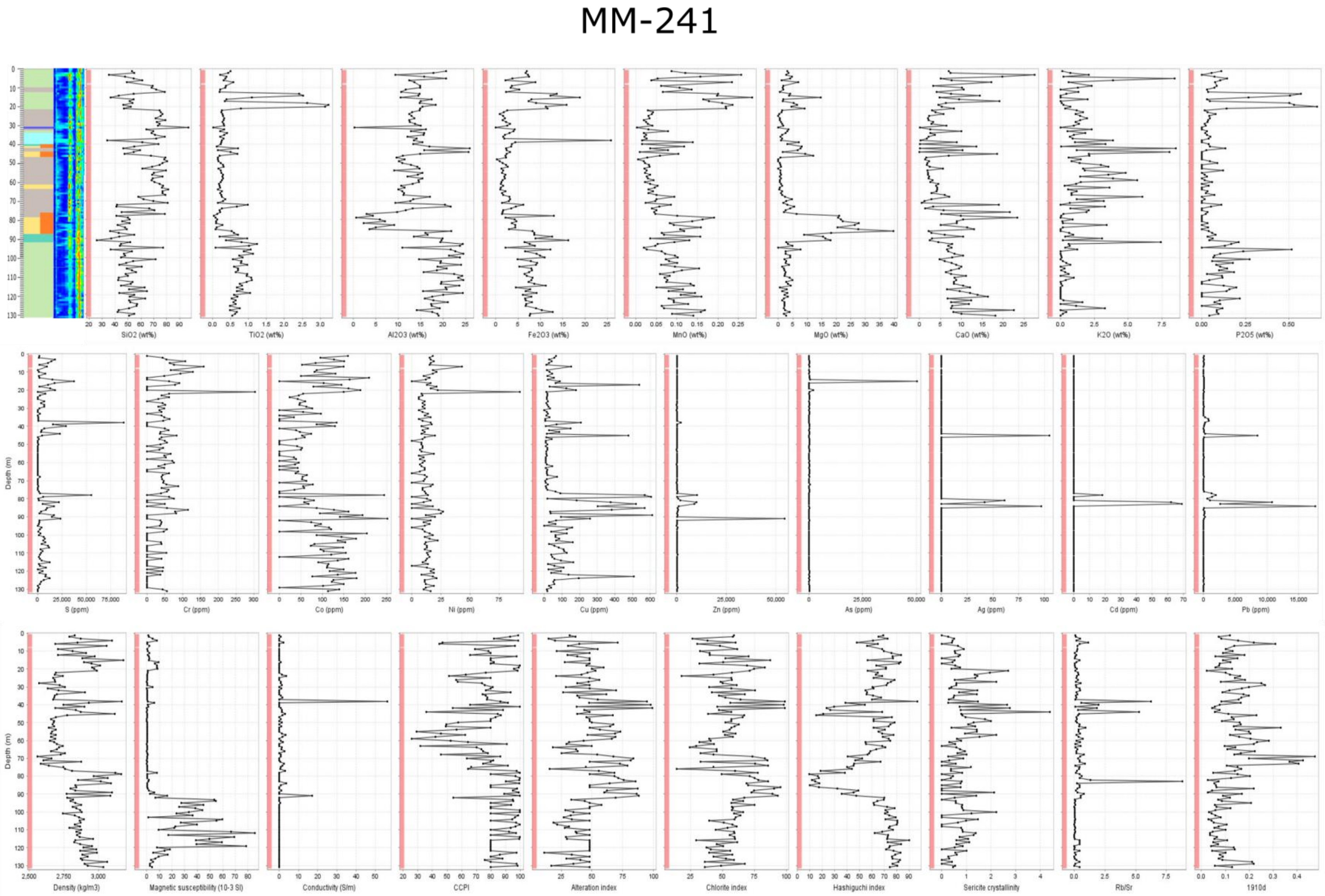
MM-241

Figure 44. The geochemical, petrophysical, and alteration data of the drill core MM-241. On the upper left corner there is the logged lithology of the drill core. Explanations of the lithology as in Figure 16.

The overall summary of the mineral phases in the drill core MM-241 detected within SWIR wavelength and identified with TSG (Fig. 45) shows again a considerable amount of chloritic alteration within this drill core. There is a remarkable amount of muscovite present in the data. The overall quality of the measurements is good, and only small portion of the phases were identified as aspectral.

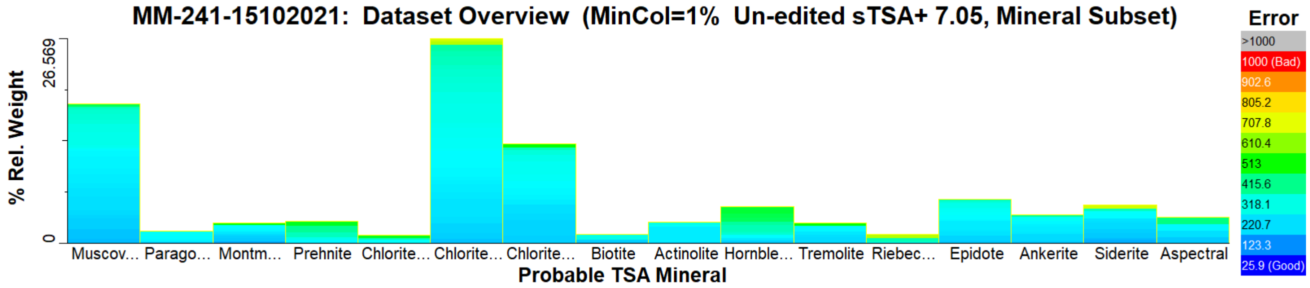

Figure 45. The summary of the mineral phases present in the drill core MM-241 detected by short-wave infrared (SWIR) spectroscopy and automatically identified with The Spectral Geologist.

The comparative SWIR and pXRD data in Figure 46 show that there is some SWIR measurement data missing from 105 and 115 m, and a considerable amount (≥ 20 wt%) of amorphous material in the pXRD data in 15, 85 and 115 m. In 105 m the pXRD data shows a great amount of albite, phlogopite, actinolite, quartz, epidote, and grossular garnet. In 115 m plenty of albite, clinochlore, quartz, some grossular and pyrrhotite are identified, and the amphibole here is tremolite.

The garnet type varies within the drill core. According to the pXRD data (Fig. 46), the garnet appears as pyrope in the beginning of the drill core in 5 and 15 m, and as grossular in the end of the drill core in 105 and 115 m. According to the SWIR data, some variation is also present within different amphiboles. Between 78-86 m there is a clear presence of sulphidic minerals, and most of the amphiboles would be tremolite. The pXRD measurement from 85 m confirms the amphibole phase to be tremolite. In the end of the drill core the amphibole composition alternates between hornblende and riebeckite. There are several observations of epidote in both the SWIR and the pXRD data when compared to other drill cores.

The SWIR data in Figure 47 show that there are concentrations of Mg-rich chlorite group minerals where the sulphidic minerals hosted by the skarn units appear in the depth of 39.90-40.75 m, 44.76-46.40 m and 75.90-87.08 m that is also evidenced in the original logging report (Outokumpu Oy 1961). There is also a significant amount of different amphibole group minerals in the latter concentration of sulphidic minerals, most dominantly tremolite. The quartz porphyry units are dominated by the chlorite group minerals of intermediate Fe-Mg composition and muscovite. Muscovite appears before, around, and after the first sulphidic mineral concentrations in 39.90-40.75 m and 44.76-46.40 m.

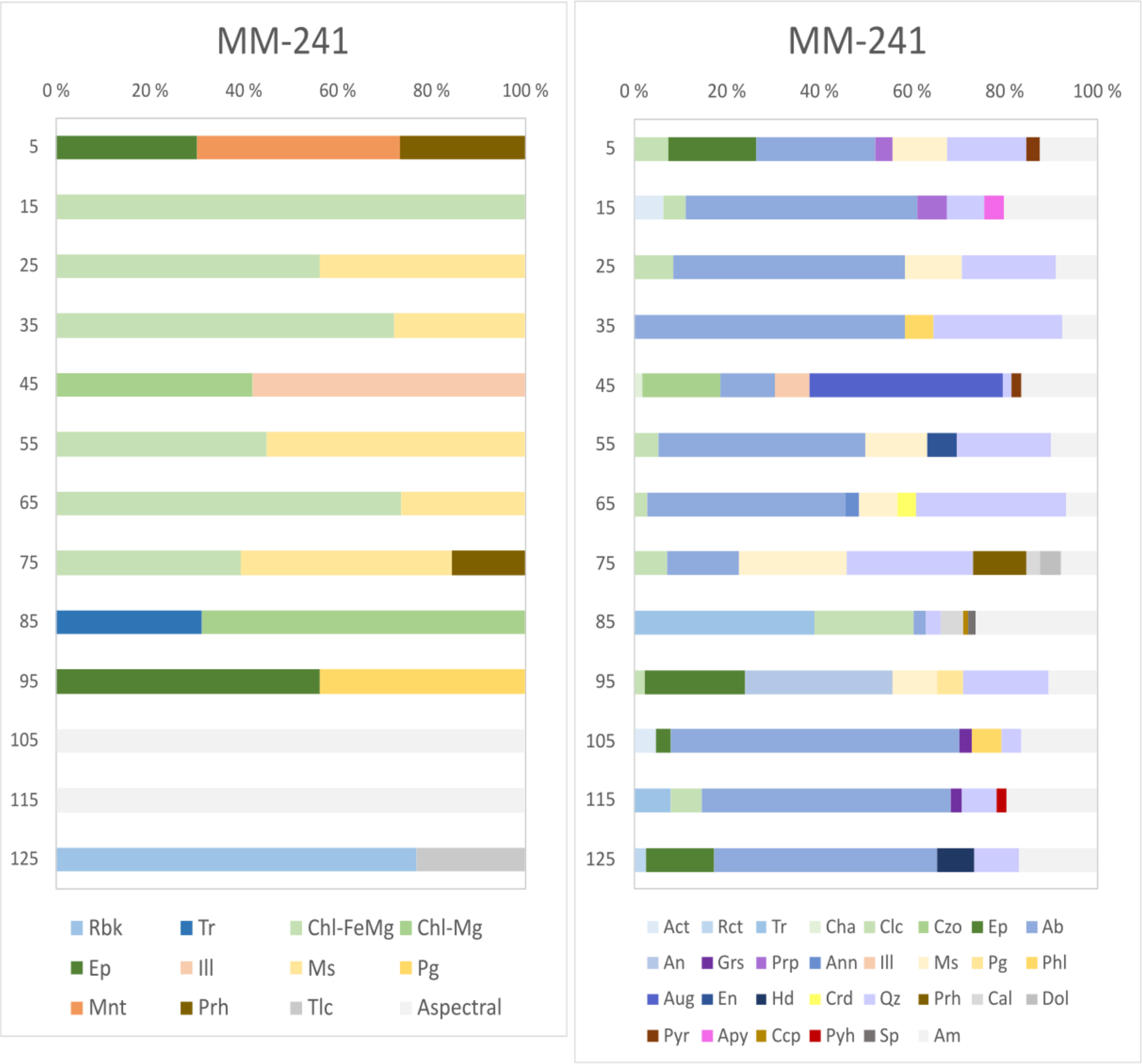

Figure 46. The mineralogical data of the drill core MM-241 by mineral. Left: The short-wave infrared (SWIR) data measured with Terraspec. Right: The portable XRD (pXRD) data. Explanations as in Figure 30.

Interestingly the Mg-rich chlorite appears again within 105-115 m in the SWIR data (Fig. 47) together with the irregular anomalies of magnetic susceptibility (Fig. 44). The pXRD data (Fig. 46) show a slight amount of disseminated pyrrhotite in the depth of 115 m, which probably explains the appearance of Mg-rich chlorite and the magnetic anomalies.

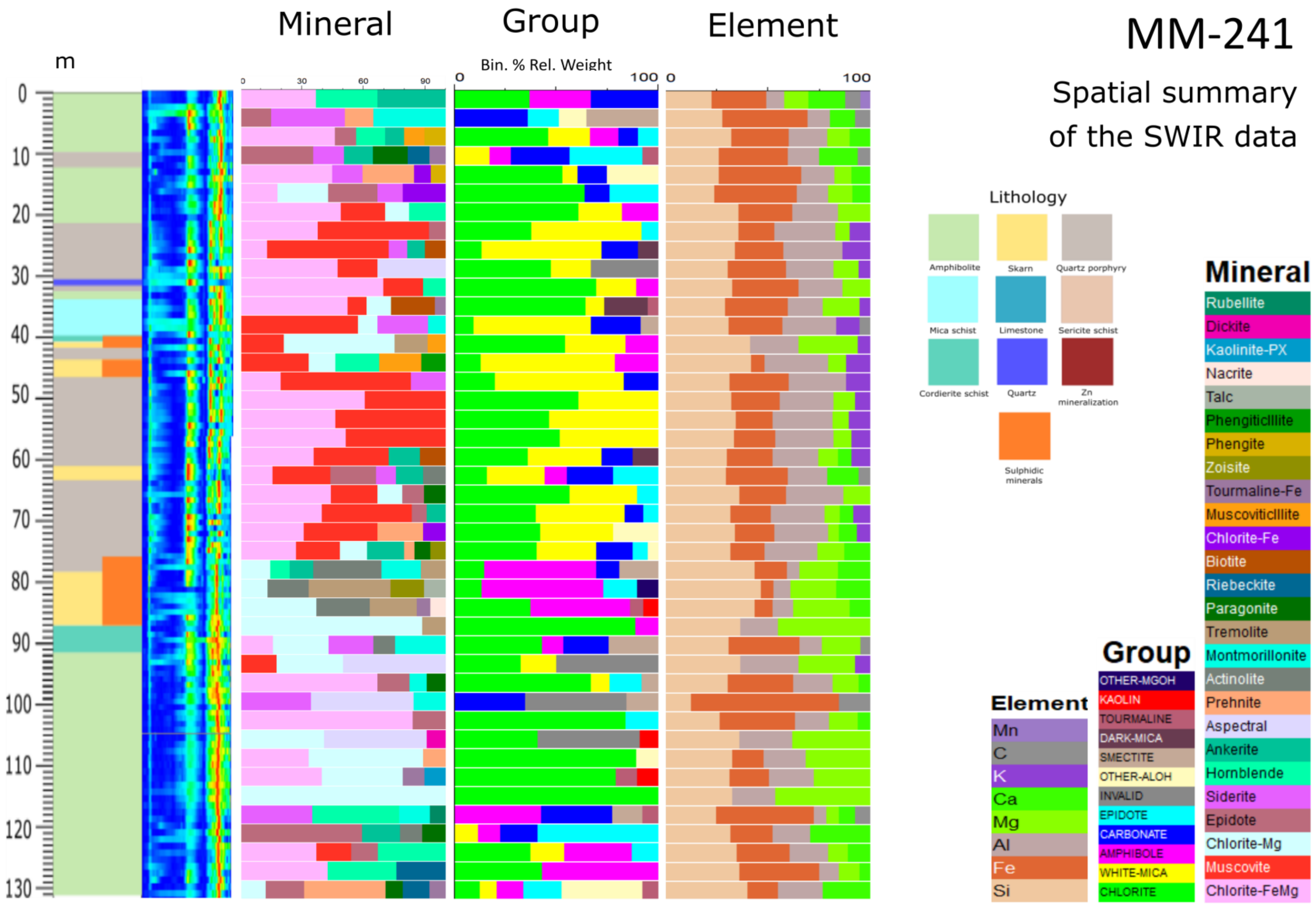

Figure 47. The visualized short-wave infrared (SWIR) data of the drill core MM-241.

The SWIR data linked to the lithological data with the wavelength positions of AlOH, FeOH, and MgOH absorption features in Figure 48 show a shift of AlOH absorption features to the muscovitic range (2200-2210 nm) with some phengitic (2210-2215 nm) compositions when the lithological unit changes from amphibolite to quartz porphyry. Within the mica schist unit between the quartz porphyry sequences the AlOH composition is muscovitic. In the quartz porphyry sequences the wavelength positions of MgOH would be typically within 2340-2350 nm. The wavelength positions of the AlOH absorption features shift to more phengitic compositions (>2210 nm) when the lithological unit changes to skarn after 78.15 m. When the lithological sequence changes from the cordierite schist to amphibolite in the depth of 91.50 m, the FeOH and MgOH wavelength positions spread to a larger scale.

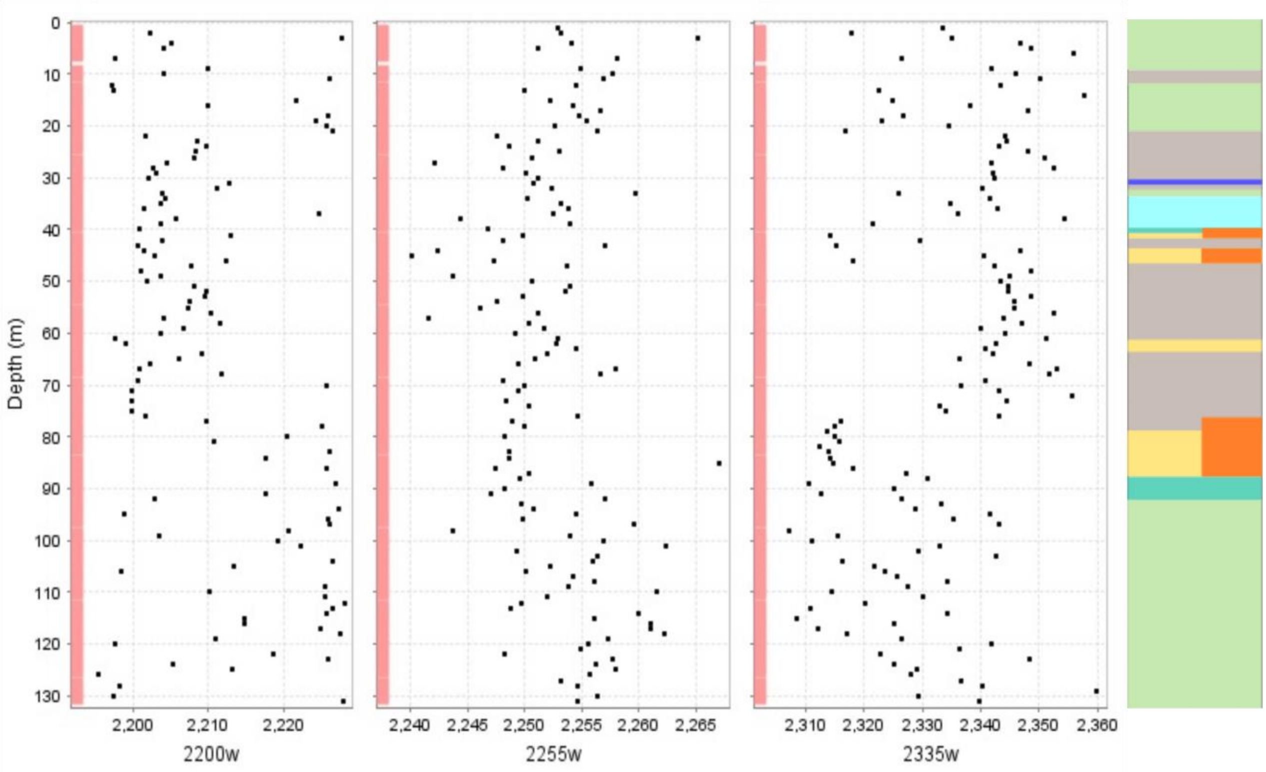

Figure 48. The wavelength positions of AlOH (2200 nm), FeOH (2255 nm) and MgOH (2335 nm) absorption features plotted against the depth of the drill core MM-241. The horizontal scale is in nanometres. On the right-hand side there is the logged lithology of the drill core. Explanations of the lithology as in Figure 47.

8 Discussion

8.1 Sources of error and limitations

First, it is important to understand that handheld measurement devices are manufactured and meant for different kind of analytical purposes than stationary, laboratory-based devices such as the laboratory XRD or scanning electron microscopy. The aim of the handheld equipment is to provide cost-efficient and time-saving workflows that take place on-site and preferably deliver the results as fast as possible so the data can be used to target the fieldwork to more feasible areas (e.g., Ross et al. 2013, Uvarova et al. 2014, Lemière & Uvarova 2020, Uvarova et al. 2020). Portable devices might be practical to use in the field or in the quality control context, but they do not aim to the same quality and accuracy that stationary devices would be able to provide. It is important to contemplate whether the chosen method provides accurate enough information to draw an overall picture of the target. Perhaps it is not reasonable to even begin to make direct comparisons between the accuracy of the handheld and stationary XRD devices but rather to think these methods as separate of each other.

Regarding the pXRD and the NIR spectroscopy, the results are only semiquantitative and directional in this study. Quantitative modelling with the XRD requires much more refined sample treatment procedures as well as longer measurements to reduce the background noise and improve the data quality. All the phases must be also identified to be able to quantify the composition properly, since all the identified phases that are included to the interpretation effect to the calculatory amounts. If one phase is taken away, then the relative amounts of other phases will change.

The comparative SWIR and pXRD data show significant differences between mineral identifications made with both methods (Figs. 30, 36, 41, 46). Some differences can be explained with the limitations of the methods as well as the data gathering and processing protocols. In the NIR spectroscopy data maximum of three mineral phases were recorded within the SWIR wavelength and maximum of two mineral phases within the VNIR wavelength. In the pXRD minimum of 3-5 phases were identified during the data processing, and in more complex samples more phases were recorded. Already these differences in the data collection make a great difference in the observation of mineralogical variation obtained with these two methods.

8.1.1 Sources of error of the portable X-ray diffraction

In general, in powder diffraction methods the diffractogram quality is strongly controlled by the sample treatment procedures (Will 2006). The physical properties of the sample affect to the sample treatment: the softness, grain size and shape of a mineral are the main factors that dictate the sample treatment procedure, in example whether the grinding of the sample would be needed. Careful sample treatment procedures include treating the sample in a way that avoids particle sorting, like dividing the sample powder carefully and then taking the sample from the middle of a sample bag, container, jar or equivalent so that particles with different densities would be included to the sample; homogenizing the sample to reduce the distribution in the grain sizes; and avoiding treating the sample with metallic instruments in order to not attract its magnetic minerals. However, it is difficult to develop one standard sample treatment procedure for XRD due to different physical properties that minerals have. Additionally, in natural samples minerals usually appear as assemblages making this task even more challenging.

In this study the samples were taken with Dremel directly from the drill core which grinds the sample into relatively fine powder. After taking the sample it was sieved with a small sieve to <150 µm to get rid of larger particles within the sample. However, it is important to keep in mind that this grain size is still very coarse regarding the powder diffraction methods since the ideal average grain size of the XRD would be 10-50 µm (Pecharsky & Zavalij 2009) and for Rietveld analysis 1-5 µm (Snellings 2014).

Generally, the sample amount used for the pXRD is relatively small, approximately 15 mg, and while it might be an advantage, it might pose several problems as well. Naturally, it would be a benefit in targets where saving the sample as much as possible would be a priority. However, the representativeness of the sample is questionable. In comparison, a side-loaded preparate made for Rietveld quantification measured with the laboratory XRD device would consume approximately 1.5-2.5 grams of the sample depending on the densities of the particles while a traditional XRD preparate made on glass would consume approximately 0.2 grams of the sample.

A small sample amount can be also an advantage since it allows to measure the consistency of one single large grain, such as a large garnet crystal. On the other hand, such a small sample amount might not give good enough a picture of the mineral distribution of larger samples such as drill cores from a certain sample depth that has been chosen for the analysis. If too small amount of sample is placed to the sample chamber, it might cause unclear, declining diffractograms with plenty of background noise, such as in Figure 49.

Consistency of the sample material is one factor affecting to the diffractogram quality (Sarala & Koskinen 2018). In this study, it was observed that sulphidic minerals caused background elevation and increased background noise in the diffractograms. Figure 50 shows an example of a sample with pyrite and relatively large amount (24.1 wt%) of amorphous material. The diffractogram contains plenty of background noise, and the peaks have widened and even merged.

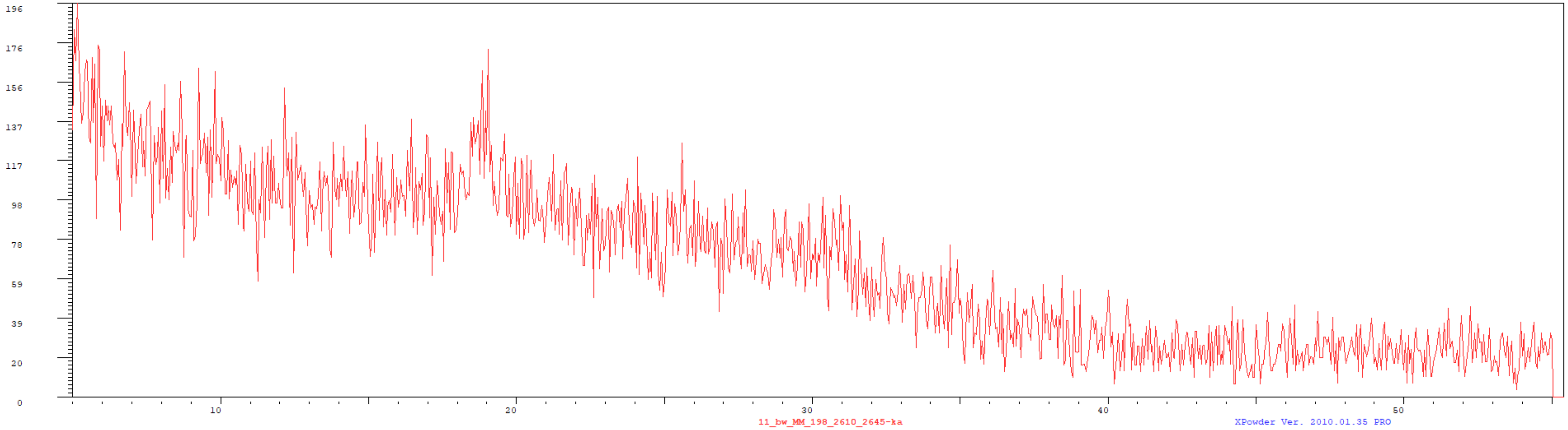

Figure 49. The diffractogram of the drill core MM-198 from the depth of 26 m. The declining trend and a great amount of background noise tell that there is too little sample in the sample chamber.

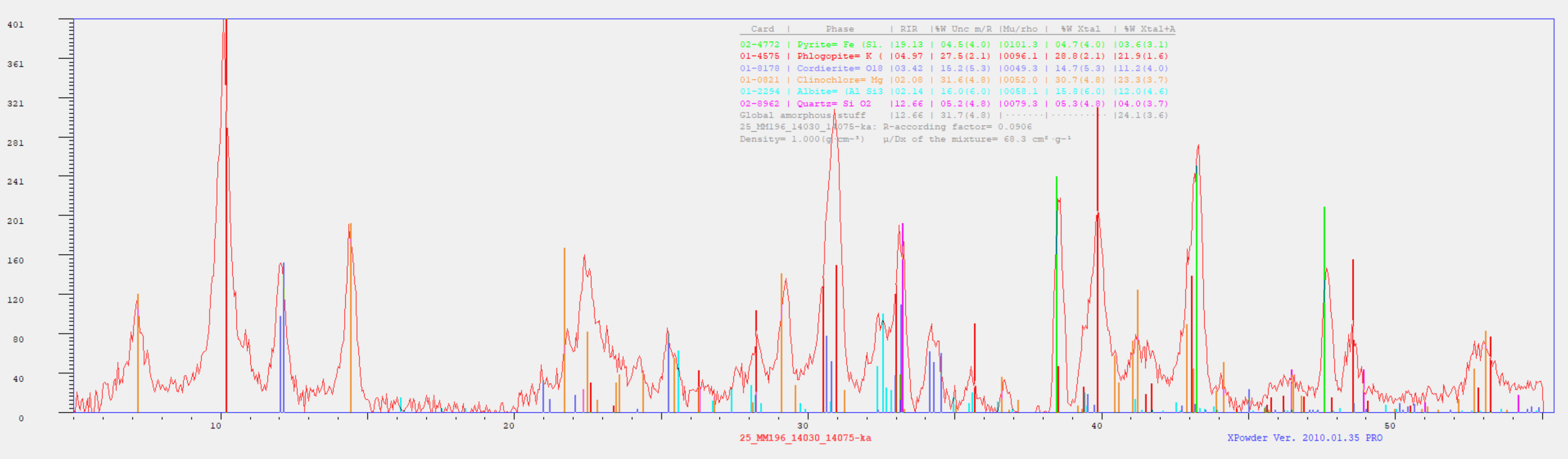

```
 Card   |      Phase       | RIR  |%W Unc m/R |Mu/rho |  %W Xtal   | %W Xtal+A
02-4772 | Pyrite= Fe (S1.  |19.13 | 04.5(4.0) |0101.3 | 04.7(4.0)  |03.6(3.1)
01-4575 | Phlogopite= K (  |04.97 | 27.5(2.1) |0096.1 | 28.8(2.1)  |21.9(1.6)
01-8178 | Cordierite= O18  |03.42 | 15.2(5.3) |0049.3 | 14.7(5.3)  |11.2(4.0)
01-0821 | Clinochlore= Mg  |02.08 | 31.6(4.8) |0052.0 | 30.7(4.8)  |23.3(3.7)
01-2294 | Albite= (Al Si3  |02.14 | 16.0(6.0) |0058.1 | 15.8(6.0)  |12.0(4.6)
02-8962 | Quartz= Si O2    |12.66 | 05.2(4.8) |0079.3 | 05.3(4.8)  |04.0(3.7)
Global amorphous stuff     |12.66 | 31.7(4.8) |·······|·········· |24.1(3.6)
25_MM196_14030_14075-ka: R-according factor= 0.0906
Density= 1.000(g·cm-³)   µ/Dx of the mixture= 68.3 cm²·g-¹
```

Figure 50. The diffractogram of the drill core MM-196 from the depth of 140 m containing pyrite.

Leväniemi et al. (2020) have reported, that the presence of galena in a sample was observed to rise the background the most. This is likely because of the fluorescence. It is well known that the fluorescence caused by the Cu anode elevates the background of the Fe-containing sulphides (Ramos Dias de Andrade et al. 2016). Even though in these measurements the Co anode was used, the background elevation effect was still observed in the case of all sulphidic minerals. Due to these effects the measurement time was adjusted to 250 exposures in the case of galena and to 150 exposures in the case of other sulphides. Even though the galena-containing samples were measured longer, a decreasing trend and plenty of background noise in the diffractogram could still be observed. Sulphides were also staining the sample holder films that might have had an effect to the peak intensity. (Leväniemi et al. 2020)

One of my initial questions regarding the applicability of the method in mineral interpretation has been the way how the device creates the random orientation to the sample to be measured. Since the sample powder is vibrated within the sample chamber, its shaking movement in the sample chamber might be a source of an erroneous diffractometer. In example, a mineral grain might get stuck between the sample films and cause an abnormal, usually sharp peak to the diffractometer (Leväniemi et al. 2020). The sample can be heterogenous, and there might happen sorting which causes the denser minerals, such as galena, pyrite, and sphalerite, to nestle to the corners of the sample chamber. Koskinen (2018) has observed such a behavior with biotite, which has a plate-like grain shape, and presumably other plate-like crystallites such as muscovite might have similar kind of behavior. It is possible to try to deal with the sorting effects with careful sample treatment procedures, such as trying to homogenize the sample by grinding it before measuring it.

To be able to do this, a great emphasis is on the careful sample preparation methods and homogenization of the sample material to avoid preferred orientation effect of plate-like minerals (Giacovazzo 1992). A large amount of amorphous material is an important factor of uncertainty affecting to the model (Billinge & Dinnebier 2008) and causes quality problems to the diffractogram (Ermrich & Opper 2011). It is an internal factor of the sample, and in a polycrystalline sample consisting of minerals with different values in the Mohs scale of hardness it might not be possible to control its amount in a reliable manner.

In addition, muscovite was one mineral that caused difficulties especially to the semiquantitative interpretation of mineral phase distribution. In some cases, if one of the diffraction patterns of muscovite was chosen to the interpretation, the relative amounts of mineral phases and the R-value of the sample were completely distorted. An example of this would be the pXRD measurement of the drill core MM-241 from the depth of 45 m (Fig. 46). The original logged lithologies represent this to be tremolite skarn (Outokumpu Oy 1961) and the SWIR data recognizes muscovitic illite and Mg-chlorite in this data point (Fig. 46). In the first diffractogram

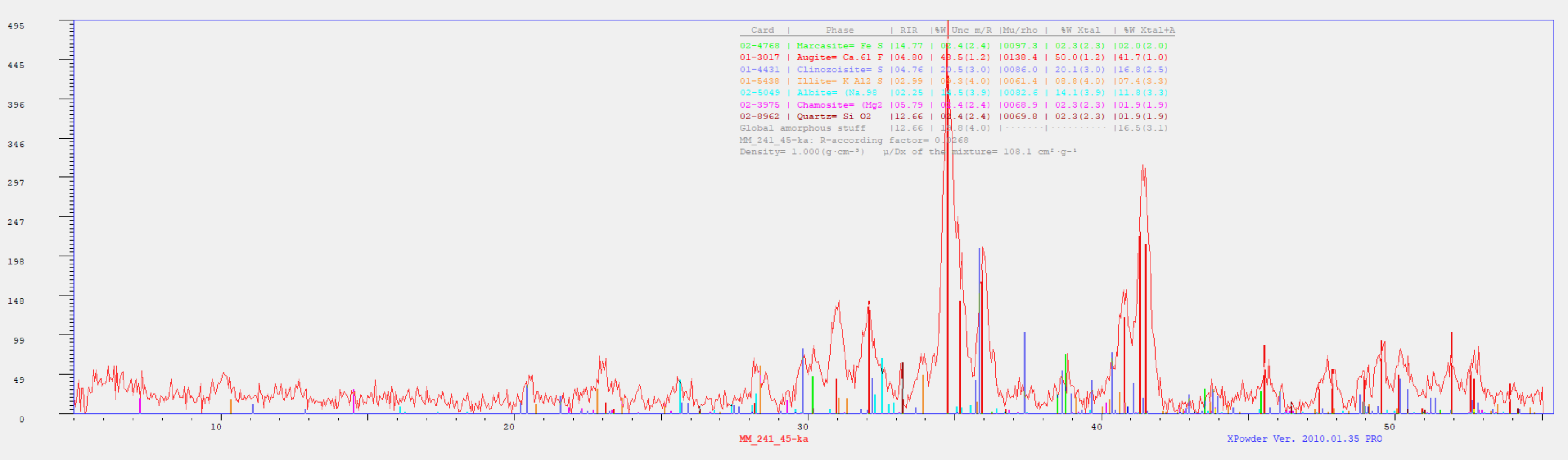

```
  Card  |       Phase        | RIR   |%W Unc m/R |Mu/rho |   %W Xtal    | %W Xtal+A
02-4768 | Marcasite= Fe S |14.77 | 02.4(2.4) |0097.3 | 02.3(2.3) |02.0(2.0)
01-3017 | Augite= Ca.61 F |04.80 | 48.5(1.2) |0138.4 | 50.0(1.2) |41.7(1.0)
01-4431 | Clinozoisite= S |04.76 | 20.5(3.0) |0086.0 | 20.1(3.0) |16.8(2.5)
01-5438 | Illite= K Al2 S |02.99 | 09.3(4.0) |0061.4 | 08.8(4.0) |07.4(3.3)
02-5049 | Albite= (Na.98  |02.25 | 14.5(3.9) |0082.6 | 14.1(3.9) |11.8(3.3)
02-3975 | Chamosite= (Mg2 |05.79 | 02.4(2.4) |0068.9 | 02.3(2.3) |01.9(1.9)
02-8962 | Quartz= Si O2   |12.66 | 02.4(2.4) |0069.8 | 02.3(2.3) |01.9(1.9)
Global amorphous stuff    |12.66 | 19.8(4.0) |·······|··········· |16.5(3.1)
MM_241_45-ka: R-according factor= 0.0268
Density= 1.000(g·cm⁻³)   µ/Dx of the mixture= 108.1 cm²·g⁻¹
```

Figure 51. The diffractogram of the drill core MM-241 from the depth of 45 m with illite included to the interpretation with the R-value = 0.0268.

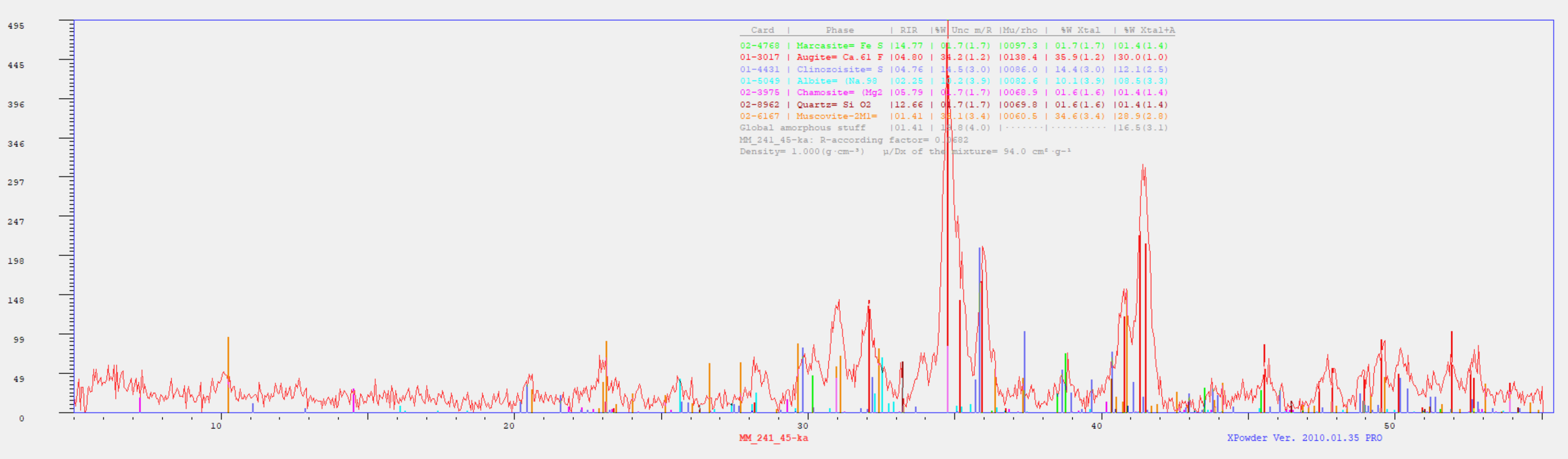

```
  Card  |       Phase        | RIR   |%W Unc m/R |Mu/rho |   %W Xtal    | %W Xtal+A
02-4768 | Marcasite= Fe S |14.77 | 01.7(1.7) |0097.3 | 01.7(1.7) |01.4(1.4)
01-3017 | Augite= Ca.61 F |04.80 | 34.2(1.2) |0138.4 | 35.9(1.2) |30.0(1.0)
01-4431 | Clinozoisite= S |04.76 | 14.5(3.0) |0086.0 | 14.4(3.0) |12.1(2.5)
01-5049 | Albite= (Na.98  |02.25 | 10.2(3.9) |0082.6 | 10.1(3.9) |08.5(3.3)
02-3975 | Chamosite= (Mg2 |05.79 | 01.7(1.7) |0068.9 | 01.6(1.6) |01.4(1.4)
02-8962 | Quartz= Si O2   |12.66 | 01.7(1.7) |0069.8 | 01.6(1.6) |01.4(1.4)
02-6167 | Muscovite-2M1=  |01.41 | 38.1(3.4) |0060.5 | 34.6(3.4) |28.9(2.8)
Global amorphous stuff    |01.41 | 19.8(4.0) |·······|··········· |16.5(3.1)
MM_241_45-ka: R-according factor= 0.0682
Density= 1.000(g·cm⁻³)   µ/Dx of the mixture= 94.0 cm²·g⁻¹
```

Figure 52. The diffractogram of the drill core MM-241 from the depth of 45 m with muscovite included to the interpretation with the R-value = 0.0682.

(Fig. 51) the diffraction pattern of illite was chosen instead of muscovite to the interpretation. This produced the R-value of 0.0268. The relative amount of illite in the sample was calculated to be 7.4 wt %.

When the diffraction pattern of muscovite was included to the interpretation (Fig. 52), the calculated R-value was 0.0682, which was over two times worse than in the interpretation made with illite. In addition, the relative amount of muscovite was calculated to be 28.9 wt%, which is almost as much as the main phase of the sample, augite, with a proportion of 30 wt% in this measurement. The proportion of muscovite does not seem to be well justified since augite has very distinctive diffraction peaks in the diffractogram by their intensity, while the diffraction pattern of muscovite inundates more to the background, overlaps with other diffraction patterns, and does not even fit that well to the diffractogram by its peak locations and intensities. On the contrary, the diffraction pattern of illite (Fig. 51) is more in harmony with the diffractogram despite its lower intensities.

These problems related to muscovite are probably appearing due to the tendency of the plate-like muscovite for a preferred orientation (Rietveld 1969) or because of the packing of the flat crystals to the corners of the sample holder as reported by Koskinen (2018). This problem was usually solved by choosing another diffraction pattern to the interpretation. One option would have been to leave this diffraction pattern completely away from the interpretation: however, it might contort the whole interpretation.

XPowder quantified relatively reasonable quantities of amorphous material from the studied samples with an average of all samples of 13.1 wt % (Appendix 5). However, in the samples where the amount of amorphous material rises to 20 wt% and above, the reliability of the data might begin to be questionable. This is because X-ray diffraction as a method is not directly applicable on the characterization of amorphous materials (Billinge & Dinnebier 2008).

Due to the software-related and methodological limitations, it is also important to point out that the estimated amount of amorphous material in the samples quantified with XPowder is merely a rough estimate (Martin 2008). In addition, due to background noise in the pXRD caused by relatively short measurement times, it is not possible to interpret all the peaks in a diffractogram since there is no certainty whether the peaks in the diffractogram would be actual mineral phases, or just background noise. Therefore, these measurements stay far behind of the precision of the measurements made with the laboratory XRD. In addition, since in this study it has not been tested with comparisons to measurements made in laboratory conditions with more precise instruments, known compositions and internal controls, it cannot be asserted that this calculated amount would be even near to correct.

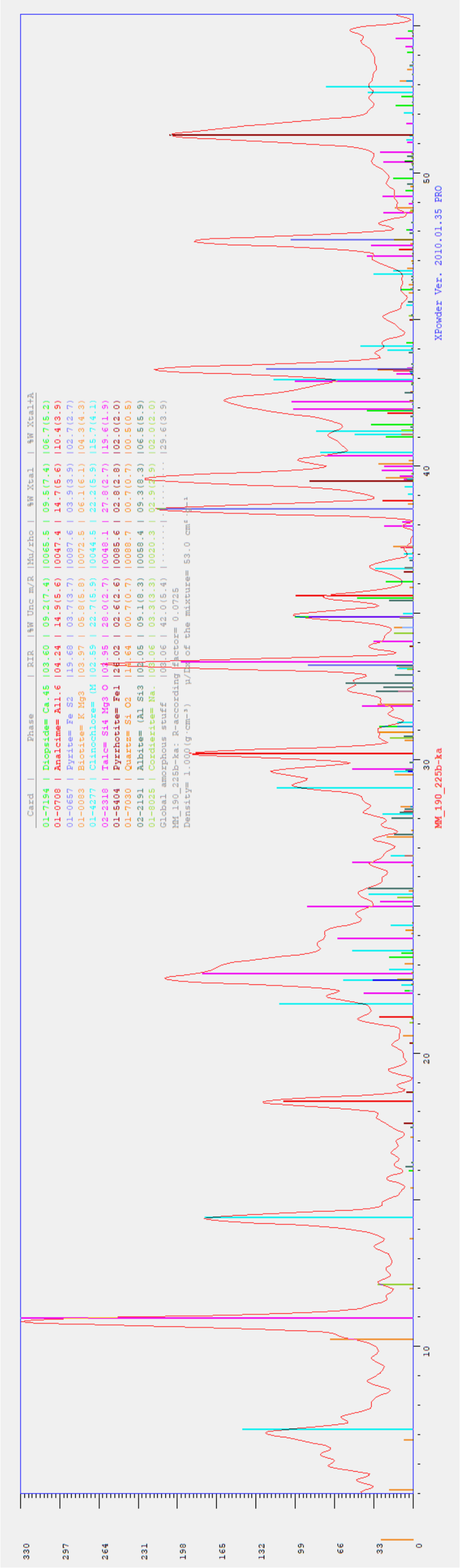

```
Card     | Phase                | RIR   |%W Unc m/R |Mu/rho  | %W Xtal   | %W Xtal+A
01-7194  | Diopside= Ca.45      |03.60  | 09.2(7.4) |0065.5  | 09.5(7.4) |06.7(5.2)
01-0708  | Analcime= Al1.6      |04.24  | 14.9(5.6) |0047.4  | 14.7(5.6) |10.4(3.9)
01-0657  | Pyrite= Fe S2        |19.68  | 03.7(3.7) |0087.6  | 03.9(3.9) |02.7(2.7)
01-0083  | Biotite= K Mg3       |03.97  | 05.8(5.8) |0072.5  | 06.1(6.1) |04.3(4.3)
01-4277  | Clinochlore= (M      |02.59  | 22.7(5.9) |0044.5  | 22.2(5.9) |15.7(4.1)
02-2318  | Talc= Si4 Mg3 O      |04.95  | 28.0(2.7) |0048.1  | 27.8(2.7) |19.6(1.9)
01-5404  | Pyrrhotite= Fe1      |28.02  | 02.6(2.6) |0085.6  | 02.8(2.8) |02.0(2.0)
01-7030  | Quartz= Si O2        |14.64  | 00.7(0.7) |0088.7  | 00.7(0.7) |00.5(0.5)
02-2191  | Albite= (Al Si3      |02.05  | 09.1(8.3) |0058.4  | 09.3(8.3) |06.5(5.9)
01-8025  | Cordierite= Na.      |03.06  | 03.3(3.3) |0020.3  | 02.9(2.9) |02.0(2.0)
Global amorphous stuff          |03.06  | 42.0(5.4) |........|...........|29.6(3.9)
MM_190_225b-ka: R-according factor= 0.0725
Density= 1.000(g·cm⁻³)    µ/Dx of the mixture= 53.0 cm²·g⁻¹
```

Figure 53. The diffractogram of the drill core MM-190 from the depth of 225 metres. Fourier smoothing has been applied to the diffractogram.

However, regarding the amorphous material in this dataset, five samples in the drill core MM-190 (depths of 45, 115, 155, 225 and 235 m), one sample in the drill core MM-196 (depth of 140 m), two samples in the drill core MM-198 (depths of 4 and 14 m) and one sample in the drill core MM-241 (depth of 85 m) have >20 wt% of amorphous material according to XPowder. The data obtained from these data points should be interpreted with extra precision. My conjecture regarding these data points is that in reality the amount of amorphous material is possibly not so high in these samples, but the samples have remained too coarse. According to the observations of Snellings (2014), grinding of the material into very fine particle size reduced the quantified amount of amorphous material in the sample. Therefore, extra caution is required with these quantifications of amorphous matter since they might be tightly connected to the sample preparation procedures.

To test this hypothesis, the diffractogram of the drill core MM-190 from the depth of 225 m (Fig. 53) was taken under observation. XPowder has calculated the amount of amorphous matter to be as high as 28.2 wt% in the sample. In this sample following minerals were identified: talc (19.7 wt%), clinochlore (15.2 wt%), analcime (10.2 wt%) albite (7.4 wt%), diopside (7.2 wt%), biotite (4.7 wt%), pyrite (2.7 wt%), cordierite (2 wt%), pyrrhotite (1.9 wt%) and quartz (0.8 wt%).

Since sulphidic minerals, especially pyrite and galena, have caused quality difficulties to the diffractograms, the diffraction pattern of pyrite was chosen to be observed first. During the measurement the energy resolution was 0.25° 2θ FWHM (true FWHM) and X-ray wavelength of the Co $K\alpha_1$ 1.78897. The $K\alpha_1$ peak of pyrite had a location of 36.5 (2θ). The calculated grain size of a crystal derived using the corrected Scherrer formula (Equation 10) would be 43 nm.

Talc is the most abundant mineral present in the drill core MM-190 from the depth of 225 m. However, its hardness on Mohs scale is 1 meaning it is very soft. Therefore, it is likely that it probably has not stayed too coarse in the sample. The calculated grain size of talc in the sample using its $K\alpha_1$ peak at a location of 10.85 (2θ) with the true FWHM being 0.325° 2θ FWHM is 32 nm. In comparison, the calculated grain size of clinochlore using its $K\alpha_1$ peak at a location of 7.10 (2θ) is 10 nm.

As a conclusion, certainly there is variation in the particle size of the sample. However, the particles in the sample seem to be preferably in a nano-size scale than in too large particles. In this case it can be deduced that the high amount of amorphous matter in this sample could be true and causes the wide bumps to the diffractogram (Ermrich & Opper 2011). Also, the nanocrystalline material in the sample influences the diffractogram quality and widens the peak profiles.

The interpretation software used in this study was XPowder, which posed its own additional challenges due to usability issues. The reference database used in this study was AMCSD, and during the interpretation its use turned out to be arduous. When the XPowder was calculating suggestions of possible mineral phases present in the sample, it gave a lengthy list of the phases that would have somehow matching diffraction pattern with the diffractogram. Typically, this list would have consisted of around 1500 diffraction patterns that could have at least theoretically matched with the diffraction patterns. It would be very time-consuming to go through all these possible patterns, and many of them were matching from one part to the diffractogram profile but from most of the parts they were not matching.

Within these diffraction patterns there were all kinds of chemical formulas in addition to phases with accepted mineral names, such as quartz, and phases with non-accepted mineral names, such as hypersthene. In example, the database includes not only albite and anorthite endmembers of the plagioclase series, but also all the members in between such as oligoclase and labradorite. The problem with these names is that they are not accepted mineral names such as albite and anorthite would be. In addition, it is not possible to identify reliably the composition of plagioclase with XRD. It is possible only to identify if the diffraction patterns of albite or anorthite would be a better fit for the diffractogram of the sample.

Since both the interpretation software and the used database produced some issues in the interpretation, there was a great emphasis on the interpretation done by a human. Therefore, human errata in interpretation could not be avoided entirely. When both knowledge and experience of the method were accumulated during the study, more details could have been noticed and interpreted. However, as in example Koskinen (2018) has already represented, it cannot be excluded that other person might have interpreted some of the samples in a different manner.

One important factor to note is that the percentages obtained from the interpretation software, such as XPowder or Diffrac.Eva, are not reliable (Sarala & Koskinen 2018). The unreliability is usually related to the amount of amorphous material in the sample (Billinge & Dinnebier 2008), and the interpretation software might either exaggerate or underestimate the amount of the amorphous material depending on what kind of mathematical basis their calculations is based on. To produce more reliable quantitative models of the diffractograms, the Rietveld method would be suggested: however, to produce a reliable model, all the mineral phases of the sample must be interpreted as carefully as possible.

It is possible to try to improve the diffraction data quality with different methods such as applying Fourier transform smoothing to the diffractograms (Martin 2008), but this leads to further questions like would post-processing of the actual diffraction data in fact interrupt the actual interpretation or even make it impossible by distorting the information. It was also observed that this kind of post-processing of the data has an effect of the relative quantities quantified by XPowder, as can be seen in Figures 54-55. Without any smoothing of the curve the amount of dolomite would be 35.7 wt%, and after the Fourier smoothing the amount of dolomite is quantified to be 38.8 wt%. After all, within the diffractogram there is plenty of subtle information concealed to the peak intensities, shapes, and locations (Billinge & Dinnebier 2008), and smoothing the diffractograms might fade out or even corrupt this information.

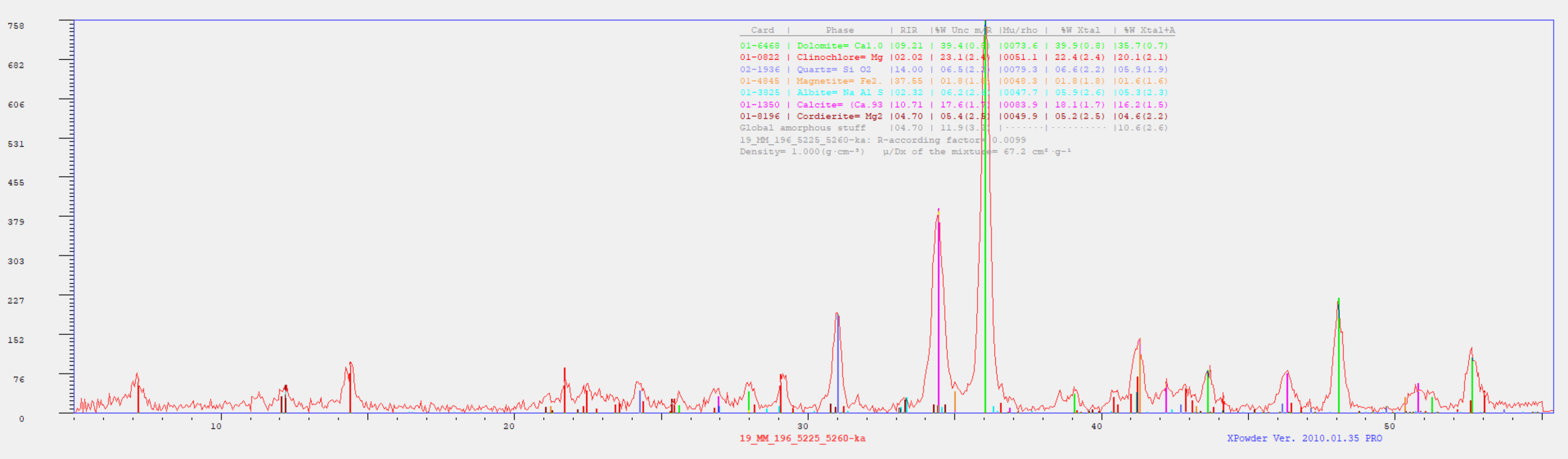

```
 Card  |        Phase       | RIR  |%W Unc m/R |Mu/rho |  %W Xtal   | %W Xtal+A
01-6468 | Dolomite= Ca1.0 |09.21 | 39.4(0.8) |0073.6 | 39.9(0.8) |35.7(0.7)
01-0822 | Clinochlore= Mg |02.02 | 23.1(2.4) |0051.1 | 22.4(2.4) |20.1(2.1)
02-1936 | Quartz= Si O2   |14.00 | 06.5(2.2) |0079.3 | 06.6(2.2) |05.9(1.9)
01-4845 | Magnetite= Fe2. |37.55 | 01.8(1.8) |0048.3 | 01.8(1.8) |01.6(1.6)
01-3825 | Albite= Na Al S |02.32 | 06.2(2.6) |0047.7 | 05.9(2.6) |05.3(2.3)
01-1350 | Calcite= (Ca.93 |10.71 | 17.6(1.7) |0083.9 | 18.1(1.7) |16.2(1.5)
01-8196 | Cordierite= Mg2 |04.70 | 05.4(2.5) |0049.9 | 05.2(2.5) |04.6(2.2)
Global amorphous stuff    |04.70 | 11.9(3.2) |·······|·········· |10.6(2.6)
19_MM_196_5225_5260-ka: R-according factor= 0.0099
Density= 1.000(g·cm-³)   µ/Dx of the mixture= 67.2 cm²·g-¹
```

Figure 54. The diffractogram of the drill core MM-196 from the depth of 52 metres without smoothing.

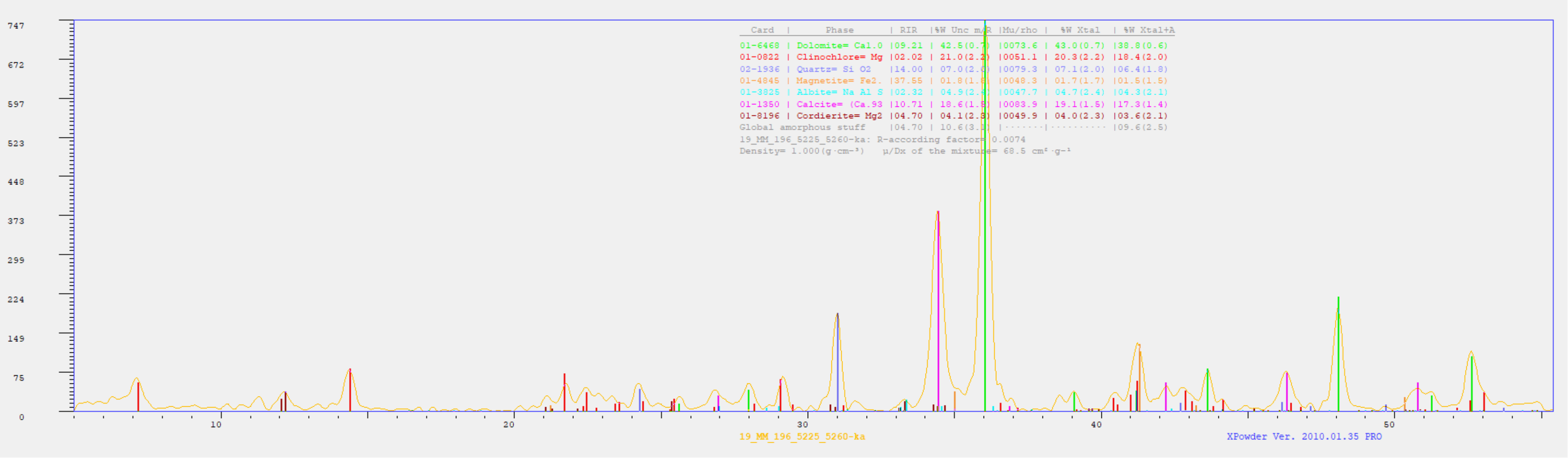

```
 Card  |        Phase       | RIR  |%W Unc m/R |Mu/rho |  %W Xtal   | %W Xtal+A
01-6468 | Dolomite= Ca1.0 |09.21 | 42.5(0.7) |0073.6 | 43.0(0.7) |38.8(0.6)
01-0822 | Clinochlore= Mg |02.02 | 21.0(2.2) |0051.1 | 20.3(2.2) |18.4(2.0)
02-1936 | Quartz= Si O2   |14.00 | 07.0(2.0) |0079.3 | 07.1(2.0) |06.4(1.8)
01-4845 | Magnetite= Fe2. |37.55 | 01.8(1.8) |0048.3 | 01.7(1.7) |01.5(1.5)
01-3825 | Albite= Na Al S |02.32 | 04.9(2.4) |0047.7 | 04.7(2.4) |04.3(2.1)
01-1350 | Calcite= (Ca.93 |10.71 | 18.6(1.5) |0083.9 | 19.1(1.5) |17.3(1.4)
01-8196 | Cordierite= Mg2 |04.70 | 04.1(2.3) |0049.9 | 04.0(2.3) |03.6(2.1)
Global amorphous stuff    |04.70 | 10.6(3.1) |·······|·········· |09.6(2.5)
19_MM_196_5225_5260-ka: R-according factor= 0.0074
Density= 1.000(g·cm-³)   µ/Dx of the mixture= 68.5 cm²·g-¹
```

Figure 55. The diffractogram of the drill core MM-196 from the depth of 52 metres after the Fourier smoothing.

8.1.2 Sources of error of the imaging spectroscopy

Possible sources of error related to the imaging spectroscopy include the data acquisition method (Humbo 2019), limitations of the used wavelengths, varying grain size (Zaini et al. 2012), and alteration (McCanta & Dyar 2020) and weathering (Ehara Suryantini 2005) of minerals. Instrumental limitations include spectral range, spectral bandwidth, spectral sampling, and signal-to-noise ratio (S/N) (Clark 1999).

Some methodological limitations include a risk to misinterpretation. In this study the VNIR and the SWIR wavelengths were used, so the spectral range would be 350-2500 nm. However, this wavelength area does not cover most of the silicate minerals such as quartz, feldspars, and garnet (Booysen 2021a) and has limited possibilities to detect the absorption features of pyroxenes and olivine (Clark 1999). Since only certain wavelength areas are measured, there are also plenty of empty measurements (Leväniemi et al. 2020). In these cases, there is a risk to misinterpret the measurement in such a way that there is not “anything” relevant in the measured area. Even if the measurement tells the result to be “null” or “aspectral”, this probably is not the case since there are plenty of other mineral phases that might exist in the sample, but they are not visible either in the VNIR or the SWIR spectra. This might also lead to another misinterpretation that spectral methods are not suitable for mineral identification, although the problem would have been in the data collection method itself with too concise spectral range.

Narrow spectral range produces other possible sources of error. In principle, the spectral continuum which is the absorption intensity relative to the background of a mineral would be a function of its abundance and the absorption coefficient (Hunt & Ashley 1979; Clark & Roush 1984). However, regarding the relative “amounts” of mineral phases given by TSG it is even more crucial to understand that these amounts do not describe the actual amounts of mineral phases in the sample at all. They only describe the proportion of that phase among the identified phases. If the method is not able to identify all the rock-forming mineral phases, then they naturally stay out of the interpretation. This can be seen very clearly in example from Figure 30, and it also warns that using only the SWIR data might give a false image that it would be the only mineral phase present in the sample even though this is not true.

Alteration of a mineral in example by oxidation (McCanta & Dyar 2020) or weathering (Ehara Suryantini et al. 2005) can influence the spectral features. According to some sources olivine and pyroxene would be possible to detect within the VNIR wavelength (Clark 1999, Booysen 2021a). Even though olivine has its first diagnostic absorption features related to the Fe^{2+} crystal field transitions within the VNIR wavelength range (Isaacson et al. 2014), many of its characteristic absorption features are visible within the LWIR wavelength (Clark 1999). The same applies to pyroxene (Clark 1999). In addition, in Finnish bedrock pure olivine with a formula of $[(Mg,Fe)_2SiO_4]$

is not abundant and is predominantly altered, and the VNIR reflectance features might also be altered due to the substitution of minor cations such as Ni^{2+} or Cr^{2+} (Isaacson et al. 2014). The spectral features of pyroxenes can be also affected by oxidation due to metamorphosis (McCanta & Dyar 2020). Therefore, using as wide spectral range as possible for the identification of mineral phases would be important. In this dataset it is possible that some of the spectral features that were initially identified as aspectral were actually slightly differing or displaced due to varying grain size, alteration, or weathering.

The drawback side of the ASD data acquisition method (which is the point measurement) is that it does not give accurate estimates of the mineral compositions of the sample (Humbo 2019). The whole drill core is not included to the analysis: only the area that stays within the measurement window is included. Since the analyses have been taken using 1 m interval, they do not fully represent the drill core. In addition, if the sample does not entirely cover the measurement window of a point spectrometer, some visible light will also be seen in the spectra (Leväniemi et al. 2020). In this dataset this error is systematic and seen in all spectra measured.

Concise reference libraries also include their own risks. Mineral phases might be left unidentified if they are not included to the reference library. The less classes in the library, the less degrees of freedom (Berman et al. 2011). In example, TSG identifies three different kaolinite phases recorded in its reference library, but it does not recognize halloysite, another water-bearing mineral that has its diagnostic absorption feature in 2200 nm (Clark 1999) which is the same place than kaolinite would have. Therefore, the automatic interpretation of kaolinite made by TSG should be double-checked and compared to the very similarly looking absorption feature of halloysite.

When compared to the pXRD data, the limitations of the SWIR data are remarkable (Figs. 30, 36, 41, and 46). The pXRD can show those rock-forming minerals that are not visible within the SWIR wavelength, such as quartz, feldspar, and cordierite. There is much more mineralogical variation visible in the pXRD data than in the SWIR data. However, considering the limitations of the SWIR spectroscopy, these observations were expected.

Measurement quality is one thing to consider in the interpretation. In Figure 56 the error values of the SWIR data are represented graphically. The quality data of the VNIR measurements are included to the diagrams of the drill core MM-190 and MM-198. The quality data of the VNIR measurements were not included to the diagrams of other drill cores due to lack of interpreted minerals with VNIR wavelength. If the error value is <1000, the data are still reliable. The data represent that the SWIR data of the drill core MM-190 are of poor quality in many data points, and there are problems with the data quality in a few data points of the VNIR data. Most of the quality problems appear within 150-200 m depth which would be the area before and within the ore zone.

Other drill cores have also some quality problems with the SWIR data. The drill core MM-198 does not seem to have significant quality problems with the VNIR data.

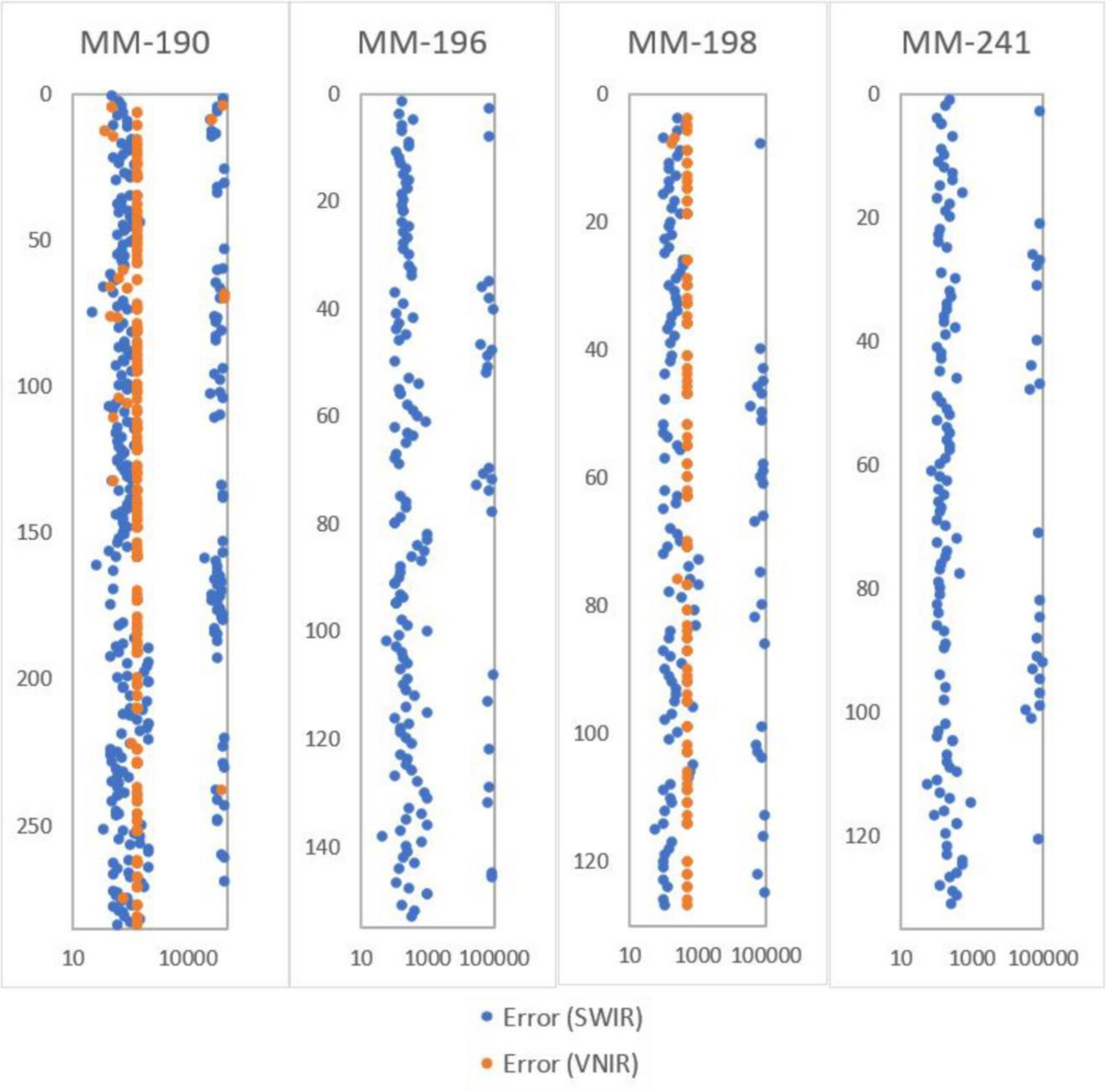

Figure 56. Measurement quality of the short-wave infrared (SWIR) and the visible, near-infrared (VNIR) measurements according to The Spectral Geologist. On the vertical scale there is the depth (m) and on the horizontal scale there is the error value represented on a logarithmic scale. The measurement quality data of the VNIR data are only included to the drill cores MM-190 and MM-198 since in the drill core MM-196 there were no identified minerals within the VNIR wavelength region and in the drill core MM-241 only one mineral phase was identified within the VNIR wavelength region.

According to the data presented in Figure 56, it seems that there is a correlation between the appearance of sulphidic minerals and erroneous SWIR measurements. It is hard to determine precisely what would cause these errata, but one conjecture would be the alteration of the sulphidic minerals by oxidation. This process would have started after the drilling in the end of 1940s-beginning of the 1950s when the sulphidic minerals have been exposed to oxygen after the drilling and in the long-term storage conditions. Another guess of the causes of the errata could be some amount of surface moisture on the samples, which could be due to humid storage conditions.

One possibility could be also related to the instrumental features, such as the narrow spectral bandwidth would limit the capability of a spectrometer to measure the absorption features. Another possibility is related to the signal-to-noise ratio which would describe the ability of the spectrometer to measure precisely. It is not only dependent on the sensitivity of the detector or the spectral bandwidth, but also on how strongly the light is reflected or emitted from the material under the measurement. (Clark 1999) It is only a guess, but perhaps shiny, reflecting surfaces of sulphidic minerals could cause disturbances to the S/N ratio.

8.2 Alterations of the drill cores MM-190, MM-196, MM-198, and MM-241

In all four drill cores the chloritic alteration can be seen strong almost throughout all the cores in the SWIR data (Figs. 31, 37, 42 and 47) and the pXRD data (Figs. 30, 36, 41, and 46) as abundant chlorite-group minerals, white micas, and quartz. The proportion of Mg-chlorite is growing around the ore minerals. Its appearance is usually connected to the skarn units, and probably to the Mg-Fe-metasomatism. In the drill cores MM-190 and MM-196 the appearance of Mg-chlorite is also connected to montmorillonite. Considering the ways to trace the ore within this deposit, this seems to be the most important ore vector that can be derived from the SWIR data, at least in the case of these four drill cores.

On the contrary, in all the drill cores, the pXRD data (Figs. 30, 36, 41 and 46) show very little variation in the chlorite group mineral composition: most of the identified chlorite group phases would be clinochlore and only few observations were made of chamosite. The reason for this is probably that in AMCSD database there are only few diffraction patterns available for chamosite, but tens of different diffraction patterns for clinochlore. Therefore, it might be usually easier to find a matching diffraction pattern within the clinochlore patterns than the chamosite patterns. However, it can be clearly seen from both datasets that there is a great emphasis on the presence of chlorite-group minerals in these drill cores.

Similar kind of observations apply to the variation of amphiboles identified by TSG. TSG recognizes mostly hornblende from the SWIR data when the pXRD has identified more different amphiboles (Figs. 30, 36, 41, and 46) which describe that there is chemical and structural variety within this mineral group amongst these samples. The pXRD identifies in example actinolite, which could be a pseudomorph of the clinopyroxene (Jones et al. 2005). These differences are probably once again due to the limited mineral library of TSG. However, both pXRD and SWIR data reveal that the sequences logged as “amphibolites” are not mineralogically straightforward, and there is much more mineralogical variation in all the drill cores.

The AlOH absorption features from the drill cores MM-190 (Fig. 33), MM-196 (Fig. 38), MM-198 (Fig. 43) and MM-241 (Fig. 48) show a continuous wavelength range from 2195 to 2230 nm. It reflects the compositional variation of white mica from sodic or paragonitic (high octahedral Al; <2200 nm) to potassic, intermediate, and muscovitic compositions (2200-2210 nm), and eventually to phengitic (low octahedral; >2210 nm) compositions (Herrmann et al. 2001). In this dataset it is hard to point out a clear connection of the white mica and the appearance of the sulphidic minerals. There are some hints in the drill cores MM-198 (Fig. 43) and MM-241 (Fig. 48) that the phengitic composition of white mica would be connected to the appearance of the sulphidic minerals. In general, probably the differing compositions of white mica reflect the complexity of the hydrothermal alteration within these drill cores. In example, acidity oh hydrothermal fluids could have been the factor that has pushed the equilibrium of the white mica to muscovitic composition.

Pinitization and eventually a complete breakdown of cordierite was observed in the drill cores MM-196, MM-198 and MM-241. In the pinitization the cordierite would first alter to chlorite, muscovite, and quartz or aluminium silicate (like cyanite, andalusite and sillimanite), and then it would break down to chlorite, aluminium silicate or pyrophyllite, and quartz together with sericitization occurring at the same time. Some other phases can also form in smaller extent, like iron oxides or paragonite. (Ogiermann & Kalt 2000)

The appearance of a smectite-group mineral, such as montmorillonite or vermiculite, together with white mica and illite would refer to argillic alteration of unmetamorphosed deposits (Table 3). In these drill cores, montmorillonite tends to appear with siderite, different chlorite-group minerals, and talc. However, there are some hints of this type of alteration, in example in the drill core MM-196 in 98 m there is illite and muscovite together with quartz, cordierite, albite, clinochlore, and pyrite in the pXRD data (Fig. 36). In the same drill core in 101 m in the pXRD data there is an assemblage of phengite and vermiculite together with albite, quartz, cordierite, clinochlore, and some pyrite and pyrrhotite. These assemblages refer to the before mentioned pinitization of cordierite, but also both to the sericitic and chloritic alteration of the greenschist and granulite facies. This describes here that the alterations here are diverse and show a gradual development.

According to the pXRD data (Fig. 36), there was only one observation of andalusite in the drill core MM-196 in 87 m hosted by the cordierite gneiss sequence accompanied by quartz, cordierite, and albite. In this data point the SWIR data (Fig. 37) shows to be aspectral, but after this measurement point there is a short zone of Mg-chlorite combined first with illite, then muscovite, and then with Fe-containing tourmaline. Right before it there is some kaolinite and Mg-chlorite. Before and after this area there are logged observations of sulphidic minerals in 75.25-77.82 m, 80.10-82.20 m, 95.20-96.83 m, and 99.70-101.45 m. The observation of andalusite is interesting since it would point to the advanced argillic alteration of greenschist facies (Shanks 2012). The unfortunate thing here is that due to missing data in this data point it is not possible to confirm with the SWIR data other diagnostic alteration minerals of this alteration zone, such as kaolinite. However, there is indeed an observation of kaolinite slightly before the observed location of andalusite (Fig. 37).

There are some observations of carbonate propylitic alteration of unmetamorphosed deposits in example in the drill core MM-198 in the depth 14 m with an assemblage of calcite, albite, clinochlore, and epidote with some quartz, hedenbergite, cordierite, and montmorillonite (Fig.41). This assemblage is relatively heterogenous and describes the complexity of these lithologies. In the drill core MM-190 in 175 m there is an assemblage of calcite, grossular garnet, albite, actinolite, and clinochlore according to the pXRD data (Fig. 30) referring to carbonate propylitic alteration of both greenschist facies and granulite facies. The amphibole phase here is identified as hornblende by the SWIR spectroscopy.

Iron-bearing mineral phases in the site include naturally the sulphides: pyrite, pyrrhotite, and marcasite. Iron also seems to appear at least bound to siderite, which is an iron (II) carbonate ($FeCO_3$) visible in the SWIR data. In the SWIR data of the drill core MM-190 (Fig. 31) another observation is that siderite tends to appear together with montmorillonite and in other drill cores it occurs more often with muscovite. The observations of siderite are spot-like, and it can be assumed that it occurs as a disseminated mineral.

Ratsula (2016) has described the hydrothermal alteration in Orijärvi area, and according to his observations the alteration has reduced the Ca, Na, and As contents in all the altered rocks while Mg and F have been enriched into them. Al, Fe and P contents on the contrary did not show significant differences between altered and non-altered rocks. Leväniemi and Hokka (2021) suggest that in Metsämonttu the increased Fe_2O_3 and MgO contents refer to Mg-Fe alteration. In these four drill cores (Figs. 28, 33, 38 and 43) the increased Fe_2O_3 and MgO contents are connected primarily to the skarn units. According to the observations of Ratsula (2016), the higher Mg content is possibly due to the precipitation of Mg transported by hydrothermal fluids.

According to Latvalahti (1979), Mg-Fe-metasomatism would be described with the gain of MgO, FeO, Al_2O_3, and TiO_2 as elements, and with the loss of SiO_2 and Na_2O elements. However, according to the contemporary knowledge this usually does not apply to TiO_2 which would be one of the most stable elements. In addition, Mäkelä (1989) has described TiO_2 to be the most stable chemical component with Al_2O_3, which makes the distinctive TiO_2 anomaly in the drill core MM-190 is particularly interesting. The logged lithologies do not shed light on these anomalies since this sequence is defined to be relatively intact and stiff amphibolite. It is possible that there is some disseminated arsenopyrite since there are some other individual spots of arsenopyrite within these drill cores.

Rapid changes of CaO contents are also observed in these drill cores. However, according to Mäkelä (1989) the changes in CaO contents cannot be used as a reliable alteration indicator in Metsämonttu since there is plenty of variation within wide range, and even within the same lithological unit. while Na and Ca contents have probably been diluted from the protoliths to the fluids. In these drill cores the increased CaO is primarily related to the limestone and skarn units. The singular peaks of Cr and Ni in the beginning of each drill core do not seem to be logically connected to any lithological units, neither mineralogical, petrophysical, nor other geochemical data. However, according to Mäkelä (1989), Cr and Ni are amongst the most immobile elements in Metsämonttu, Aijala, Iilijärvi and Tupala. Latvalahti (1979) suggests, that silicification could be seen as the rise of SiO_2 content, and the depletion of all other elements. Within these four drill cores there is no area that would completely fill these criteria of the silicification.

8.3 Suitability for mineral exploration

Certainly, both the pXRD and the SWIR spectroscopy can be used together to form a tool for mineralogical and alteration drill core logging, and they fulfill the mineralogical data gaps caused by the limitations of both methods. However, it is questionable if using two relatively limited methods instead of one powerful and reliable method could be considered time-wise fast or reasonable. Application of both methods in the mineral identification would assuredly strongly benefit of some re-evaluation of the used methods and method development with a strong emphasis on reliable and effective algorithm-based automated mineral identification solutions.

One thing that defends the use of pXRD and imaging spectroscopy in data acquisition for mineral exploration is their objectivity as methods. Drill core logging by visual observation is always subjective and might lead to contradictory interpretations and discordant use of terminology. Portable devices are also easy to take to the site, and they can provide objective in-situ data of the destination (Lemière & Uvarova 2020; Uvarova et al. 2020). However, it is good to keep in mind that this kind of data are at its best in a more rough, directional scale.

Regarding the field conditions, ideally the workflow would be such that measurements could take place on-site and provide fast, sufficiently good, and reliable information of the target so that this information could be used for further planning of the field activities within rough timetables (Lemière & Uvarova 2020). This would require minimal on-site data processing done by humans, and here the role of a functional and reliable software for the data processing grows. Future perspectives of the automated mineral identification certainly include algorithm-based approaches for the data processing, such as SwiftMin® (Uvarova et al. 2020), or mineral identification scanners using imaging spectroscopy technology for logging time-efficiently whole boxes of drill cores. There are handheld mineral identifiers using LWIR, that can possibly be used alongside with VNIR and SWIR measurements, and that would allow this methodology to be used in field conditions as well.

8.3.1 The portable X-ray diffraction in the mineral exploration

The pXRD is a portable device that is suitable for field-working conditions (Blake et al. 2012; Burkett et al. 2015). It does not include moving parts except the sample holder that vibrates the sample during the measurement (Olympus 2020). It can identify major mineral phases, and it does not require much of the sample material (Koskinen 2018; Sarala et al. 2019). In theory, the sample does not need complicated sample treatment procedures before the measurement (Sarrazin et al. 2005; Sarala & Koskinen 2018).

However, the pXRD seems to be problematic with accessory minerals due to its accuracy problems (Koskinen 2018). The angular resolution of the pXRD is 5-55° versus 2-120° of the laboratory XRD. The limited angular resolution is likely to cause problems with those phases which would fall out of the range, and these phases might not become visible in the pXRD diffractograms. (Sarala et al. 2019) Additionally, the sulphidic minerals, especially galena (Leväniemi et al. 2020) and the plate-like crystallites such as muscovite (Figs. 51-52) and biotite (Koskinen 2018) might cause quality problems to the diffractograms such as rising of the background and high background noise. The pXRD is also not suitable for the identification of metamictic minerals, such as zircon and allanite due to their distorted or destroyed crystal structure (Lima de Faria 1964; Sarala & Koskinen 2018; Sarala et al. 2019) since XRD is a method meant to define well crystalline materials (e.g., Will 2006).

The quality of the pXRD diffraction data is varying and poses serious difficulties to the interpretation. According to the experience obtained from this method development project, the data collected with the pXRD does not have good enough quality for quantitative modelling of the XRD data. There are significant problems related to the insufficient sample preparation procedures that have a strong effect on the quality of powder diffraction data, including sorting of the material and preferred orientation effect, that are not compensated with the measurement technology of the pXRD well enough. The most severe quality problems occurred with the plate-like crystallites, in this data mainly muscovite (Figs. 51-52), and the sulphidic minerals (Fig. 50).

The diffraction data measured with the pXRD includes plenty of background noise (in example in Fig. 49) which makes the data reliability questionable since it is very difficult to distinguish if all the peaks visible in the diffractogram are actual peaks or just background noise. Certainly, the data with this quality cannot be used for reliable quantitative modelling, such as Rietveld, since all the mineral phases of the sample need to be identified, meaning, each peak of the diffractogram needs to be interpreted. The data quality is partially due to short measuring times and the limited angular resolution. Increasing the measuring time, it might be possible to improve the diffractogram quality (Koskinen 2018; Sarala et al. 2019), but this also depends on the sample consistency and does not overcome with the limitations of the concise angular resolution. Due to these problems, it is also debatable if the method could actually be a fast and easy-to-use one, since the interpretation of the diffractograms can be time-consuming and requires some expertise of the topic. To improve the data quality of the pXRD it would be recommended to use longer measurement times and careful sample preparation methods.

Regarding the pXRD, there is a great emphasis on the choice of the interpretation software and the mineralogical database it uses. Easy-to-use and ductile user interface with an up-to-date mineralogical database would improve the usability, time consumption and eventually the data quality. To produce reliable phase interpretation results, there must be a possibility to compare the data quality of the diffraction patterns used in comparison. It would be suggested to use a database that is restricted only to approved mineral phases and names with a possibility to compare the data quality, such as PDF-4/Minerals by ICDD.

8.3.2 Imaging spectroscopy in the mineral exploration

The SWIR spectroscopy can effectively detect the presence of white mica and dark mica in the sample, and it can identify well clay minerals, which would be a challenge in the pXRD and the laboratory XRD. Minerals identified with the SWIR spectroscopy show a variation in mineral chemistry as well, in example in chlorite group phases, which might be hard to identify using the pXRD. In the four drill cores of Metsämonttu it was possible to observe the abundance of chloritic alteration and see the chemical changes of chlorite group minerals. It was observed that in the drill cores MM-190, MM-196, MM-198 and MM-241 the increase of Mg-rich chlorite group minerals was connected to the presence of the ore minerals (Figs. 31, 37, 42 and 47).

It was also noticed that the VNIR data did not bring much additional information to the analysis of these four drill cores. There were plenty of data points that TSG identified as aspectral, and in addition, there were multiple empty measurements. Perhaps by extending the reference library of TSG would improve the data mining from this data source and increase the amount of identified mineral phases. However, it is good to keep in mind that there are only some mineral groups visible within the VNIR wavelength including iron oxides (e.g., Clark 1999).

In this work the SWIR data were successfully linked to the lithological data by using the wavelength positions of AlOH, FeOH, and MgOH absorption features (Figs. 33, 38, 43 and 48). The shifts of the wavelength positions can be used to draft large-scale boundaries of altered lithologies of the drill cores. These changes would also point out chemical alteration trends that could be bound together with the lithological units. This approach can be applied to other VMS and other hydrothermally altered ore deposits. It is perhaps not that sensitive in tracing very fine changes in the alteration trends, but it seems to be useful when drafting the bigger picture of the lithology. Several other studies (e.g., Thompson 1999; Herrmann et al. 2001; Jones et al. 2005; Squire et al. 2007; Laukamp et al. 2011; Tappert et al 2011; Harraden et al. 2013) have shown the usability of the NIR spectroscopy in alteration mapping, and this data can be possibly used for ore vectoring. In addition, it is an objective approach compared to the traditional core logging and alteration zone identification based on visual observation, that are always subjective (e.g., Herrmann et al. 2001).

However, it would be recommended to combine imaging spectroscopy methods using only VNIR and SWIR wavelengths to measurements done with LWIR wavelengths in order to expand the possibilities to identify more rock-forming mineral phases (e.g., Humbo 2019, Booysen 2021a). Information of several important rock-forming minerals such as quartz and feldspars is not obtained only from the VNIR and the SWIR measurements, and therefore plenty of information will not be reached. These limitations can be seen in example when the data are validated against the pXRD data (Figs. 30, 36, 41 and 46).

Due to the before-mentioned limitations the SWIR spectroscopy alone cannot be used for the determination of the abundance of minerals in the rock samples. However, the SWIR spectroscopy is applicable to identification of alteration mineralogy related to the zonation of the VMS deposits with some limitations, mainly the missing information regarding albitic alteration. It depends on the characteristics of each mineral deposit if this is important information or not. Additionally, it would be recommended to use the hyperspectral imaging data that would cover the surface of the whole drill core instead of the ASD point measurements measured with defined intervals that would only cover the area of the measurement window (Humbo 2019).

9 Conclusions

In this study the NIR spectroscopy with the SWIR and the VNIR wavelengths was tested as well as the use of the pXRD analyzer in the case of characterization of hydrothermal alteration zones of Metsämonttu VMS deposit. This data were validated against the petrophysical and geochemical data. The NIR spectroscopy using the SWIR wavelength was proven to be successful in characterization of hydrothermal alteration and shifts between lithological units.

However, the SWIR spectroscopy is limited in description of mineralogical variation since many rock-forming minerals such as quartz, albite, and pyroxenes fall outside of its observation range. When compared to the mineralogical data obtained with the pXRD, plenty of mineralogical variation is excluded if only the SWIR data would be used. On the contrary, the pXRD and XRD in general are more limited with its ability to detect subtle chemical variations of white mica and chlorite-group minerals that are more clearly visible in the SWIR data. In this study the VNIR spectroscopy did not bring much of additional value to the SWIR data since there were not that many mineral phases identified with it. However, it was possible to find some galvanized iron and Zn-Al alloys with it from the drill core MM-190 and link this data to the petrophysical data.

This study showed that within these four drill cores there was a correlation between the Mg-rich chlorite group phases to the appearance of ore minerals. However, this should be tested further with a larger set of drill cores in order to find out better its possible uses as an exploration vector.

Interpretation of the pXRD data would certainly speed up by using a powerful, algorithm-based tool for automatic mineral identification such as SwiftMin coupled with a reference database limited only to accepted mineral names and diffraction patterns preferably with an option to double-check the quality of the reference pattern. However, it is good to approach these novel methods with a critical mind remembering the limitations of the XRD as a method. Due to structural and chemical variety there might be numerous different diffraction patterns for a mineral with the same name, and the physical properties of a sample such as high amount of amorphous material or nano-scale grain size can bring their own problems to the interpretation.

For future studies, it would be useful to validate the pXRD data obtained from Metsämonttu against the laboratory XRD, the microprobe or the SEM measurements so it would be possible to see whether there would be differences in the identified mineralogy. It would be necessary to compare if the problems with sulphidic and plate-like minerals would repeat also in the laboratory XRD data, or would these observations limit only to the pXRD data. Using the XRF data made of whole rock samples measured with the laboratory XRF would bring additional information on alterations especially if now lacking sodium values could be used in the characterization of alteration zones. This data could be compared to the observations made of the SWIR and the pXRD data.

10 Acknowledgements

I would like to thank my supervisor professor Esa Heilimo from the University of Turku for all your professional and academic advice. Without your contribution and dedication this work would have never been published. I would also like to thank my second supervisor, researcher Irmeli Huovinen from the Geological Survey of Finland (GTK) for all your help, advice, and encouragement with this work, and last but not least, for finding this subject.

I would like to thank researcher Pasi Heikkilä from the Research Laboratory of GTK of sharing all your knowledge regarding XRD, XRF, and mineralogy. I am also very grateful to the head of the

Research Laboratory of GTK Marja Lehtonen of the ability to work in the laboratory and learn more from the analytical methods used there.

My greatest thanks to geologist Jaro Kuikka from GTK for helping me with the SWIR data and teaching me to use The Spectral Geologist. I would like to thank specialist Janne Hokka from GTK for insightful discussions of Metsämonttu deposit and sharing your knowledge of the topic. I am grateful also to team manager Hanna Leväniemi from GTK who gave me a permission to use the published material from Metsämonttu in this work. Finally, I would like to give special thanks to team manager Katja Lalli and specialist Maija Pennanen from GTK, who helped me to find this thesis subject.

11 References

AIRO, M. and SÄÄVUORI, H., 2013. Petrophysical characteristics of Finnish bedrock: Concise handbook on the physical parameters of bedrock. Geological Survey of Finland, Report of Investigation, 205, 33 pp.

ALT, J.C., 1995. Subseafloor Processes in Mid-Ocean Ridge Hydrothermal Systems. In: Humphris, S.E., Zierenberg, R.A., Mullineaux, L.S., and Thomson, R.E. (eds.) Seafloor Hydrothermal Systems: Physical, Chemical, Biological, and Geological Interactions, Geophysical Monograph Series, 91, Washington, DC: American Geophysical Union, 85–114.

ARO, K. and LAITAKARI, I. 1987. Suomen diabaasit ja muut mafiset juonikivilajit = Diabases and Other Mafic Dyke Rocks in Finland. Espoo: Geologian tutkimuskeskus, 254 pp.

ASHCROFT, N.W. and MERMIN, N.D., 2021. Solid state physics. Boston: Cengage, 826 pp.

BERMAN, M., BISCHOF, L., LAGERSTROM, R., GUO, Y., HUNTINGTON, J., and MASON, P., 2011. An Unmixing Algorithm Based on a Large Library of Shortwave Infrared Spectra. CSIRO, DOI: https://doi.org/10.4225/08/584c433f7ab79, 1-37.

BILLINGE, S.J.L. and DINNEBIER, R.E., 2008. Powder diffraction: theory and practice. Cambridge: Royal Society of Chemistry, 582 pp.

BLAKE, D., VANIMAN, D., ACHILLES, C., ANDERSON, R., BISH, D., BRISTOW, T., CHEN, C., CHIPERA, S., CRISP, J., DES MARAIS, D., DOWNS, R.T., FARMER, J., FELDMAN, S., FONDA, M., GAILHANOU, M., MA, H., MING, D.W., MORRIS, R.V., SARRAZIN, P., STOLPER, E., TREIMAN, A. and YEN, A., 2012. Characterization and Calibration of the CheMin Mineralogical Instrument on Mars Science Laboratory. Space science reviews, 170, 341-399.

BONNET, A. and CORRIVEAU, L., 2007. Alteration Vectors to Metamorphosed Hydrothermal Systems in Gneissic Terranes. In: Goodfellow, W.D. (ed.) Mineral deposits of Canada—A synthesis of major deposit-types, district metallogeny, the evolution of geological provinces, and exploration methods: Special Publication 5. Geological Association of Canada, Mineral Deposits Division, 1035-1049.

BOOYSEN, R., GLOAGUEN, R., LORENZ, S., ZIMMERMANN, R. and NEX, P., 2021a. Geological Remote Sensing. In: Encyclopaedia of Geology, 2nd ed., Elsevier, 301-314.

BOOYSEN, R., LORENZ, S., THIELE, S.T., FUCHSLOCH, W.C., MARAIS, T., NEX, P.A.M. and GLOAGUEN, R., 2021b. Accurate imaging spectroscopy of mineralised outcrops: An example from lithium-bearing pegmatites at Uis, Namibia. Remote Sensing of Environment, DOI: 10.1016/j.rse.2021.112790, 1-17.

BURKETT, D., 2018. Portable X-ray diffraction for unconventional and conventional petroleum exploration. ASEG Extended Abstracts, 1, DOI: 10.1071/ASEG2018abW9_4B, 1-4.

BURKETT, D., GRAHAM, I. and WARD, C., 2015. The application of portable X-ray diffraction to quantitative mineralogical analysis of hydrothermal systems. The Canadian Mineralogist, 53, 429-454.

BURNS, R.G., 1993. Mineralogical Applications of Crystal Field Theory. 2nd ed. Cambridge: Cambridge University Press, 551 pp.

CHUNG, F.H., 1974. Quantitative interpretation of X-ray diffraction patterns of mixtures. I. Matrix-flushing method for quantitative multicomponent analysis. Journal of applied crystallography, 7, 519-525.

CLARK, G.L. and REYNOLDS, D.H., 1936. Quantitative analysis of mine dusts: An X-ray diffraction method. Industrial & engineering chemistry. Analytical edition, 8, 36-40.

CLARK, R.N. and ROUSH, T.L., 1984. Reflectance spectroscopy: Quantitative analysis techniques for remote sensing applications. Journal of Geophysical Research: Solid Earth, 89, 6329-6340.

CLARK, R.N., KING, T.V.V., KLEJWA, M., SWAYZE, G.A. and VERGO, N., 1990. High spectral resolution reflectance spectroscopy of minerals. Journal of Geophysical Research: Solid Earth, 95, 12653-12680.

CLARK, R.N., 1999. Spectroscopy of rocks and minerals and principles of spectroscopy. In: ANDREW N. RENCZ, ed., Manual of Remote Sensing, Wiley, 3-58.

CORNABY, S., REYES-MENA, R., PEW, H. K., MOODY, P. W., HUGHES, T., STRADLING, A., TURNER, D. C. and KNIGHT, L. V., 2001. An XRD/XRF instrument for the microanalysis of rocks and minerals. Measurement science and technology, 12, 676-683.

CORNELL, R. M. and SCHWERTMANN, U., 2003. The Iron Oxides: Structure, Properties, Reactions, Occurences and Uses. Weinheim: Wiley-VCH, 664 pp.

DEBYE, P. and SCHERRER, P., 1916. Interferenzen an regellos orientierten Teilchen im Röntgenlicht. Physikalische Zeitschrift, 17, 277-283.

DEKKERS, M.J., 1989. Magnetic properties of natural pyrrhotite. II. High- and low-temperature behaviour of J_{rs} and TRM as function of grain size. Physics of the Earth and Planetary Interiors, 57, 266-283.

DE LA TORRE, A.G., BRUQUE, S. and ARANDA, M.A.G., 2001. Rietveld quantitative amorphous content analysis. Journal of applied crystallography, 34, 196-202.

DOLLASE, W.A., 1986. Correction of intensities for preferred orientation in powder diffractometry: application of the March model. Journal of applied crystallography, 19, 267-272.

DOUBLIER, M.P., ROACHE, T. and POTEL, S., 2010. Short-wavelength infrared spectroscopy; a new petrological tool in low-grade to very low-grade pelites. Geology, 38, 1031-1034.

DOUBLIER, M.P., ROACHE, T., POTEL, S. and LAUKAMP, C., 2012. Short-wavelength infrared spectroscopy of chlorite can be used to determine very low metamorphic grades. European journal of mineralogy (Stuttgart); An international journal of Mineralogy, Petrology, Geochemistry and related sciences, 24, 891-902.

EHARA SURYANTINI, S., VAN RUITENBEEK, F.J.A. and VAN DER MEER, F.D., 2008. The effect of weathering on reflectance spectra of hydrothermal white micas and chlorites: Implications for alteration mapping. In: Bierlein, F.P. and Mao, J. (eds.), 2008. Mineral deposit research: Meeting the global challenge, Berlin, Heidelberg: Springer, 703-706.

EILU, P., AHTOLA T., ÄIKÄS, O., HALKOAHO, T., HEIKURA, P., HULKKI, H., ILJINA, M., JUOPPERI, H., KARINEN, T., KÄRKKÄINEN, N., KONNUNAHO, J., KONTINEN, A., KONTONIEMI, O., KORKIAKOSKI, E., KORSAKOVA, M., KUIVASAARI, T., KYLÄKOSKI, M., MAKKONEN, H., NIIRANEN, T., NIKANDER, J., NYKÄNEN, V., PERDAHL, J.-A., POHJOLAINEN, E., RÄSÄNEN, J., SORJONEN-WARD, P., TIAINEN, M., TONTTI, M., TORPPA, A., and VÄSTI, K., 2012. Mineral deposits and metallogeny of Fennoscandia. 2nd ed. Geological Survey of Finland, Special Paper, 53, 401.

ERMRICH, M. and OPPER, D., 2011. X-Ray Powder Diffraction. XRD for the analyst. PANalytical GmbH, 94 pp.

ESKOLA, P., 1914. On the petrology of the Orijärvi region in southwestern Finland. Geological Survey of Finland, Bulletin - Bulletin de la Commission Géologique de Finlande, 40, 277 pp.

ESKOLA, P., 1915. Om sambandet mellan kemisk och mineralogisk sammansättning hos Orijärvitraktens metamorfa bergarter. Summary of the contents: On the relations between the chemical and mineralogical composition in the metamorphic rocks of the Orijärvi region. Geological Survey of Finland, Bulletin - Bulletin de la Commission Géologique de Finlande, 44, 145 pp.

FARMER, V.C., 1974. The Infrared Spectra of Minerals. Mineralogical Society of Great Britain and Ireland, 539 pp.

FRANKLIN, J.M., GIBSON, H.L., JONASSON, I.R. and GALLEY, A.G., 2005. Volcanogenic Massive Sulfide Deposits. In: J.W. HEDENQUIST, J.F.H. THOMPSON, R.J. GOLDFARB and J.P. RICHARDS (eds.), One Hundredth Anniversary Volume. Society of Economic Geologists, 525-560.

GALLEY, A.G., 1993. Characteristics of semi-conformable alteration zones associated with volcanogenic massive sulphide districts. Journal of Geochemical Exploration, 48, 175-200.

GALLEY, A., HANNINGTON, M.D. and JONASSON, I., 2007. Volcanogenic massive sulphide deposits. In: Goodfellow, W.D. (ed.) Mineral deposits of Canada—A synthesis of major deposit-types, district metallogeny, the evolution of geological provinces, and exploration methods: Special Publication 5. Geological Association of Canada, Mineral Deposits Division, 141-161.

GEMMELL, J.B. and LARGE, R.R., 1992. Stringer system and alteration zones underlying the Hellyer volcanogenic massive sulfide deposit, Tasmania, Australia. Economic Geology, 87, 620-649.

GIACOVAZZO, C., 1992. Fundamentals of crystallography. Oxford: International Union of Crystallography, 654 pp.

GIANONCELLI, A., CASTAING, J., ORTEGA, L., DOORYHÉE, E., SALOMON, J., WALTER, P., HODEAU, J. and BORDET, P., 2008. A portable instrument for in situ determination of the chemical and phase compositions of cultural heritage objects. X-Ray Spectrometry, 37, 418-423.

GOODFELLOW, W.D., PETER, J.M., WINCHESTER, J.A. and STAAL, C.R.V, 2003. Ambient Marine Environment and Sediment Provenance during Formation of Massive Sulfide Deposits in the Bathurst Mining Camp: Importance of Reduced Bottom Waters to Sulfide Precipitation and Preservation. In: Goodfellow, W.D., McCutcheon, S.R., and Peter, J.M. (eds.), Volcanogenic massive sulphide deposits of the Bathurst mining camp, New Brunswick, and northern Maine. Economic Geology Monograph, 11, 129-156.

GUIDOTTI, C.V., SASSI, F.P., SASSI, R. and BLENCOE, J.G., 1994. The effects of ferromagnesian components on the paragonite-muscovite solvus: a semiquantitative analysis based on chemical data for natural paragonite-muscovite pairs. Journal of Metamorphic Geology, 12, 779-788.

HAEST, M., CUDAHY, T., LAUKAMP, C. and GREGORY, S., 2012. Quantitative mineralogy from Infrared spectroscopic data. I. Validation of mineral abundance and composition scripts at the Rocklea Channel iron deposit in Western Australia. Economic Geology and the Bulletin of the Society of Economic Geologists, 107, 209-228.

HANNINGTON, M.D., GALLEY, A., HERZIG, P. and PETERSEN, S., 1998. Comparison of the TAG mound and stockwork complex with Cyprus-type massive sulfide deposits. Oceanographic Literature Review, 158, 1557-1558.

HANNINGTON, M.D., 2014. Volcanogenic Massive Sulfide Deposits. Treatise on Geochemistry: 2nd ed., 13, 463-488.

HARRADEN, C.L., MCNULTY, B.A., GREGORY, M.J. and LANG, J.R., 2013. Shortwave Infrared Spectral Analysis of Hydrothermal Alteration Associated with the Pebble Porphyry Copper-Gold-Molybdenum Deposit, Iliamna, Alaska. Economic Geology, 108, 483-494.

HASHIGUCHI, H., YAMADA, R. and INOUE, T., 1983. Practical Application of Low Na2O Anomalies in Footwall Acid Lava for Delimiting Promising Areas around the Kosaka and Fukazawa Kuroko Deposits, Akita Prefecture, Japan. In: H. OHMOTO and B.J. SKINNER, eds., The Kuroko and Related Volcanogenic Massive Sulfide Deposits. Society of Economic Geologists, 387-394.

HEDENQUIST, J.W. and LOWENSTERN, J.B., 1994a. The role of magmas in the formation of hydrothermal ore deposits. Nature, 370, 519-527.

HERRMANN, W., BLAKE, M., DOYLE, M., HUSTON, D., KAMPRAD, J., MERRY, N. and PONTUAL, S., 2001. Short Wavelength Infrared (SWIR) Spectral Analysis of Hydrothermal Alteration Zones Associated with Base Metal Sulfide Deposits at Rosebery and Western Tharsis, Tasmania, and Highway-Reward, Queensland. Economic Geology, 96, 939-955.

HILL, R.J. and HOWARD, C.J., 1987. Quantitative phase analysis from neutron powder diffraction data using the Rietveld method. Journal of applied crystallography, 20, 467-474.

HUMBO, E.J., 2019. Hyperspectral imaging in SWIR and LWIR of low-grade metamorphic rocks. M.Sc. Thesis. University of Twente, Faculty of Geo-information Science and Earth Observation, 77 pp (unpublished).

HUNT, G.R. and ASHLEY, R.P., 1979. Spectra of altered rocks in the visible and near infrared. Economic Geology and the Bulletin of the Society of Economic Geologists, 74, 1613-1629.

ICRU, 1980. Radiation Quantities and Units. Report 33. Bethesda, MD: International Commission on Radiation Units and Measurements, 25 pp.

ISAACSON, P., KLIMA, R., SUNSHINE, J., CHEEK, L., PIETERS, C., HIROI, T., DYAR, M., LANE, M. and BISHOP, J., 2014. Visible to near-infrared optical properties of pure synthetic olivine across the olivine solid solution. American Mineralogist, 99, 467-478.

ISHIKAWA, Y., SAWAGUCHI, T., IWAYA, S. and HORIUCHI, M., 1976. Delineation of Prospecting Targets for Kuroko Deposits Based on Modes of Volcanism of Underlying Dacite and Alteration Halos. Mining Geology, 26, 105-117.

JONES, S., HERRMANN, W. and GEMMELL, J.B., 2005. Short Wavelength Infrared Spectral Characteristics of the HW Horizon: Implications for Exploration in the Myra Falls Volcanic-Hosted Massive Sulfide Camp, Vancouver Island, British Columbia, Canada. Economic Geology, 100, 273-294.

KISHIDA, A. and KERRICH, R., 1987. Hydrothermal alteration zoning and gold concentration at the Kerr-Addison Archean lode gold deposit, Kirkland Lake, Ontario. Economic Geology, 82, 649-690.

KOSKELA, E., LAAKSO, V. and GALVIN, K., 2019. Geophysical characterization of the Orijärvi-Aijala VMS belt based on archived reports, geophysical and petrophysical data. Geological Survey of Finland, Open File Work Report 102/2019, 30 pp.

KOSKINEN, H., 2018. Kannettavan XRD-analysaattorin soveltuvuus kriittisten mineraalien tunnistamiseen kentällä. M.Sc. Thesis. University of Oulu, 77 pp (unpublished).

KÄHKÖNEN, Y., 2005. Svecofennian supracrustal rocks. In: LEHTINEN, M., NURMI, P.A. and RÄMÖ, O.T., 2005. Precambrian geology of Finland: key to the evolution of the Fennoscandian shield. Amsterdam: Elsevier, 343-405.

LAAKSO, K., PETER, J.M., RIVARD, B. and WHITE, H.P., 2016. Short-Wave Infrared Spectral and Geochemical Characteristics of Hydrothermal Alteration at the Archean Izok Lake Zn-Cu-Pb-Ag Volcanogenic Massive Sulfide Deposit, Nunavut, Canada: Application in Exploration Target Vectoring. Economic Geology, 111, 1223-1239.

LARGE, R.R., 1992. Australian volcanic-hosted massive sulfide deposits; features, styles, and genetic models. Economic Geology and the Bulletin of the Society of Economic Geologists, 87, 471-510.

LARGE, R.R., 2001a. The Alteration Box Plot: A Simple Approach to Understanding the Relationship between Alteration Mineralogy and Lithogeochemistry Associated with Volcanic-Hosted Massive Sulfide Deposits. Economic Geology and the Bulletin of the Society of Economic Geologists, 96, 957-971.

LARGE, R.R., MCPHIE, J., GEMMELL, J.B., HERRMANN, W. and DAVIDSON, G.J., 2001b. The spectrum of ore deposit types, volcanic environments, alteration halos, and related exploration vectors in submarine volcanic successions; some examples from Australia. Economic Geology and the Bulletin of the Society of Economic Geologists, 96, 913-938.

LATVALAHTI, U., 1979. Cu-Zn-Pb ores in the Aijala-Orijärvi area, southwest Finland. Economic Geology and the Bulletin of the Society of Economic Geologists, 74, 1035-1059.

LAUKAMP, C., CUDAHY, T., THOMAS, M., JONES, M., CLEVERLEY, J.S. and OLIVER, N.H.S., 2011. Hydrothermal mineral alteration patterns in the Mount Isa Inlier revealed by airborne hyperspectral data. Australian Journal of Earth Sciences, 58, 917-936.

LEMIÈRE, B. and UVAROVA, Y.A., 2020. New developments in field portable geochemical techniques and on-site technologies and their place in mineral exploration. Geochemistry : exploration, environment, analysis, 20, 205-216.

LEHTINEN, M., NURMI, P.A. and RÄMÖ, O.T., 2005. Precambrian geology of Finland: key to the evolution of the Fennoscandian shield. Amsterdam: Elsevier, 736 pp.

LEMIÈRE, B. and UVAROVA, Y.A., 2020. New developments in field portable geochemical techniques and on-site technologies and their place in mineral exploration. Geochemistry: exploration, environment, analysis, 20(2), 205-216.

LEVÄNIEMI, H., 2019. Performance of the KT-20 susceptibility meter and the BJ6100D density balance for drillcore measurements. Geological Survey of Finland, Open File Work Report 63/2019, 17 pp.

LEVÄNIEMI, H., HOKKA, J., HULKKI, H., HUOVINEN, I., KARJALAINEN, J., KAUNISMÄKI, J., KUIKKA, J., SANDSTRÖM, J., STENBERG, R. and VUOHELAINEN, J., 2020. Tiedonkeruukäytännöt Aijala-Metsämonttu -projektin kairasydänmittauksissa 2019-2020. Geological Survey of Finland, Open File Work Report 39/2020, 51 pp.

LEVÄNIEMI, H. and HOKKA, J., 2021. Petrophysical target characterization with lithogeochemical clustering: the Metsämonttu Zn–Pb–Cu deposit, southern Finland. Near Surface Geophysics, John Wiley & Sons Ltd, DOI: 10.1002/nsg.12182, 1-24.

LIMA DE FARIA, J., 1964. Identification of metamict minerals by x-ray powder photographs. Lisboa: Junta de investigacoes do ultramar, Estudos, ensaios e documentos, 112, 74 pp.

LUUKAS, J., KOUSA, J., NIRONEN, M. and VUOLLO, J., 2017. Major stratigraphic units in the bedrock of Finland, and an approach to tectonostratigraphic division. In: Nironen, M. (ed.), 2017. Bedrock of Finland at the scale 1:1 000 000 – Major stratigraphic units, metamorphism and tectonic evolution. Geological Survey of Finland, Special Paper, 60, 9-40.

LYDON, J.W., 1984. Volcanogenic Massive Sulphide Deposits Part I: A Descriptive Model. Geoscience Canada, 11, 195-202.

LYDON, J.W., 1996. Characteristics of volcanogenic massive sulfide deposits — Interpretations in terms of hydrothermal convection systems and magmatic hydrothermal systems. Instituto Tecnologico Geominero de Espana, Boletin Geologico y Minero, 3-4, 15-64.

MARTIN, J. D., 2008. XPowder. Qualitative, quantitative and microtexture. User guide. 160 pp.

MASSA, W. and GOULD, R.O., 2004. Crystal structure determination. 2nd ed. Berlin: Springer, 210 pp.

MASSONNE, H. and SCHREYRER, W., 1987. Phengite geobarometry based on the limiting assemblage with K-feldspar, phlogopite, and quartz. Contributions to mineralogy and petrology, 96, 212-224.

MATHIEU, L., 2018. Quantifying Hydrothermal Alteration: A Review of Methods. Geosciences, 8, 1-27.

MAYDAGÁN, L., FRANCHINI, M., IMPICCINI, A., LENTZ, D., PATRIER, P. and BEAUFORT, D., 2018. Chlorite, white mica and clay minerals as proximity indicators to ore in the shallow porphyry environment of Quebrada de la Mina deposit, Argentina. Ore geology reviews, 92, 297-317.

MCCANTA, M.C. and DYAR, M.D., 2020. Effects of oxidation on pyroxene visible-near infrared and mid-infrared spectra. Icarus, 352, 1-11.

MCNULTY, B.A., FOX, N. and GEMMELL, J.B., 2020. Assessing hydrothermal alteration intensity in volcanic-hosted massive sulfide systems using portable X-ray fluorescence analysis of drill core: An example from Myra Falls, Canada. Economic Geology, 115, 443-453.

MIDDLETON, M., NÄRHI, P., KUOSMANEN, V. and SUTINEN, R., 2011. Quantification of glacial till chemical composition by reflectance spectroscopy. Applied Geochemistry, 26, 2215-2225.

MOORE, J. and AULT, W., 1965. Historic Littoral Cones in Hawaii. Pacific Science, 19, 3-11.

MORRIS, R.V., LAUER JR., H.V., LAWSON, C.A., GIBSON JR., E.K., NACE, G.A. and STEWART, C., 1985. Spectral and other physicochemical properties of submicron powders of hematite (α-Fe2O3), maghemite (γ-Fe2O3), magnetite (Fe3O4), goethite (α-FeOOH), and lepidocrocite (γ-FeOOH). Journal of Geophysical Research: Solid Earth, 90, 3126-3144.

MÄKELÄ, U., 1989. Geological and geochemical environments of Precambrian sulphide deposits in southwestern Finland. Ph. D. dissertation, University of Turku. Suomalainen tiedeakatemia, 102 pp.

NIRONEN, M. (ed.) 2017. Bedrock of Finland at the scale 1:1 000 000 – Major stratigraphic units, metamorphism and tectonic evolution. Geological Survey of Finland, Special Paper 60, 41-76.

NIRONEN, M. and LUUKAS, J., 2017. Definition of the Kisko group for Finstrati. Geological Survey of Finland, Open File Work Report 57/2017, 24 pp.

OGIERMANN, J. and KALT, A., 2000. Chemical Characterization of Cordierite Breakdown Products in Gneisses and Migmatites of the Schwarzwald and the Bayerische Wald. Journal of Conference Abstracts 5, 752.

OLYMPUS, 2020. *Terra™ II Portable XRD Analyzer.* [https://www.olympus-ims.com/en/xrf-xrd/mobile-benchtop-xrd/terra/#!cms[tab] =%2Fxrf-xrd%2Fmobile-benchtop-xrd%2Fterra%2Fresources] Visited 29.4.2021.

OUTOKUMPU OY, 1959a. Core drilling report n:o 3418. Aijala district, Metsämonttu mine, hole n:o MM-190.

OUTOKUMPU OY, 1959b. Core drilling report n:o 3419. Aijala district, Metsämonttu mine, hole n:o MM-196.

OUTOKUMPU OY, 1959c. Core drilling report n:o 3425. Aijala district, Metsämonttu mine, hole n:o MM-198.

OUTOKUMPU OY, 1961. Core drilling report n:o 3445. Aijala district, Metsämonttu mine, hole n:o MM-241.

PARKKINEN, J., 1975. Uusi Metsämonttu. Rakennegeologinen ja malmipetrografinen tutkimus. Outokumpu Oy, 61 pp.

PEARCE, J., 1996. A User's Guide to Basalt Discrimination Diagrams. Geological Association of Canada Short Course Notes, 12, 79-113.

PEARCE, T.H., 1968. A contribution to the theory of variation diagrams. Contributions to mineralogy and petrology, 19, 142-157.

PECHARSKY, V.K. and ZAVALIJ, P.Y., 2009. Fundamentals of powder diffraction and structural characterization of materials. 2nd ed. New York: Springer, 741 pp.

PIERCEY, S., ed, 2009. Lithogeochemistry of volcanic rocks associated with volcanogenic massive sulfide (VMS) deposits and applications to exploration. In: Cousens, B., and Piercey, S.J., eds., Submarine volcanism and mineralization — Modern through ancient: Geological Association of Canada. Short Course Notes, v. 19, 15–40.

PUUSTINEN, K., 2003. Suomen kaivosteollisuus ja mineraalisten raaka-aineiden tuotanto vuosina 1530-2001, historiallinen katsaus erityisesti tuotantolukujen valossa. Geologian tutkimuskeskus, 578 pp.

RAJA-HALLI, H. 1949. Aijalan ”Metsämontun” sinkkimalmi. Metsämonttu 1 Kaivospiiri. 1950. Outokumpu Oy. Kaivosoikeudesta luopuminen, Kaivosrekisterinumero 0712/1a.

RAMOS DIAS DE ANDRADE, F., GOBBO, L.D.A. and SOUSA, L.F.A., 2016. Iron ore classification by XRD-Rietveld and cluster analysis. Geologia USP. Série científica, 16, 19.

RIETVELD, H.M., 1969. A profile refinement method for nuclear and magnetic structures. Journal of applied crystallography, 2, 65-71.

ROBB, L., 2005. Introduction to ore-forming processes. Malden, MA: Blackwell, 373 pp.

ROSS, P., BOURKE, A. and FRESIA, B., 2013. A multi-sensor logger for rock cores: Methodology and preliminary results from the Matagami mining camp, Canada. Ore geology reviews, 53, 93-111.

RUMBLE, J.R. (ed.), 2021. CRC handbook of chemistry and physics. 102nd ed. (Internet version 2021). Boca Raton, FL: CRC Press/Taylor and Francis Group. Visited 1.12.2021.

SAEKI, Y. and DATE, J., 1980. Computer application to the alteration data of the footwall dacite lava at the Ezuri kuroko deposits, Akita Prefecture. Mining Geology, 30, 241-250.

SARALA, P. and KOSKINEN, H., 2018. Application of the portable X-Ray Diffraction (pXRD) analyser in surficial geological exploration. Geologi, 70, 58-68.

SARALA, P., TAIVALKOSKI, A., HUOVINEN, I., KALLIOSALO, H., KARINEN, J., KOSKINEN, H., LEHTONEN, M., LUKKARI, S., STRAND, K., TOPPILA, R., JOUTSENVAARA, J. and VALKAMA, J., 2019. Indikaattorimineraalien automatisoitu tunnistaminen kriittisten mineraalien etsinnässä - Indika: Loppuraportti. Geological Survey of Finland, Open File Work Report 47/2019, 74 pp.

SARRAZIN, P., BLAKE, D., FELDMAN, S., CHIPERA, S., VANIMAN, D. and BISH, D., 2005. Field deployment of a portable X-ray diffraction/X-ray fluorescence instrument on Mars analog terrain. Powder Diffraction, 20, 128-133.

SCHNEIDERMAN, J.S. and TRACY, R.J., 1991. Petrology of orthoamphibole-cordierite gneisses from the Orijärvi area, southwest Finland. American Mineralogist, 76(5-6), 942-955.

SHANKS III, W.C.P., 2012. Hydrothermal alteration. In: SHANKS III, W. C. P. and THURSTON, R. 2012. Volcanogenic massive sulfide occurrence model: Chapter C in Mineral deposit models for resource assessment. Reston, VA, 169-180.

SMITH, D.K., JOHNSON, G.G., SCHEIBLE, A., WIMS, A.M., JOHNSON, J.L. and ULLMANN, G., 1987. Quantitative X-Ray Powder Diffraction Method Using the Full Diffraction Pattern. Powder Diffraction, 2, 73-77.

SNELLINGS, R., BAZZONI, A. and SCRIVENER, K., 2014. The existence of amorphous phase in Portland cements: Physical factors affecting Rietveld quantitative phase analysis. Cement and Concrete Research, 59, 139-146.

SPRY, P.G., PETER, J.M. and SLACK, J.F., 2000. Meta-Exhalites as Exploration Guides to Ore*. In: F.M. VOKES, B. MARSHALL and P.G. SPRY (eds.), Metamorphic and Metamorphogenic Ore Deposits. Reviews in Economic Geology, 81, 163-201.

SQUIRE, R.J., HERRMANN, W., PAPE, D. and CHALMERS, D.I., 2007. Evolution of the Peak Hill high-sulfidation epithermal Au–Cu deposit, eastern Australia. Mineralium Deposita, 42, 489-503.

SUN, Y., SECCOMBE, P. and YANG, K., 2001. Application of short-wave infrared spectroscopy to define alteration zones associated with the Elura zinc–lead–silver deposit, NSW, Australia. Journal of Geochemical Exploration, 73, 11-26.

SUOMEN MALMI OY, 1949. Yleisiä näkökohtia ja huomautuksia sähkömittauksista Suomen malmin laskuun vuosina 1945-48. Outokumpu Oy.

TAPPERT, M., RIVARD, B., GILES, D., TAPPERT, R. and MAUGER, A., 2011. Automated drill core logging using visible and near-infrared reflectance spectroscopy: A case study from the Olympic Dam IOCG deposit, South Australia. Economic Geology, 106, 289-296.

TAYLOR, B.E. and SLACK, J.F., 1984. Tourmalines from Appalachian-Caledonian massive sulfide deposits; textural, chemical, and isotopic relationships. Economic Geology and the Bulletin of the Society of Economic Geologists, 79, 1703-1726.

THOMPSON, A. J. B., HAUFF, P.L. and ROBITAILLE, A.J., 1999. Alteration Mapping in Exploration: Application of Short-Wave Infrared (SWIR) Spectroscopy. SEG Newsletter 39, 16-27.

TURNER, D. RIVARD, B. and GROAT, L. 2014. Rare earth element ore grade estimation of mineralized drill core from imaging spectroscopy. 2014 IEEE Geoscience and Remote Sensing Symposium 2014, 4612-4615.

UVAROVA, Y., CLEVERLEY, J., BAENSCH, A. and VERRALL, M., 2014. Coupled XRF and XRD analyses for rapid and low-cost characterization of geological materials in the mineral exploration and mining industry. EXPLORE Newsletter for the Association of Applied Geochemists, 162, 1-14.

UVAROVA, Y., TASSIOS, S., FRANCIS, N., LEGRAS, M., CLEVERLEY, J.S. and BAENSCH, A., 2020. Top-of-holes sensing techniques: developments within Deep Exploration Technologies Cooperative Research Centre. Australian Journal of Earth Sciences, DOI: 10.1080/08120099.2020.1743356, 1-13.

VELDE, B., 1965. Phengite micas; synthesis, stability, and natural occurrence. American journal of science, 263, 886-913.

VELDE, B., 1967. Si^{+4} Content of natural phengites. Contributions to mineralogy and petrology, 14, 250-258.

VÄISÄNEN, M. and MÄNTTÄRI, I., 2002. 1.90-1.88 Ga arc and back-arc basin in the Orijärvi area, SW Finland. Bulletin of the Geological Society of Finland, 74, 185-214.

WARMA, A., 1985. Outokumpu Oy:n Aijalan ja Metsämontun kaivosten vaiheita. Vuoriteollisuus, 33, 94-98.

WESTPHAL, T., FÜLLMANN, T. and PÖLLMANN, H., 2009. Rietveld quantification of amorphous portions with an internal standard—Mathematical consequences of the experimental approach. Powder Diffraction, 24, 239-243.

WILL, G., 2006. Powder diffraction: the Rietveld method and the two-stage method to determine and refine crystal structures from powder diffraction data. Berlin: Springer, 224 pp.

WINCHESTER, J.A. and FLOYD, P.A., 1977. Geochemical discrimination of different magma series and their differentiation products using immobile elements. Chemical Geology, 20, 325-343.

YANG, K., HUNTINGTON, J.F., GEMMELL, J.B. and SCOTT, K.M., 2011. Variations in composition and abundance of white mica in the hydrothermal alteration system at Hellyer, Tasmania, as revealed by infrared reflectance spectroscopy. Journal of Geochemical Exploration, 108, 143-156.

ZAINI, N., VAN DER MEER, F. D and VAN DER WERFF, H. M. A, 2012. Effect of grain size and mineral mixing on carbonate absorption features in the SWIR and TIR wavelength regions. Remote sensing, 4, 987-1003.

12 Appendices

Appendix 1. The stacked portable XRD spectra of the drill core MM-190.

Appendix 2. The stacked portable XRD spectra of the drill core MM-196.

Appendix 3. The stacked portable XRD spectra of the drill core MM-198.

Appendix 4. The stacked portable XRD spectra of the drill core MM-241.

Appendix 5. A table of the portable XRD data represented by mineral group.

Appendix 1. The stacked portable XRD spectra of the drill core MM-190.

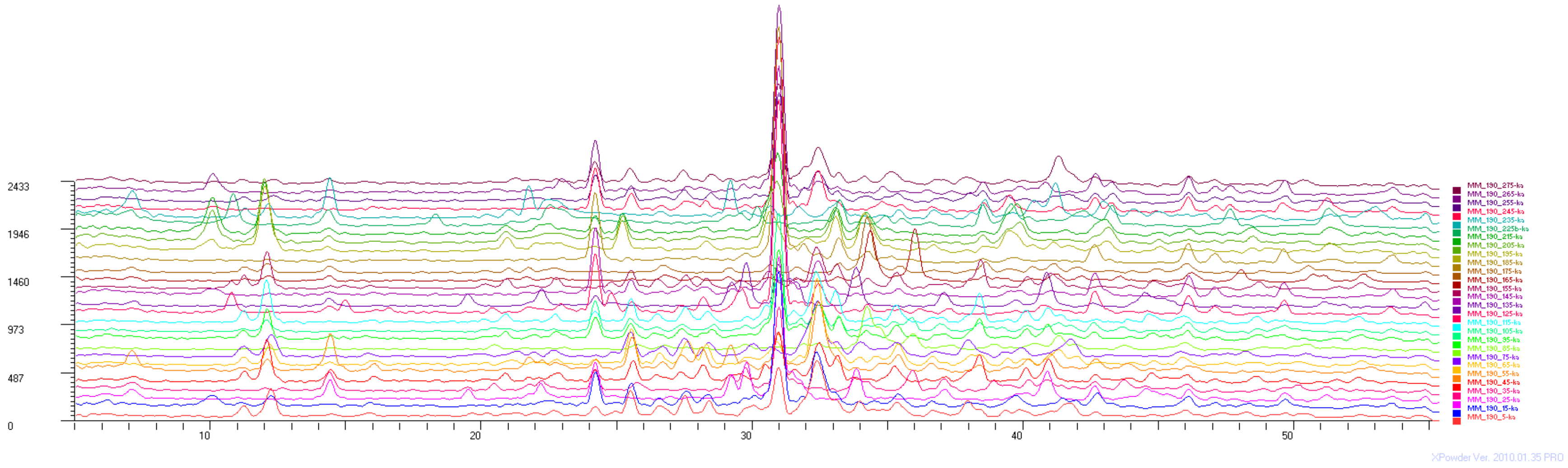

Appendix 2. The stacked portable XRD spectra of the drill core MM-196.

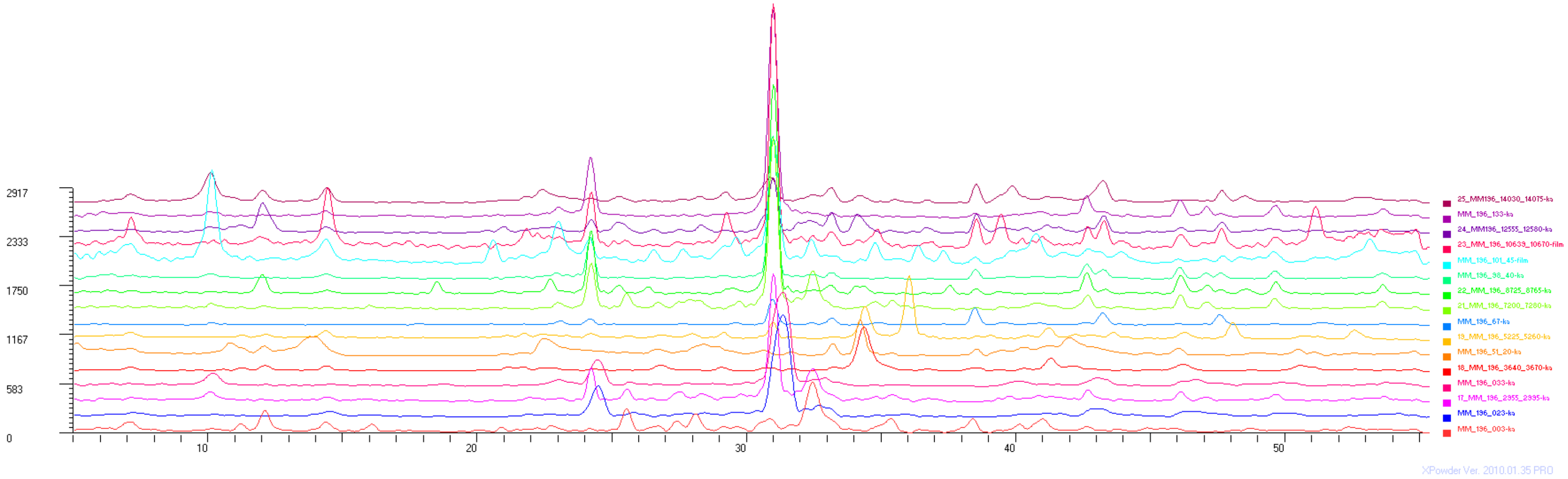

Appendix 3. The stacked portable XRD spectra of the drill core MM-198.

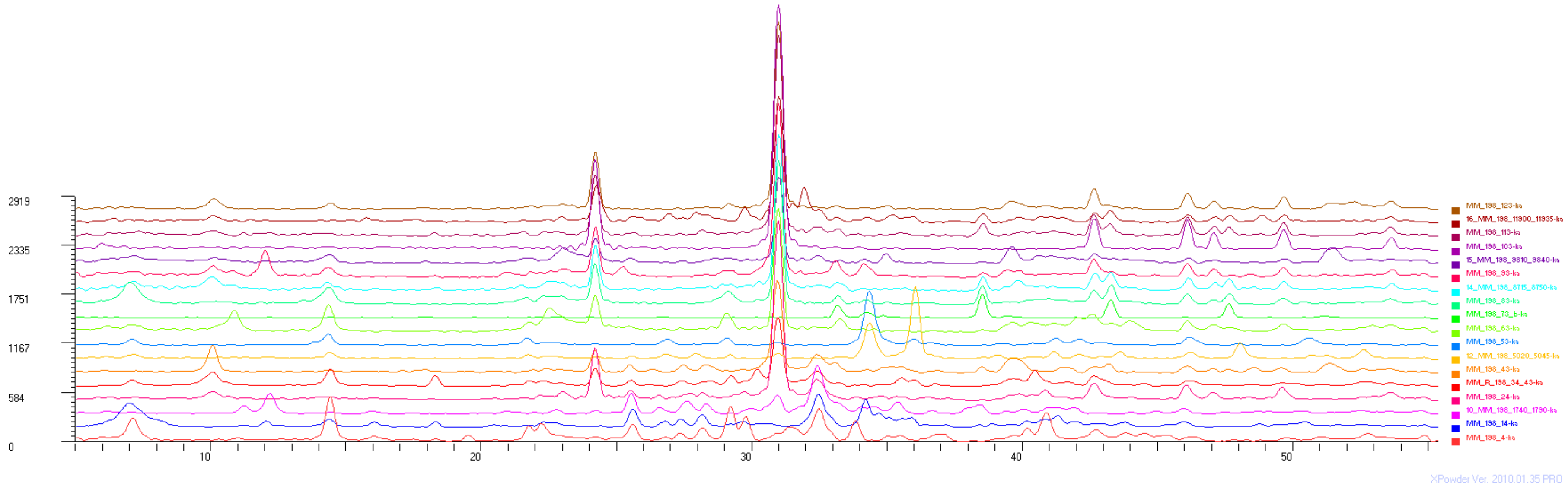

Appendix 4. The stacked portable XRD spectra of the drill core MM-241.

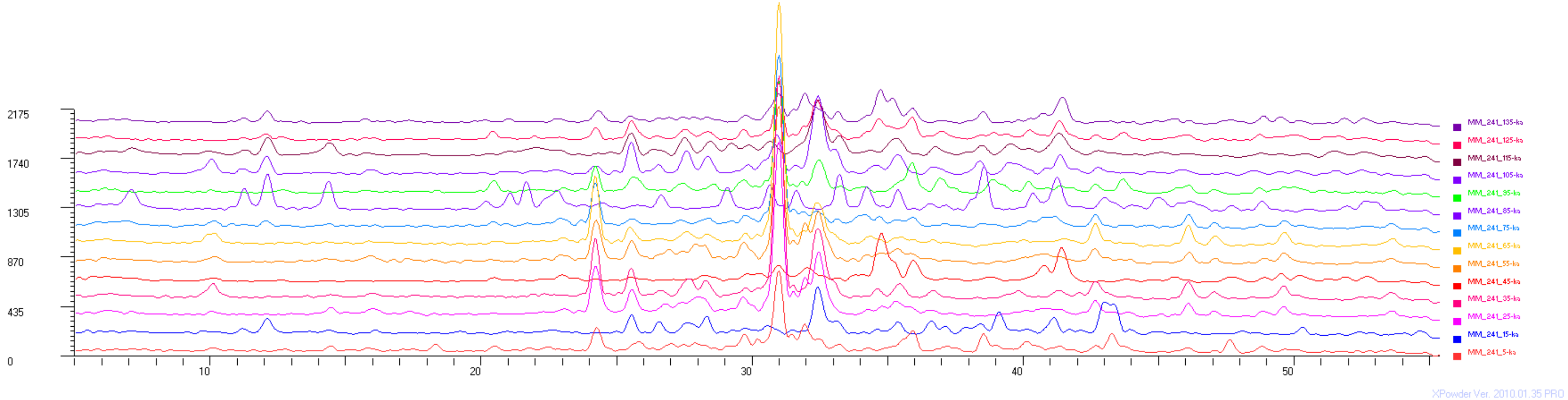

Appendix 5. A table of the portable XRD data represented by mineral group

Hole ID	**Depth**	Amp	And	Bt	Chl	Crd	Ep	Fsp	Grt	Ms	Prh	Px	Qz	Sep	Sme	Srp	Tlc	Zeo	Crb	Spl	SO_4	Am	**SUM**
MM-190	5	17.5			2.4			49.6				4	6.9									19.5	99.9
MM-190	15			5.9	3.5	5.4		57.1					17.5									10.5	99.9
MM-190	25				13.3			4.2			41.7		31.8									9	100
MM-190	35				23.9		17.3	6.9			22		17.4									12.4	99.9
MM-190	45	22.2			5.7			43.1					7									21.9	99.9
MM-190	55	4.6			12.6			53.8			3.9		4.8		0.7							19.6	100
MM-190	65	6.6						70			6		2.9						1			13.5	100
MM-190	75	16.7			2			62.1					1.5									17.7	100
MM-190	85				6.8		23.7	17.5		7.1			3.6						26.4			14.8	99.9
MM-190	95	19.8			4			44.4		7.4			12.6									11.8	100
MM-190	105	11.3					11.2	45.3					23.5									8.7	100
MM-190	115	18						53.8					7.4									20.9	100.1
MM-190	125				3.1			27.2		10.2			29.5					22.8				7.2	100
MM-190	135				7.5			6.9			56		10									19.6	100
MM-190	145			4				42.2		12.8			34.3									6.6	99.9
MM-190	155	18.8			2.4			38.1		7.2			2.3					9.4				21.8	100
MM-190	165	13.3			13			4.8					1.3						54.1			13.6	100.1
MM-190	175	21.3			14.7			16.1	3				3.3						26.6	2.3		12.8	100.1
MM-190	185					33.2		4					56.9									5.9	100
MM-190	195			9.1	5.2	30.5		14.3	5.1				6.2						1.9	3.4	5.2	19.2	100.1
MM-190	205			18.9	5	29		9	4.6				9							4.8		19.7	100
MM-190	215			16.3	10.2	26.6		6.8	6.5				14.7								2.7	16.3	100.1
MM-190	225			4.7	15.2	2		7.4				7.2	0.8				19.7	10.2			4.6	28.2	100
MM-190	235	17.4			44.7			4.6				4.6	2.1								0.7	25.9	100
MM-190	245				4.8			44.3	4.1	5.2		6	25.9								2.4	7.3	100
MM-190	255	8.1			5.4			47.9				4.4	22								2.1	10.2	100.1
MM-190	265			4.3				18.7	6.1	25.1			36.2								2.2	7.4	100
MM-190	275	7.9						56.7				2.4	18.3							2.9		11.7	99.9

Hole ID	**Depth**	Amp	And	Bt	Chl	Crd	Ep	Fsp	Grt	Ms	Prh	Px	Qz	Sep	Sme	Srp	Tlc	Zeo	Crb	Spl	SO_4	Am	**SUM**
MM-196	3	16.4		2.4	9.7			50.7					2.1									18.6	99.9
MM-196	23			3.1	11.8			25.2		18			32.5									9.5	100.1
MM-196	29			4.8	3.9			44.3		14.9			24.1									8	100
MM-196	33			8.9	6.8			21.8		20.2			32.3									9.9	99.9
MM-196	36	12.5			21.3	10.5		10.8					1.8						28.2	3.1		11.9	100.1
MM-196	51	12.4			12.2			3.4	2.4				1.7			14.8	14.2		14.9			24	100
MM-196	52				20.1	4.6		5.3					5.9						51.9	1.6		10.6	100
MM-196	67				4.4			14.6		31			16.2		3.3	4.4	2.8				10	13.2	99.9
MM-196	72					3.4		46.1		12.2			31.1									7.2	100
MM-196	87		13.1			21.2		8.5					51.3									5.9	100
MM-196	98				9.7	9.2		9.2		27.3			36.6								2.1	6	100.1
MM-196	101				12.2	2.4		16.8		35.5			13.4		1.2						1.1	17.4	100
MM-196	106	11.2			21.4			15.8					32.9		1.4					0.8	6.8	9.6	99.9
MM-196	125				9.2	23.6		15.6	4.4	8.1			10.7		1.3		6.3				4.5	16.4	100.1
MM-196	133			6.6	7.8			10		21.6			47.9									6.1	100
MM-196	140			21.9	23.3	11.2		12					4								3.6	24.1	100.1
MM-198	4				18.8			36.6			20.2		1.8									22.6	100
MM-198	14				10	2.7	6.5	38.8				5.6	6.2		1.3				6.5			22.5	100.1
MM-198	17	13.4			3			53.4		6.4		4.4	3.1									16.3	100
MM-198	24				3.3			33.3		26.3			30.3									6.8	100
MM-198	34			12.7	10.9			11.1	8.4	21.6			27.7									7.6	100
MM-198	43	10.1		18.3				32.9					20.4			2.9				3.9	1.4	10.1	100
MM-198	50				15.8			4					2.9						68			9.4	100.1
MM-198	53				43.2	2.3		4.3					1.8						38.7			9.7	100
MM-198	63				30.4			12.9	2.4				19.5		1.7	6.8	12.4			3.4		10.5	100
MM-198	73							20.4	10.5				2.9								54.6	11.6	100
MM-198	83				28.8	4.1		4.2		16.8			33.4		1.6						3.2	7.8	99.9
MM-198	87			7.4	15.5			10.2		15.5			39.2		1.1						3.1	8	100
MM-198	93			2.2	7.3	15.3		13.6		15.8			34.3						4.2			7.3	100
MM-198	98				15.8	4.9		12.9		31.8			16.5		0.6						5.9	11.7	100.1
MM-198	103												94.4									5.6	100

Hole ID	**Depth**	Amp	And	Bt	Chl	Crd	Ep	Fsp	Grt	Ms	Prh	Px	Qz	Sep	Sme	Srp	Tlc	Zeo	Crb	Spl	SO_4	Am	**SUM**
MM-198	113	16.1		5.1				13.6		13.1			40.6							5.4		6.1	100
MM-198	119					6.1		23.2		18.1			28.3	8.6						4.8	2.2	8.7	100
MM-198	123			16.8	14.4	2.3		6.4					54.5									5.7	100.1
MM-241	5				7.5		18.8	25.8	3.7	11.7			17.2								3	12.4	100.1
MM-241	15	6.4			4.8			50	6.2				8								4.5	20	99.9
MM-241	25				8.6			49.8		12.3			20.4									8.9	100
MM-241	35			6.1				58.5					27.9									7.5	100
MM-241	45				1.9		16.8	11.8		7.4		41.7	1.9								2	16.5	100
MM-241	55				5.4			44.6		13.3		6.3	20.5									9.9	100
MM-241	65			2.9	2.9	3.8		42.8		8.4			32.5									6.7	100
MM-241	75				7			15.6		23.1	11.7		27.2						7.5			7.7	99.8
MM-241	85	39			21.3			2.8					3.2						4.9		2.6	26.3	100.1
MM-241	95				2.4		21.5	31.9		15.2			18.3									10.6	99.9
MM-241	105	4.8		6.3			3.1	62.5	2.7				4.4									16.3	100.1
MM-241	115	8			6.6			53.7	2.3				7.5								2.2	19.6	99.9
MM-241	125	2.6					14.8	48.1				8	9.6									16.9	100
Average amount of the amorphous matter																						13.1	

Amp = Amphibole
And = Andalusite
Bt = Biotite
Chl = Chlorite
Crd = Cordierite
Ep = Epidote
Fsp = Feldspar
Grt = Garnet

Ms = Muscovite
Prh = Prehnite
Px = Pyroxene
Qz = Quartz
Sep = Sepiolite
Sme = Smectite
Srp = Serpentine
Talc = Tlc

Zeo = Zeolite
Crb = Carbonates
Spl = Spinel
SO_4 = Sulphates

Am = Amorphous